Exploiting Non Linear Piezoelectricity in Novel Semiconductor based Electronic Devices

A thesis submitted to the University of Manchester for the degree of

Doctor of Philosophy (PhD)

In the Faculty of Engineering and Physical Science

Joydeep Pal

2013

School of Electrical and Electronic Engineering

The University of Manchester

Faculty of Engineering and Physical Sciences

Abstract of thesis submitted by Joydeep Pal

For degree title of Doctor of Philosophy

Entitled *Exploiting Non Linear Piezoelectricity in Novel Semiconductor based Electronic Devices*

Date of Submission: 05 August 2013

Abstract

Materials have always had a large impact on society over the different ages. Piezoelectric materials are the often ‘invisible’ materials which find widespread use, unknown to the general public by large. Mobile electronics, automotive systems, medical and industrial systems are few of the key areas where ‘piezoelectricity’ is indispensable. The parking sensor of our car uses the effect and even the echo to image an unborn baby in a womb requires the exploitation of the piezoelectric effect.

The work presented in this thesis investigates the piezoelectric effect in semiconductors, namely in III-V, III-N and II-VI materials to have a better understanding and design potential applications in light emitting diodes (LEDs) and other electronic devices. The current work focuses on the non-linear behaviour in the strain of the piezo effect, which is manifested by the generation of electric field under crystal deformation.

Previous works have already confirmed the reports of the existence of non-linear piezoelectric effects in zincblende III-V semiconductors. Here, the same semiempirical approach using Density Functional Theory has been utilized to investigate the strain dependent elastic and dielectric properties of wurtzite III-N materials. While we report the strong non-linear strain induced piezoelectric behaviour with second order coefficients, all spontaneous polarization terms are substantially smaller than the previously proposed values. We show that, unlike existing models, our calculated piezoelectric coefficients and nonlinear model provide a close match to the internal piezoelectric fields of quantum well and superlattice structures. Also, pressure dependence of the piezoelectric field in InGaN based LEDs predicts a significant improvement of the spontaneous emission rate can be achieved as a result of a reduction of the internal field. The LED devices using the proposed structures including a metamorphic layer under the active region of the device are expected to increase their light output power by up to 10%. We also explored the impact of the non-linear piezo effect in nanowires and present a further theoretical computational study of single photon sources optimization in InGaN based wurtzite single quantum dots. We observed the light emission can be made by those single photon sources covering the entire visible spectrum through suitable change in the alloy composition.

Declaration

The author of this thesis declares that no portion of the work referred to in the thesis has been submitted in support of an application for another degree or qualification of this or any other university or other institute of learning.

Joydeep Pal

Copyright Statements

- The author of this thesis (including any appendices and/or schedules to this thesis) owns certain copyright or related rights in it (the "Copyright") and s/he has given The University of Manchester certain rights to use such Copyright, including for administrative purposes.

- Copies of this thesis, either in full or in extracts and whether in hard or electronic copy, may be made only in accordance with the Copyright, Designs and Patents Act 1988 (as amended) and regulations issued under it or, where appropriate, in accordance with licensing agreements which the University has from time to time. This page must form part of any such copies made.

- The ownership of certain Copyright, patents, designs, trade marks and other intellectual property (the "Intellectual Property") and any reproductions of copyright works in the thesis, for example graphs and tables ("Reproductions"), which may be described in this thesis, may not be owned by the author and may be owned by third parties. Such Intellectual Property and Reproductions cannot and must not be made available for use without the prior written permission of the owner(s) of the relevant Intellectual Property and/or Reproductions.

Dedication

This thesis is dedicated to my Mother and Father, ***Kakali Pal*** and ***Uttam Kumar Pal*** who have always encouraged and supported me all throughout my life.

This thesis is also dedicated to my Elder Brother, ***Subham Pal***, whom I am very fond of.

Acknowledgements

I wish to express deep gratitude and respect to thank my supervisor Dr. Max Migliorato for his excellent supervision and invaluable guidance and help throughout the lifetime of the project. His wide knowledge and logical way of thinking have been of great value for me.

I am deeply indebted to Dr. Geoffrey Tse for his advice and support through out the research work. I would like to thank my other colleagues Umberto Monteverde and Hanan Al-zahrani for their advice and motivation in the last three years.

Thanks also to all the colleagues at the School of Electrical and Electronic Engineering at the University of Manchester.

I am also very grateful to all my collaborators at University of Salford, University of Surrey and National Taiwan University, Taiwan.

Finally, I would also like to acknowledge the financial support of the EPSRC for making this work possible.

Table of Contents

Total Words count, including foot notes and end notes: 35,020

Table of Figures

List of Journal Publications

- U. Monteverde, M. A. Migliorato, J. Pal and D. Powell, "*Elastic and vibrational properties of group IV semiconductors in empirical potential modelling",* J. Phys.: Condens. Matter, **25**, 425801(2013).

- J. Pal, M. A Migliorato, C. K. Li, Y. R. Wu, B. G. Crutchley, I. P. Marko, S. J. Sweeney *"Enhancement of efficiency of InGaN-based light emitting diodes through strain and piezoelectric field management"*, J. Appl. Phys. **114**, 073104 (2013).

- G. Tse, J. Pal, U. Monteverde, R. Garg, V. Haxha, M. A. Migliorato, and S. Tomić, *"Non-linear piezoelectricity in zinc blende GaAs and InAs semiconductors"*, J. Appl. Phys. **114**, 073515 (2013).

- H.Y.S. Al-Zahrani, J. Pal and M. A. Migliorato, *"Non Linear Piezoelectricity in Wurtzite ZnO Semiconductors"*, Nano Energy (2013) (Article in press**).**

- B. G. Crutchley, I. P. Marko, J. Pal, M. A. Migliorato, S. J. Sweeney, "*Optical properties of InGaN-based LEDs investigated using high hydrostatic pressure dependent techniques"*, Phys. Stat. Sol. (B) **250**, 698 (2013).

- J. Pal, G. Tse, V. Haxha, M. A. Migliorato and S. Tomić, "*Importance of non linear piezoelectric effect in Wurtzite III-N semiconductors*", Opt. Quant. Electron, **44**, 195 (2012).

- J. Pal, G. Tse, V. Haxha, M. A. Migliorato and S. Tomić, "*Second-order piezoelectricity in wurtzite III-N semiconductors*", Phys. Rev. B **84**, 085211 (2011).

List of Conference Publications

- M.A. Migliorato, J. Pal, R. Garg, G. Tse, H.Y.S. Al-Zahrani, C-K. Li and Y R. Wu, B. G. Crutchley, I. P. Marko and S. J. Sweeney, S. Tomić, "*A Review of Non Linear Piezoelectricity in Semiconductors",* AIP Conference Proceedings of International Conference on Nanomaterials 2013 (Submitted).

- G. Tse, J. Pal, R. Garg, V. Haxha, and M. A. Migliorato, *"Non-linear piezoelectricity in zinc blende GaAs and InAs semiconductors"*, IEEE Conf. Proceedings of 12th International Conference on Numerical Simulation of Optoelectronic Devices (NUSOD), 2012, pp.85-86 (2012).

- J. Pal, G. Tse, V. Haxha, M. A. Migliorato and S. Tomić, "*Strain Dependence of Internal Displacement and Effective Charge in Wurtzite III-N semiconductors*", Journal of Physics: Conference Series **367**,012006 (2012).

- J. Pal, G. Tse, S. Tomić, and M. A. Migliorato, *"Investigating the effect of non linear piezoelectricity on the excitonic properties of III-N semiconductor quantum dots"*, IEEE Conf. Proceedings of 11th International Conference on Numerical Simulation of Optoelectronic Devices (NUSOD), 2011, pp.155-156 (2011).

List of Presentations

- J. Pal, "*Exploiting Linear and Non linear Piezoelectricity in Novel Semiconductor Devices*", at Materials Research Society (MRS) Spring Meeting and Exhibit 2013, San Francisco, USA.

- J. Pal, "*Strain Dependence of Internal Displacement and Effective Charge in Wurtzite III-N semiconductors*", Theory, Modelling and Computational Methods for Semiconductors TMCS III, Leeds, UK, 2012.

- J. Pal, "*Non Linear Piezoelectricity in ZincBlende GaAs and InAs Semiconductors*", Numerical Simulation of Optoelectronic Devices (NUSOD) 2012, Shanghai, China.

- J. Pal, "*Excitonic properties of visible-spectrum quantum-light sources for InGaN/GaN quantum dots*", International Symposium on Semiconductor Light Emitting Diodes ISSLED 2012, Berlin, Germany.

- J. Pal, "*Non-Linear Piezoelectric Effects on the Excitonic properties of the Gr-III-Nitrides Quantum Dots*", UK Semiconductors 2011, Sheffield, UK.

- J. Pal, "*Investigating the Effect of Non Linear Piezoelectricity on the Excitonic Properties of III-N Semiconductor Quantum Dot*", Numerical Simu-lation of Optoelectronic Devices (NUSOD), Rome, Italy, 2011.

List of Abbreviations

PL	**Photoluminescence**
DFT	**Density Functional Theory**
LDA	**Local Density Approximation**
DFPT	**Density Functional Perturbation Theory**
LED	**Light Emitting Diode**
HFET	**Heterostructure Field-Effect Transistor**
DEG	**Dimensional Electron Gas**
GGA	**Generalized Gradient Approximation**
PZC	**Piezoelectric Coefficients**
LM	**Linear Model**
NLM	**Non-linear Model**
NLE	**Non-linear Elasticity**
WZ	**Wurtzite**
ZB	**Zinc Blende**
QW	**Quantum Well**
QD	**Quantum Dot**
MQW	**Multi Quantum Well**
EBL	**Electron Blocking Layer**
NW	**Nanowire**

1. Piezotronics and Piezophototronics

The field of Piezotronics began in 2006 when Regent Professor Zhong Lin Wang at Georgia Institute of Technology coined two terms to describe the exploitation of strain induced Piezoelectricity in Nanostructured semiconductors to develop electronic devices with new functionalities. A piezoelectric potential can be created in any nanostructured semiconductor crystal having non-central symmetry, such as the Group III-V and II-VI materials, due to polarization of ions under applied stress and strain. Because of the presence of both piezoelectric and semiconductor behavior, the piezopotential in the crystal affects significantly the carrier transport at the interface/junction. The piezophototronic effect utilizes the piezopotential to influence the performance of optoelectronic devices[1], such as photodetector[2], solar cell[3], transducers[4] and LEDs[5] by controlling the material properties including the carrier generation, transport, separation and/or recombination. Unique applications can be observed in areas such as sensing and actuating in nanorobotics, human-computer interfacing, nanorobotics, smart MEMS/NEMS, smart and personalized electronic signatures and energy sciences.[6]

Within this area of research, energy harvesting involves the fundamental process of converting the nanoscale mechanical energy from the surrounding environment into electric energy. Such electrical energy can then be utilized to power nanodevices with less reliance on a battery. In 2006, a novel approach was reported converting the mechanical energy to electrical energy through the usage of piezoelectric zinc oxide (ZnO) nanowire (NW) arrays.[7] As a very promising self-powering sources of nanosystems, one can

envisage that eventually nanogenerators will be part of everyday life and will be included in mobile phones and portable devices.

What makes nanogenerators possible is the use of Nanowires (NWs), filaments thinner than a human hair, based on ZnO[8] and GaN.[9,10] Devices based on NWs have been demonstrated as nanogenerators7 and pressure sensors[11] in the past few year. These have generated much interest because of their potential commercial applications in self-powered circuits for wireless sensors, portable devices, medical science and mobile phones[12,13,14,15] but also as environmental sensors (pressure and vibrations). The most recent media coverage was for an array of such devices, mounted on a flexible substrate, which is able to mimic the tactile sense of human skin. A very recent work on a piezotronic transistor arrays has been published in Science[11] and major media covered the story including BBC[16], CNET[17], Nature World News[18], The Engineer[19], Science World Report[20], Physics World[21] and Engineering and Technology[22].

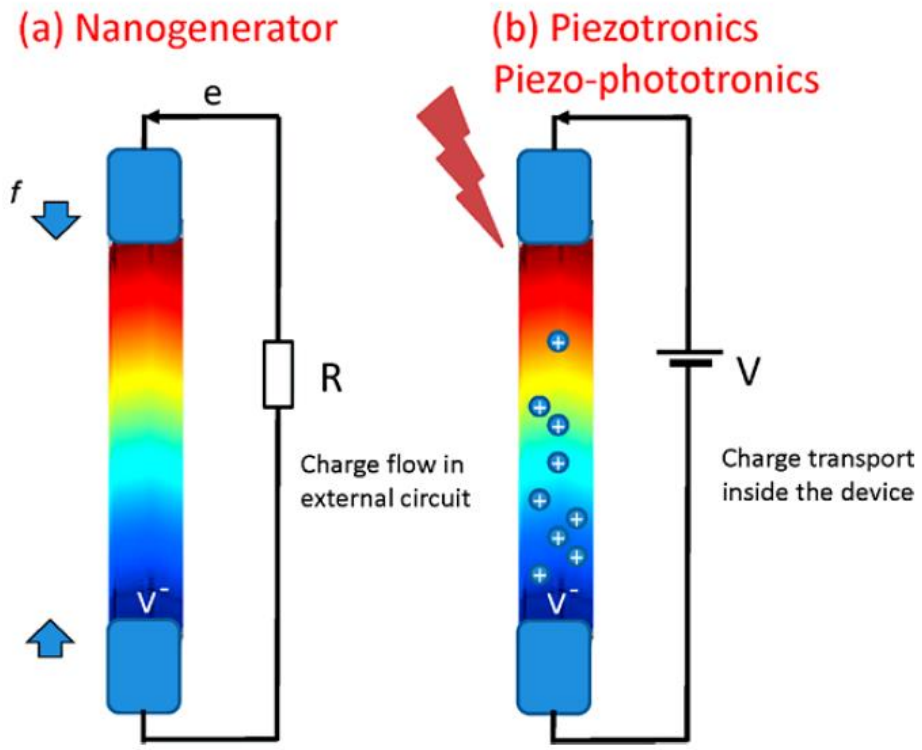

Figure 1-1: Piezopotential created inside a nanostructure, as represented by the color code, is the fundamental physics for nanogenerator and piezotronics. (reproduced from Z.L. Wang, "*Piezotronics and Piezo-Phototronics*", Microtechnology and MEMS, Springer-Verlag Berlin Heidelberg 2012)

In Figure1-1, the distribution of piezopotential inside a ZnO semiconductor NW is shown for both a nanogenerator and a piezotronics transistor. In a nanogenerator the pressure generates a potential difference that can be converted into an electric current. In a Piezotronics transistor pressure acts as a gate and allows or constricts the current flow.

Currently, the nanogenerator technology has been extensively developed and optimized to provide an output of ~3V with the output power capable to run a liquid crystal display (LCD), light-emitting diode or laser diode.[23]

Nanowire-based LEDs are of interest owing to the possible advantages of higher efficiency, higher lumens, and lower power consumption in comparison to traditional lighting modules. In a recent experimental work from Prof. Z. L. Wang's group in Georgia Institute of Technology, USA, it has been shown that the external true LED efficiency can reach ~7.82% after strain is applied. At a fixed applied bias above the turn-

on voltage (3V), with 0.093% compressive strain along the growth plane, the injection current and output light intensity is found to be improved by a factor of 4 and 17, respectively, projecting a conversion efficiency improvement of 4.25 compared to the unstrained case.[24]

Group III-Nitrides with wurtzite crystal structure and having much higher piezoelectric properties can also be utilized as the core nanostructures for LED,[25] piezotronics,[26] and even piezophotonics.[27] Recent works on III-V NWs illustrated potential applications in solar cells[28], lasers[29] and photodetectors[30]. Due to the direct band gap and superior electrical properties, III-V NWs are ideal candidates for photonic devices. Furthermore, III-V nanowires can be grown epitaxially on Si (and even Graphene!!!), giving a realistic prospect for large scale fabrication of III-V NW optoelectronic devices.[31,32,33]

Referring back to Fig 1-1 and the pressure controlled transistor, the reason we can call it a transistor is because it is obviously the counterpart of the conventional Silicon-based CMOS technology, operated by electrical driven charge transport process. In order to replicate the operational control of CMOS by mechanical action, generation of electrical signal is required as a result of mechanical stress. The obvious and natural choice is piezoelectricity and we will be discussing more in detail in later sections.

Almost all of the concepts discussed so far have been conceptualized and pioneered in the research group in Georgia Institute of Technology, USA. It was in this group that researchers started exploiting ZnO semiconductors and their material properties such as the electrostatic interaction energy and the distinct chemical activities of the polar surfaces to produce a wide variety of ZnO based nanostructures such as nanowires, nanobelts, nanosprings, nanorings, nanobows, nanopropellors, nanocages and nanohelices. The nanostructures have been synthesized under ad hoc growth conditions,

using a solid state thermal sublimation process and controlling the growth kinetics, local growth temperature, and the chemical composition of the source materials.[34]

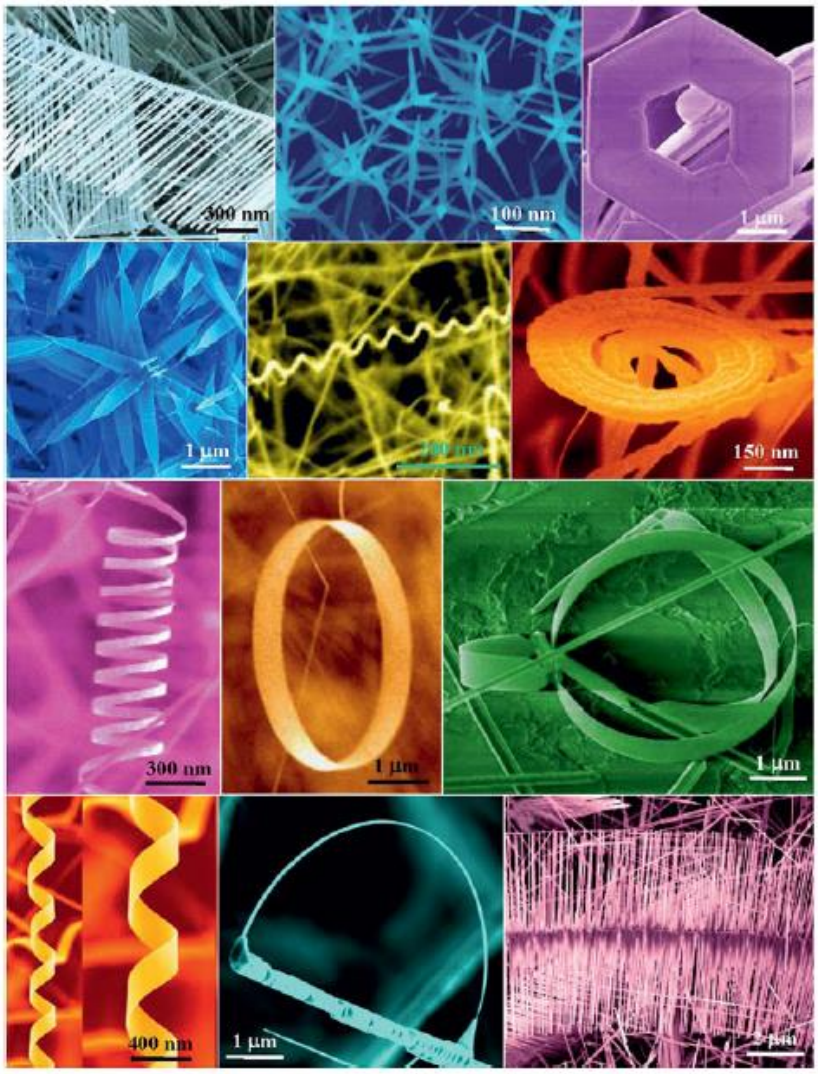

Figure 1-2: A collection of nanostructures of ZnO nanostructures due to existence of [0001] polar surface (reproduced Z. L. Wang, MRS Bulletin, 37, 814 (2012))

Fig.1-2 shows high magnification scanning electron microscopy (SEM) images of the nanostructures. ZnO nanobelts and the associated unique nanostructures were grown by a vapor-solid process.

Vertically aligned NWs are the most exploitable structures for potential applications mentioned earlier and aligned growth of ZnO nanorods has been performed successfully on a solid substrate using a vapor-liquid-solid or vapor-solid-solid process with gold

nanoparticles as catalysts.[35, 36] While the catalyst initiates and provides guidance for growth, the epitaxial orientation relationship between the substrate and the nanorods gives rise to aligned growth.[37] The patterns of the grown NWs are determined by the spatial distribution of the catalyst particles. An optimum match of the desired NWs and the substrate lattice provides aligned growth of NWs normal to the substrate. One of the low-cost, low-temperature and large scale approach for aligned NWs is the solution based growth technique.[38,39] As the growth temperature is only 80-100°C, substrate of any material and shape can be used allowing a broad range of applications.

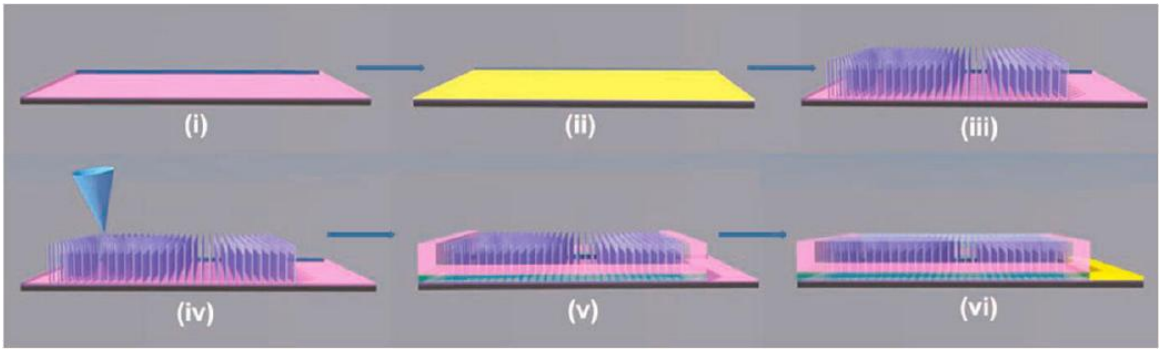

Figure 1-3: Fabrication flowcharts of a GaN NW LED device, including (i) growth of a p-type GaN thinfilm on (0001) sapphire, (ii) Au catalyst thin-film evaporation, (iii) growth of n-type GaN NWs, (iv) piezoelectric investigation with an atomic force microscope, (v) spin-coating of a polymer spacer (PMMA) in the LED device, and (vi) deposition of InO and Au/Ni electrodes for n-type and p-type contact, respectively (Reproduced from C-Y. Chen *et al*, ACS Nano 6 (6), 5687-5692 (2012))

In Figure 1-3, the fabrication process of GaN NW based LED modules has been illustrated including several procedures for e-beam photolithography, with (i) p-type GaN thin film grown on a c-plane (0001) sapphire by MOCVD, (ii) a Au catalyst thin film is deposited in ultrahigh-vacuum thermal evaporation, (iii) n-type GaN nanowires grown on a p-type thin film by a vapor-liquid-solid process, (iv) piezoelectric performance studied through a unique AFM measurement, (v) spin-coated polymethyl methacrylate (PMMA) as the binding spacer in LED devices, and (vi) an indium oxide (InO) layer and Au/Ni electrodes for n-type and p-type contact are deposited, respectively.

In the case of III-V semiconductors NW growth, the crystallographic quality still remains difficult to control despite the significant advances in growth techniques. The stable phase in bulk III-V materials is the cubic zinc blende (ZB) phase but it is not always predominant in NWs. Rather, often NWs replicate the hexagonal wurtzite (WZ) phase in sections of, or throughout, the NW. ZB-WZ polytypism, stacking faults and twin defects are reported quite often.[40] As device applications require excellent physical properties, control over the NW crystal structure is essential. Although the commonly reported problems are non-desirable, they can be used to engineer the NW bandstructure, luminescence polarization and the emission energy.[40,41,42] Several recent works reported the issue of diameter dependency of the NW crystal structure, with smaller diameter tending towards a WZ phase while larger diameter favours ZB phase.[43,44,45] Algra *et al.*[44] reported a dramatic transition of WZ structure to a periodically twinned ZB structure with the addition of Zn dopants to the InP NW growth system. Instead Caroff *et al.* [45] utilized a combination of NW diameter and growth temperature to achieve InAs NWs in periodically twinned ZB phase and WZ phase with higher control.

The field has grown rapidly over the past few years. In particular the development of different approaches for energy harvesting using piezotronics and nanogenerators has stimulated great interest even in the commercial sector where there is a significant demand for wireless self powered sensors. In December 2012, the first international Xiangshan Science Conference was held in Beijing (China) dedicated to the frontiers of piezotronics and nanogenerators. The MRS 2013 Spring Meeting and Exhibit, held from April 1-5, 2013, at the Moscone West Convention Center in San Francisco, California, dedicated an entire symposium to piezotronics.

Thus, the field of piezotronics and piezophototronics has gained much attention worldwide signifying the need of much better understanding about the materials involved and their exploited properties, which is discussed in the next sections.

1.1. Piezoelectric Semiconductors

The crystal classes of Cane sugar, Quartz, Tourmaline, Rochelle salt (sodium potassium tartrate tetrahydrate) and Topaz have all demonstrated to exhibit a piezoelectric effect. The effect has also been observed in the crystal classes having cubic (e.g. InGaAs) and hexagonal (GaN and ZnO) symmetries. Applications such as energy harvesters, actuators, micro-positioners, ultrasonic transducers for sonar and medical imaging and fuel injectors have utilized the piezoelectric effect.

The nature of the effect is the same as the generation of electrical dipole moments observed in solids. On application of a mechanical stress, a change in polarization is seen in the crystal, as the charge symmetry is broken. This asymmetry in the charge density leads to an electric field in the crystal which is known as the piezoelectric field. Though the electric field is difficiult to measure directly, an impact can be observed on both the electrical and optical properties of the crystal.

The last few years have witnessed a significant interest in investigating the impact of the piezo-effect in the epitaxially grown semiconductor materials. The exploitable nature of the variable piezo effect in wide range of applications has already been highlighted within

the field of piezotronics in the previous section. A detailed analysis of this effect in the III-V's, mainly III-Nitrides and II-VI's can be found later in chapter 3.

The changes in the spontaneous (polarization that exists even in the absence of external pressure) and piezoelectric polarization fields lead to the increase in the polarization-induced electrostatic charge density. In a structurally pure bulk semiconductor, the variation in the polarization fields will be observed at the surfaces. Nonetheless, the existence of the surface states or mobile carriers can nullify the resultant surface charges. However, in a heterostructure, the polarization and the associated polarization-induced charge has a significant influence on the internal electric field and the charge distributions. Donor-like or acceptor-like behaviour is stimulated in many ways by the induced positive or negative charge polarization. The behaviour of the polarization-induced charge is electrostatically indistinguishable to the charge density due to the ionized dopants. The presence of a small dipole factor in each unit cell produces a uniform distribution of polarization induced volume charge density within the alloy layer. Although the polarization is dependent on the semiconductor properties in the ZB or WZ phase, examples of different crystal structures in III-V, III-N and II-VI semiconductors have been provided. In the case of ZB InAs grown pseudomorphically on GaAs (001) a PZ polarization of $+0.069 C/m^2$ is predicted using the PZCs by Beya-Wakata *et al.*[46] For the case of WZ semiconductors, a thin film of GaN layer when grown on AlN in [0001] direction gives rise to a compressive strain of 3% and a polarization of $+0.095 C/m^2$ is predicted and in ZnO a polarization of $+0.01 C/m^2$ is expected when strained compressively by 3% in the growth plane using the classic linear model of piezoelectricity[47].

The piezoelectric effect is now explained in more details exploring the fundamental concepts and material properties.

1.2. Piezoelectric Effect

The field of Piezotronics solely relies on piezoelectricity and as we have already seen the exploitation of the effect can have large influence on the device properties, we will explain in more detail about the present understanding of this phenomenon.

The direct piezoelectric effect is the generation of an electric dipole moment in certain crystals if a stress is applied and the electric dipole moment is proportional to the applied stress.[48] Such an effect was demonstrated first by Jacques Curie and Pierre Curie in the year of 1880. The origin of the word "*piezo"* is from the Greek word "*piezen (πιέζειν)"* which means *"to press or squeeze"*. The effect has been understood as the charge formation in some crystals due to the ionic displacements under some mechanical pressure.[49]

The converse piezoelectric effect, where the crystals deforms under the application of external electric field in the polarization direction, has been outlined mathematically in 1881 by Gabriel Lippmann from fundamental thermodynamic principles. Later in 1910, the publication "Lehrbuch der Kristallphysik" (textbook on crystal physics) by Woldemar Voigt classified 20 natural piezoelectric crystal classes. The publication also had detailed an investigated report of the piezoelectric constants using tensor analysis.

1.2.1. Piezoelectric Polarization

The non-centrosymmetric feature of the hexagonal WZ and the cubic ZB structure gives rise to the nonzero piezoelectric moduli.

Although both WZ and ZB give rise to piezoelectric polarization, the cubic ZB structure has higher symmetry than the WZ structure as can be seen in the figure 1.2.1-1:

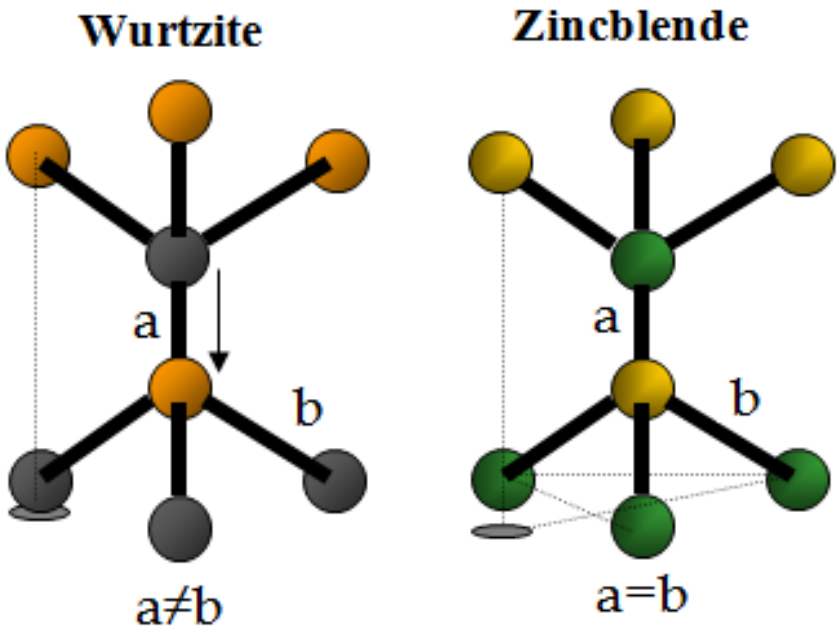

Figure 1.2.1-1: Crystal Structures of Wurtzite and Zinc blende crystals

The tetrahedrons are the fundamental units of the crystals and in ZB crystals, the atoms of both tetrahedrons do not overlap each other, while owing to reduced symmetry, the atoms in different tetrahedrons exactly overlap in WZ leading to a repulsive force at the centre of the two tetrahedrons. This gives rise to an inherent polarization term in the unstrained WZ crystals compared to the unstrained ZB structures and this inherent component of polarization in WZ, even in absence of any strain, is known as spontaneous polarization. We will be discussing the spontaneous polarization in the next section in much more detail.

Here, the relations of the piezoelectric polarization field P_{pz} with the piezoelectric moduli d_{ijk} and e_{ijk}, the stress tensor σ_{jk} and the strain tensor ε_{jk} is expressed as follows[48]:

$$P_{pz,i} = d_{ijk}\sigma_{jk} = e_{ijk}\varepsilon_{jk}, \sigma_{ij} = c_{ijkl}\varepsilon_{kl} \quad (1)$$

where c_{ijkl} is the elastic tensor.

The symmetry of the tensors d_{ijk},σ_{jk}, e_{ijk} and ε_{jk} belongs to the indices of j and k; Hence, a unique array of indices are labelled as $j = xx, yy, zz, yz, zx, xy \equiv 1, \ldots, 6$ and the short matrix notation is taken for the tensors in Eq. (1).

The matrix notation for e_{ij} and ε_j is denoted as follows:

$$e_{ij} = \begin{pmatrix} e_{11} & e_{12} & e_{13} & e_{14} & e_{15} & e_{16} \\ e_{21} & e_{22} & e_{23} & e_{24} & e_{25} & e_{26} \\ e_{31} & e_{32} & e_{33} & e_{34} & e_{35} & e_{36} \end{pmatrix} \quad (2)$$

$$\varepsilon_j = \begin{pmatrix} \varepsilon_1 \\ \varepsilon_2 \\ \varepsilon_3 \\ \varepsilon_4 \\ \varepsilon_5 \\ \varepsilon_6 \end{pmatrix} = \begin{pmatrix} \varepsilon_1 & \varepsilon_6 & \varepsilon_5 \\ \varepsilon_6 & \varepsilon_2 & \varepsilon_4 \\ \varepsilon_5 & \varepsilon_4 & \varepsilon_3 \end{pmatrix} \quad (3)$$

We first discuss about the ZB structure, where we have only three non-zero independent coefficients

$$e_{ij} = \begin{pmatrix} 0 & 0 & 0 & e_{14} & 0 & 0 \\ 0 & 0 & 0 & 0 & e_{25} & 0 \\ 0 & 0 & 0 & 0 & 0 & e_{36} \end{pmatrix} \quad (4)$$

When we have the unstrained case, it was shown by Nye (1957)[48] that the ZB crystal structure has only one non-zero coefficient from Eq.(4) as $e_{14} = e_{25} = e_{36}$. The WZ phase is bit more complicated with five different coefficients in the strained case.

The five independent non-zero coefficients present in the piezoelectric tensors of the WZ structure, is

$$e_{ij} = \begin{pmatrix} 0 & 0 & 0 & 0 & e_{15} & 0 \\ 0 & 0 & 0 & e_{24} & 0 & 0 \\ e_{31} & e_{32} & e_{33} & 0 & 0 & 0 \end{pmatrix} \quad (5)$$

In the case of zero strain in the WZ structure, all the five coefficients are reduced to only three independent non-zero coefficients, given in Eq. (5)[48], as $e_{31} = e_{32}$, and $e_{15} = e_{24}$ and d_{ij} is symbolized by an analogous term.

Thus, a piezoelectric polarization field with nonzero values exists along the (111) growth direction diagonal to the normal growth axis (001) in ZB structures. The polarization is present along the c-axis direction in an [0001] epitaxially grown coherently strained WZ structures of III-N or II-VI material.

In case of ZB, $\varepsilon_3 = -2\frac{c_{12}}{c_{11}}\varepsilon_1$ (6)

But, the piezoelectric polarization is only present when we have the off-diagonal components of the strain tensor available.

$P_{pz,x}^{zb} = e_{14}\varepsilon_4, P_{pz,y}^{zb} = e_{25}\varepsilon_5$ and $P_{pz,z}^{zb} = e_{36}\varepsilon_6$. (7)

While for WZ, a free-surface boundary condition for surface charge ($\sigma_{zz} \equiv \sigma_{33} = 0$) is supposed to be present as the polarization is directed in the [0001] or z- direction, then

$$\varepsilon_3 = -2\frac{c_{13}}{c_{33}}\varepsilon_1 \quad (8)$$

$$P_{pz,z} = 2(e_{31} - \frac{c_{13}}{c_{33}}e_{33})\varepsilon_1 = 2d_{31}(c_{11} + c_{12} - 2\frac{c_{13}^2}{c_{33}}e_{33})\varepsilon_1 \quad (9)$$

The growth of an alloy with a lattice constant *a* on a substrate which is coherently strained, generates a strain expressed by:

$$\varepsilon_1 = \varepsilon_2 = \frac{a_{sub} - a}{a},$$

where a_{sub} is the lattice constant of the substrate material.

We have compiled the experimental values of the coefficients of different III-V, III-N and II-VI semiconductors in the following table[50,51,52,53,54]. The experimental data presented are for the natural crystalline material symmetry and data is missing for rest of the combinations.

TABLE I: Experimental values of the piezoelectric coefficients of III-V, III-N and II-VI semiconductors

Semiconductor		Piezoelectric coefficients (C/m^2)			
		$e_{14}=e_{25}=e_{36}$	e_{31}	e_{33}	e_{15}
ZB	**GaAs**	-0.160			
	InAs	-0.045			
WZ	**GaN**		-0.55	1.12	
	InN		-0.55	0.95	
	AlN		-0.60	1.50	-0.48
	ZnO		-0.62	0.96	

In later sections, we will discuss the piezoelectric coefficients (PZCs) in more details and we will introduce the influence of non-linear piezoelectricity.

1.2.2. Spontaneous Polarization

Though epitaxially grown wurtzite semiconductors formed in the typical [0001] orientation lead to the creation of a sizeable piezoelectric field when strain is present. Additionally, large spontaneous polarization[47] is also present in both III-N and II-VI semiconductors. As spontaneous polarization (like the strain induced one) cannot be measured directly, it can only be inferred from experimental data on electro optical properties and their change as a result of strain. In addition, the electrostatic charge densities produced by the spontaneous polarization can be comparable to those produced by the strain induced piezoelectric polarization fields.[55]

Spontaneous polarization develops from the atomic layout in the bulk materials. In the wurtzite structure, z-direction marks the overlap of the neighbouring dual tetrahedrons in contrast to the zinc blendes. As already pointed out earlier, this arrangement gives rise to closer second nearest neighbours in the wurtzites. The modified inter-atomic forces lead to a marginal reduction of the inter-atomic separation between the first nearest neighbours. Thus, the non-zero dipole moment in the crystal that is present in the absence of strain or an electric field[55] is the spontaneous polarization.

The charge reorganization at the surface of the bulk materials is assumed to cancel the uniform polarization fields owing to the piezoelectric and spontaneous polarization effects. Conversely, the variations in the crystal structure of the inhomogeneous alloy layers or heterostructures creates a non-vanishing and spatially altering field due to the piezoelectric and spontaneous polarization. The difference in the composition also generates the charge densities which have a prominent influence on device behaviour[55] and the properties of the material.

While investigating multilayered structures and piezo-devices,[56] spontaneous polarization needs to be also included.

The wurtzite III-N structures demonstrate a peculiar property of having the piezoelectric constants similar to those of the Group II-VI materials and quite starkingly opposite to the Group III-V materials. The III-N materials also differ from the normal III-V compounds, with a larger ionic charge and the internal-strain ionic contribution becomes larger than the clamped-ion term. The following table provides the compiled list for the spontaneous polarization values[47] of different III-N and II-VI semiconductors.

TABLE II: Spontaneous polarization values of III-N and II-VI semiconductors

	Semiconductor	Spontaneous Polarization (C/m^2)
WZ	**GaN**	-0.029
	InN	-0.032
	AlN	-0.081
	ZnO	-0.057

1.3. The Microscopic Model

So far we have described piezoelectricity in terms of macroscopic terms. An alternative model to analyse the effects of polarization has been proposed by Harrison[57] based on Bond-Orbital Approximation which is at the origin of the microscopic understanding of piezoelectricity which will be used throughout this thesis.

The total polarization resulting from both spontaneous and strain induced polarization is given by the sum of a direct dipole contribution and a bond contribution:[57]

$$P_{\hat{x}_i} = \frac{Z_H^* \delta r + 2\alpha_p \left(1-\alpha_p{}^2\right) \cdot \sum_{q=1}^{4} \left(\vec{r}_q \cdot \hat{x}_i\right) \delta R_q}{2\Omega} \qquad (10)$$

where $\hat{X}_i$ is the Cartesian direction, δr is the displacement vector of cations in respect of anions from the ideal position (i.e. the situation where all bonds in the tetrahedron are equal to each other), r_q and δR_q are the distance and displacement (deviation from the ideal position) vectors of the nearest neighbour q from the atom at the centre of the tetrahedron, respectively, α_p is the bond polarity and Ω is the atomic volume. Borrowing from the language of tight binding, Z_H^* is the atomic charge, generally different from the transverse effective charge, which instead has its direct equivalent in the dynamic effective charge, or Born charge (Z*), calculated with density functional perturbation theory (DFPT).

In the case of ZB crystals, as the tetrahedrons are subjected to small shear strain, the cation and anion sublattices undergo displacement relative to each other to minimize the cohesive energy. This is relaxation across the direction perpendicular to the shear strain, e.g., along the k direction when the shear strain is along the ij plane, as initially pointed out by Kleinman.[58]When the internal displacement takes place, the bond lengths in each tetrahedron become non equivalent and therefore both terms in Eq. 11 become non-zero. If the difference between the two terms is different from zero then a macroscopic polarization is predicted. A more comprehensive discussion and formalization of these concepts will be presented in Chapter 3. The displacement is dependent on the shear strain and is assumed to be linear in the strain, and therefore can be characterized by ζ, the Kleinman parameter. The Kleinman parameter defines the distance between the two sublattices and normally a constant for a material. The displacement can be easily written as $a\varepsilon_{ij}\zeta/4$, with a, the lattice constant and ε_{ij}, the shear strain. The PZCs can be then obtained in the ZB case from

$$P_{strain}^{ZB} = e_{14}\varepsilon_{\hat{i}\hat{j}} = P_{\hat{k}} = \frac{e}{2\,\Omega}\frac{a\varepsilon_{ij}\zeta}{4}\left(Z_H^* - \frac{4}{3}\alpha_p\left(1-{\alpha_p}^2\right)\frac{(1-\zeta)}{\zeta}\right) \qquad (11)$$

where $\varepsilon_{\hat{\imath}\hat{\jmath}}$ is the strain component and ζ is the Kleinman parameter. For the case of WZ structures, one must also take the spontaneous polarization into account,

$$P_{strain}^{WZ} = e_{31}\varepsilon_{\parallel} = P_{Tot} - P_{sp} = \frac{Z_H^*(\delta r - \delta u) + 2\alpha_p(1-{\alpha_p}^2)\sum_{q=1}^{4}(\overrightarrow{r_q}\cdot\hat{x}_i)\delta R_q}{2\Omega} \quad (12)$$

In later chapters, we will discuss more in details about the parameters and the coefficients obtained in our calculations.

1.4. Polar semiconductors

The polar semiconductors in Group III-V, III-N and II-VI are all important in their different applications and in this section, applications and research interest in each group of semiconductors will be described in detail.

In epitaxially grown ZB III-V semiconductors, the piezoelectric effect can be found in quantum wells grown on (111) substrates, quantum wires, and quantum dots. Piezoelectric effects in such nanostructures have attracted a substantial amount of interest in recent years,[59,60] and were identified as the source of experimentally observable optical anisotropies.[61,62,63]

For (111) orientation, where the PZ polarization is maximum in the ZB materials, InGaAs/GaAs (111)B heterostructures based MQW p-i-n photodiodes are found to have a significant influence on the device performance.[64] Enhancement of the 2DEG density in AlGaAs/InGaAs/GaAs p-HEMT structures have also been observed on (111)A GaAs substrates[65]. These HEMT based power microwave devices that work or operate in the 30–100 GHz range are used in many high-speed digital applications[66,67]

Moreover, InGaAs/AlGaAs laser diodes grown in (111)B direction demonstrated a positive role of the piezoelectric effect in reducing the threshold current of the diodes.[68] In GaAs/AlGaAs core-shell NWs, piezoelectric field is observed to reduce the carrier recombination due to the induced spatial separation of electron and holes.[69]

Apart from the QW structures, the strain induced effect is observed even in the quantum dots.[70] Single dot spectroscopy of InAs/GaAs QDs grown along polar direction has shown large Stark shifts due to the piezoelectric field as large as 800kV/cm.[71]Recent works on the embedded GaAs QD into AlGaAs NW have also illustrated relatively stronger electric field due to PZ effect compared to typical values observed in ZB QDs.[72]

On the contrary, III-Nitride heterostructures are employed for an abundant variety of device applications, including ultraviolet high-power electronics,[73,74,75] photodetectors,[76,77] light-emitting diodes (LEDs) and lasers[78] as also field emitter arrays.[79] Thus the research on III-Nitrides is gaining momentum owing to the expected high volume demand and low production costs. The latest 'Blu-Ray' technology from Sony Corporation, exploit GaN based Blue LASERs to enable read/write mechanism. In addition, due to the presence of their wurtzite structure with high level of ionicity, wide range of exploitable material properties are demonstrated, which could have much less significance or even be absent in fundamental and normal zinc blende III-V semiconductors. The particular interests are the piezoelectric and the spontaneous polarization effects as they can be utilised to advantage in device engineering, as advocated by the recent experimental as well as the theoretical investigations or studies.[80,81,82]

In III-N heterostructure field-effect transistors (HFET's), two dimensional electron gas (2DEG)[83] generated with intensely high carrier concentrations[84] are the effect of the

positive polarization at the junction interface. The polarization induces electrostatic charge in the devices and helps to achieve a major increase in barrier height, and consequently a reduction in gate leakage current, without increasing the total barrier thickness.[85]

The investigation of photoluminescence from an III-N multiple quantum-well structure also illustrates the Quantum Confined Stark Effect due to the piezoelectric polarization fields as blue shift is observed with increasing excitation intensity[86].

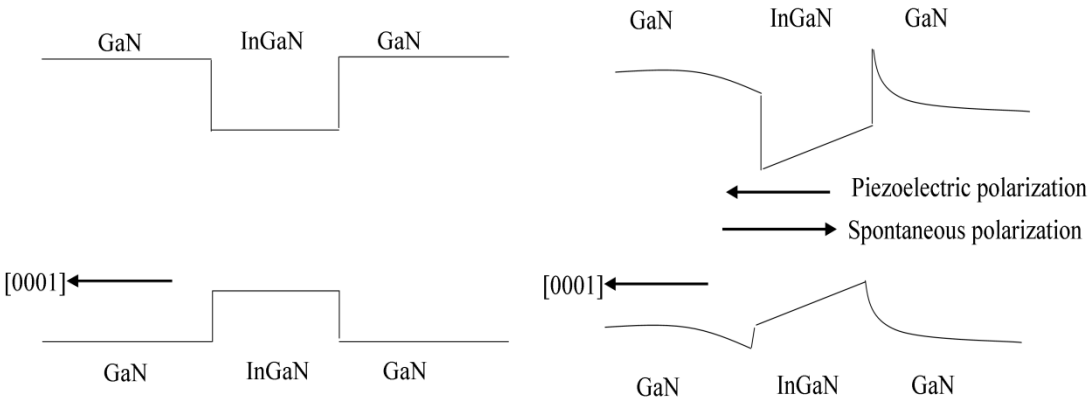

Figure 1.4-1: Schematic energy band diagrams for an $In_yGa_{1-y}N$/GaN single-quantum-well structure (a) in the absence of polarization fields (b) in the presence of the piezoelectric field within the $In_yGa_{1-y}N$ layer

Hence, the optical properties in nitride quantum-well structures are strongly affected by polarization fields and the associated electrostatic charge densities. The polarization-induced field in an $In_yGa_{1-y}N$/GaN quantum well structure will lead to a red shift in the PL wavelength, in the absence of screening effects, in comparison to absence of polarization effects. This polarization-induced red shift would be expected to increase with increasing well width. In Figure 1.4-1, the schematic band energy diagrams are shown where on the left, the ideal case of zero polarization is considered and on the right, with the presence of the polarization, enhanced band bending due to piezoelectricity and spontaneous polarization is illustrated.

While it was discussed in detail about the PZ effect in ZnO based NWs and its application on previous occasion, this section will focus more on the impact of piezoelectricity on other ZnO based nanostructures and applications. Polarization effects observed in ZnO based LEDs reveal a strong hole confinement.[87] Also, ZnO films have been utilized in detectors and actuators and can be used to detect the strain and provide feedback.[88] In addition, ZnO nanobelts have been demonstrated to work as bulk acoustic resonators (BARs) for high performance frequency control devices exploiting the piezoelectric polarization.[89]

Recent work on exploiting the PZ effect in two-dimensional ZnO based nanosheets has been explored for efficient direct current power generation.[90] Interface engineering has also been observed in ZnO based photoelectrochemical anode by exploiting the PZ polarization.[91]

Recent progress in the field of piezoelectricity led to research interests in converting 2D layers into PZ materials. One such work relates to study of 2D graphene to make it a PZ material and provide dynamic control over graphene based electronics and devices. The inversion symmetry in graphene needs to be broken to generate piezoelectricity[92]. The authors proposed and discussed technique to break the symmetry by the adsorption of atoms on the surface of graphene only on one side requiring spatial control of the adsorption method, as demonstrated in recent experiments to produce hydrogen and fluorine covered graphene (graphane and fluoro-graphene)[93,94]. The piezoelectric properties of graphene are predicted to be smaller by a factor 3 compared to GaN in this work and this could potentially lead to the creation of new piezoelectric devices.[92]

As the piezoelectric polarization is very much dependent on the stress and strain, it is imperative to understand the concepts in details and we have discussed the underlying theory in more details in the next chapter.

2. Research Modeling Techniques

The current work described in the thesis has utilized different modelling techniques and it is imperative to provide a deeper insight in these research methodologies. While we start discussing the concepts of stress and strain at the beginning of the chapter, we introduce Density Functional Theory and the k·p theory in the later sections.

2.1. Stress and Strain

Stress and strain are two important factors in the characterization of condensed matter. Stress and strain can be responsible for fractures and creation of defects in the crystal. Also, bandstructure and device behaviour gets affected by strain, which can be utilized in device design. Stress can also be quantified by experimental microscopy processes. In the later sections, we will discuss more about the stress, strain, their relationship and how they can be used in certain applications.

The different combinations of pressure on a material as shear and dilation can be expressed through a stress tensor. In terms of condensed matter, independent parameters, like macroscopic stress and atomic force defines the final conditions of equilibrium[95] of the system.

*"**Condition (1)**: the total force vanishes on each atom*

***Condition (2)**: the macroscopic stress equals the externally applied stress."*

The conditions are widely used in classical simulations[96] (such as metric[97] and Parrinello-Rahman[98] methods), and now became an integral part of electronic structure calculations[99] where the structure is relaxed by minimizing with respect to the atomic positions in a unit cell and shape and size of the cell.

2.1.1. Elastic strain

An unstrained system with axes $\hat{x}$,$\hat{y}$, $\hat{z}$ will be distorted to a new system of axes x', y' and z' under external pressure. The deformation could be owing to any kind of applied pressure on the material as shear or dilation and creates small strains in the system.[141]

The current section explores the basic expression for strain in crystalline materials. The new set axes is related to the original unstrained one as follows,

$$x' = (1 + \epsilon_{xx})\hat{x} + \epsilon_{xy}\hat{y} + \epsilon_{xz}\hat{z} \quad (13)$$

$$y' = \epsilon_{yx}\hat{x} + (1 + \epsilon_{yy})\hat{y} + \epsilon_{yz}\hat{z} \quad (14)$$

$$z' = \epsilon_{zx}\hat{x} + \epsilon_{zy}\hat{y} + (1 + \epsilon_{zz})\hat{z} \quad (15)$$

where $\epsilon_{\alpha\beta}$ defines the deformation in the system.

Also, an important fact is that the new axes have lost their orthogonality in general.

The following expression shows the relation of the space vector r' with the distorted axes as

$$r' = xx' + yy' + zz' \quad (16)$$

For the case of unstrained system, the expression is as follows

$$r = x\hat{x} + y\hat{y} + z\hat{z} \quad (17)$$

The displacement of the deformation is obtained by the difference in the space vectors,

$$R = r' - r \quad (18)$$

$$= x(x' - \hat{x}) + y(y' - \hat{y}) + z(z' - \hat{z})$$

Using the last three equations, the expression can be rewritten as

$$R = \left(x\epsilon_{xx} + y\epsilon_{xy} + z\epsilon_{xz}\right)\hat{x} + \left(x\epsilon_{yx} + y\epsilon_{yy} + z\epsilon_{yz}\right)\hat{y} + \left(x\epsilon_{zx} + y\epsilon_{zy} + z\epsilon_{zz}\right)\hat{z} \quad (19)$$

Hence, three new quantities u, v and w have been defined as

$$u = \left(x\epsilon_{xx} + y\epsilon_{xy} + z\epsilon_{xz}\right)$$

$$v = \left(x\epsilon_{yx} + y\epsilon_{yy} + z\epsilon_{yz}\right)$$

$$w = \left(x\epsilon_{zx} + y\epsilon_{zy} + z\epsilon_{zz}\right) \quad (20)$$

In the limit of small strain, the position dependent strain can be defined for a general non-uniform distortion.

$$x\epsilon_{xx} = x\frac{\partial u}{\partial x};\ y\epsilon_{yy} = y\frac{\partial v}{\partial y};\ z\epsilon_{zz} = z\frac{\partial w}{\partial z} \quad (21)$$

The diagonal strain components can be used to define distortion as

$$e_{xx} = \epsilon_{xx} = \frac{\partial u}{\partial x};\ e_{yy} = \epsilon_{yy} = \frac{\partial v}{\partial y};\ e_{zz} = \epsilon_{zz} = \frac{\partial w}{\partial z} \quad (22)$$

While the off-diagonal terms, defining the shear strain or angular distortion of strain, can be expressed as

$$e_{xy} = x' \cdot y' \approx \epsilon_{yx} + \epsilon_{xy} = \frac{\partial u}{\partial y} + \frac{\partial v}{\partial x} \quad (23)$$

$$e_{yz} = y' \cdot z' \approx \epsilon_{zy} + \epsilon_{yz} = \frac{\partial v}{\partial z} + \frac{\partial w}{\partial y} \quad (24)$$

$$e_{xz} = x' \cdot z' \approx \epsilon_{zx} + \epsilon_{xz} = \frac{\partial u}{\partial z} + \frac{\partial w}{\partial x} \quad (25)$$

The net fractional change in the volume due to distortion is defined by Dilation and can be expressed as

$$\delta = \frac{V'-V}{V} \approx e_{xx} + e_{yy} + e_{zz} \quad (26)$$

where V and V' are the volume before and after distortion and initial cubic volume is unity.

It is important to outline the stress components responsible for producing a distortion in a crystalline unit cell. Then, stress can be defined as the applied force over area. We can have 9 possible quantities of stress. However, in absence of torque on the system, we can have a reduced set of 6 stress quantities. The stress quantities are indicated as

$$X_x, Y_y, Z_z, X_y, Y_z, Z_x$$

where the main letter, in capitals, represents the direction of force while the subscript represent the direction perpendicular to the plane of stress and also, the following condition is met,

$$X_y, = Y_x; X_z, = Z_x; Y_z = Z_y \quad (27)$$

In the following sections using the stress-strain relations, the general expression for the elastic constants can be obtained. This will be very helpful in studying the elastic properties of crystalline material. The strain mentioned here defines the terms of displacement, internal strain parameter and moreover the piezoelectric constants can also be estimated utilizing the same relations.

2.1.2. Macroscopic strain and stress

The atomic displacement of an atom $R = r - r'$ from a point r to r' due to deformation under applied pressure of shear or dilation is defined as strain. Here, the displacement *R* depends on the space coordinate *r*, which specifies the deformation. This can be illustrated with an example. Considering two near points connected together, the deformation will initiate a change of vector from dr to dr' and the distance in between the two points changes to dl' from the corresponding $dl = \sqrt{(dr_1^2 + dr_2^2 + dr_3^2)}$. The lowest order in u, dl' is given as follows

$$(dl')^2 = dl^2 + 2R_{\alpha,\beta} dr_\alpha dr_\beta \quad (28)$$

where the summation over Cartesian coordinates α and β are assumed, and

$$R_{\alpha,\beta} = \frac{1}{2}\left(\frac{\partial R_\alpha}{\partial r_\beta} + \frac{\partial R_\beta}{\partial r_\alpha}\right) \quad (29)$$

This is strain tensor. This is equivalent to the metric tensor that provides changes in the lengths in the deformed system from the undeformed coordinates[100]

$$(dl')^2 = \delta_{\alpha,\beta} + 2R_{\alpha,\beta} dr_\alpha dr_\beta \quad (30)$$

Also, it is convenient to define the strain tensor $\delta_{\alpha,\beta}$ and unsymmetrized strain tensor $\epsilon_{\alpha\beta}$, a scaling in space, as

$$r_\alpha \rightarrow (\epsilon_{\alpha,\beta} + \delta_{\alpha,\beta}) r_\beta \quad (31)$$

The terms such as rotation will not affect the internal coordinates itself and thus allows us to use the expression in Eq. (31) relating to internal energy. The expression is valid for symmetric systems clearly even when antisymmetric terms, like rotation, are included.

The macroscopic average stress tensor $\sigma_{\alpha,\beta}$ is defined by the derivative of the energy to the strain tensor, per unit volume. The strain is considered to be homogenous over macroscopic regions.

$$\sigma_{\alpha,\beta} = -\frac{1}{\Omega}\frac{\partial E_{total}}{\partial \epsilon_{\alpha\beta}} \quad (32)$$

The enthalpy decreases for positive strain and thus compressive strain is defined by the applied forces with a negative sign.

The stress-strain relations define the elastic phenomena and the linear elastic constants are given by

$$C_{\alpha\beta,\gamma\delta} = \frac{1}{\Omega}\frac{\partial^2 E_{total}}{\partial \epsilon_{\alpha\beta}\partial \epsilon_{\gamma\delta}} = \frac{\partial \sigma_{\alpha\beta}}{\partial \epsilon_{\gamma\delta}} \quad (33)$$

$C_{\alpha\beta,\gamma\delta}$ can be specified as 6x6 C_{ij} array for a general crystal using symmetry[101,102] and the notations *i* and *j* are defined in terms of Voigt's notation as

$1 = xx;\ 2 = yy;\ 3 = zz;\ 4 = xy;\ 5 = yz;\ 6 = xz$

A cubic crystal has only three independent constants, C_{11}, C_{12} and C_{44} while a wurtzite crystal has five independent constants namely, C_{11}, C_{12}, C_{13}, C_{33} and C_{44}.[48]

While linear elasticity constants have been discussed here, non-linear elasticity models provide higher order dependence on applied pressure. [103]

It is also worth noting that both the stress-strain relations to linear and non-linear terms can be observed in stress calculations. Also, stress along with applied strain, is being described by the derivatives. Moreover, for any strain, the atomic positions in the unit cell are fixed by non-zero (internal + externally applied) force. Thus, the finite theory of strains can be treated simply from the basic theory. In order to compute the stress and strain effects on the semiconductor materials under study, we utilized the Density Functional Theory and the theory has been explained in the next section.

2.2. Density Functional Theory

"Density functional theory (DFT) has long been the mainstay of electronic structure calculations in solid-state physics. (..) [The] approximate functionals were shown to provide a useful balance between accuracy and computational cost. This allowed much larger systems to be treated than by traditional ab-initio methods, while retaining much of their accuracy. Nowadays, traditional wavefunction methods, either variational or perturbative, can be applied to find highly accurate results on smaller systems, providing benchmarks for developing density functionals, which can then be applied to much larger systems." As stated by the author, K. Burke, in his book "*The ABC of DFT*".[104]

A totally unique method to transform any complex interacting problem to a much simpler non-interacting problem, the exceptional theory is applied in a wide array of diverse problems. One of the most common of them is the ground-state electronic structure problem.[105,106]

The Theory of DFT as projected by Hohenberg[105] and Kohn[107], Kohn and Sham[106] can be condensed in the following fundamental theorems.[108]

Theorem 1: ***"****For any system of interacting particles in an external potential, the interparticle potential is uniquely determined by the ground state charge density****".***

Thus the ground state charge density can ascertain the properties of a system.

Theorem 2: *"A universal functional of the energy F[n] in terms of density n(r) can be defined, valid for any external potential. Conversely for any particular potential, the*

exact ground state energy of the system is the global minimum value of this functional and the density n(r) which minimizes this functional is the exact ground state density".

Hence, the theorem, in simple words, affirms that the functional F[n] can characterize the ground state density effectively and hence the system properties. But the structure of the functional F[n] is yet to be determined.

The Kohn-Sham equations being self-consistent should be interpreted such that unique potential is formed from the final ground state electron density, employed at the beginning to find it.

Using the Born-Oppenhiemer approximation where the heavy nuclei are considered as fixed points, the ground-state electron problem is solved.[104]

For a spin system, which is non-degenerate, the Kohn-Sham equations can be shown as follows:

$$\left[-\frac{\hbar^2}{2m}\nabla^2 + V_H[n(r)] + V_{ion}[n(r)] + V_{xc}[n(r)]\right]\psi_i(r) = \varepsilon_i\psi_i(r), \qquad (34)$$

where $\left[-\frac{\hbar^2}{2m}\nabla^2\right]$ is the kinetic energy of the fictitious elements of non interacting nature,

$V_H[n(r)]$ is the Hartree potential, $V_{ion}[n(r)]$ is the ionic potential,

$V_{xc}[n(r)]$ is the exchange-correlation potential, ε_i is the eigenvalue,

and $\psi_i(r)$ is the eigenfunction of the fictitious elements (non-interacting).

The exchange-correlation potential V_{xc} is sketched as:

$$V_{xc}[n(r)] = \frac{\delta E_{xc}[n(r)]}{\delta n(r)} \qquad (35)$$

The exchange-correlation potential could be found out by a functional derivative of the density, only if the functional $E_{xc}[n(r)]$ was recognized. However as the outline of the functional is unknown, approximations produce adequate results.

The total electronic charge density is equal to $[\psi_i(r)]^2$.

In order to materialize an initial estimate, importance is needed equally to the basis set ($\emptyset_i$).

The Density Functional Theory, with a bright future, has the most important drawbacks as

1. The absence of the '*divine functional,*'[109] the exact exchange-correlation functional.
2. The proper scheme to obtain the ground state charge density is absent.

The outcome from DFT is dependent on the usage of exchange-correlation functional approximations.

The Kohn-Sham equation terms of V_H and V_{xc} are represented in different forms and provides the various aspects of DFT. As different approaches are available, it is highly questionable to determine the method with the finest outcome. A discussion on the benefits and the drawbacks of the different techniques is essential to have the complete representation.

2.2.1. Exchange-Correlation

The exchange-correlation potential illustrates the effects of the Pauli Exclusion Principle as well as the Coulomb potential, which is not a strain from sheer electrostatic interaction between the electrons.[110]

The many-electron system has an anti-symmetric nature of the wavefunction. This antisymmetry causes the spatial separation among the electrons having same spin. This very unique nature of the wavefunction eventually shrinks the repulsive Coulomb potential. The exchange energy is thus referred to as the energy minimization of the electronic system owing to the anti-symmetric wavefunction properties.

The spatial separation of the electrons with opposite spins minimizes the Coulomb energy of the electronic system. The electron correlation effect is neglected by the Hartree-Fock scheme. *"The difference between the many body energy of an electronic system and the energy of the system calculated in Hartree-Fock approximation is called the correlation energy*". [111]

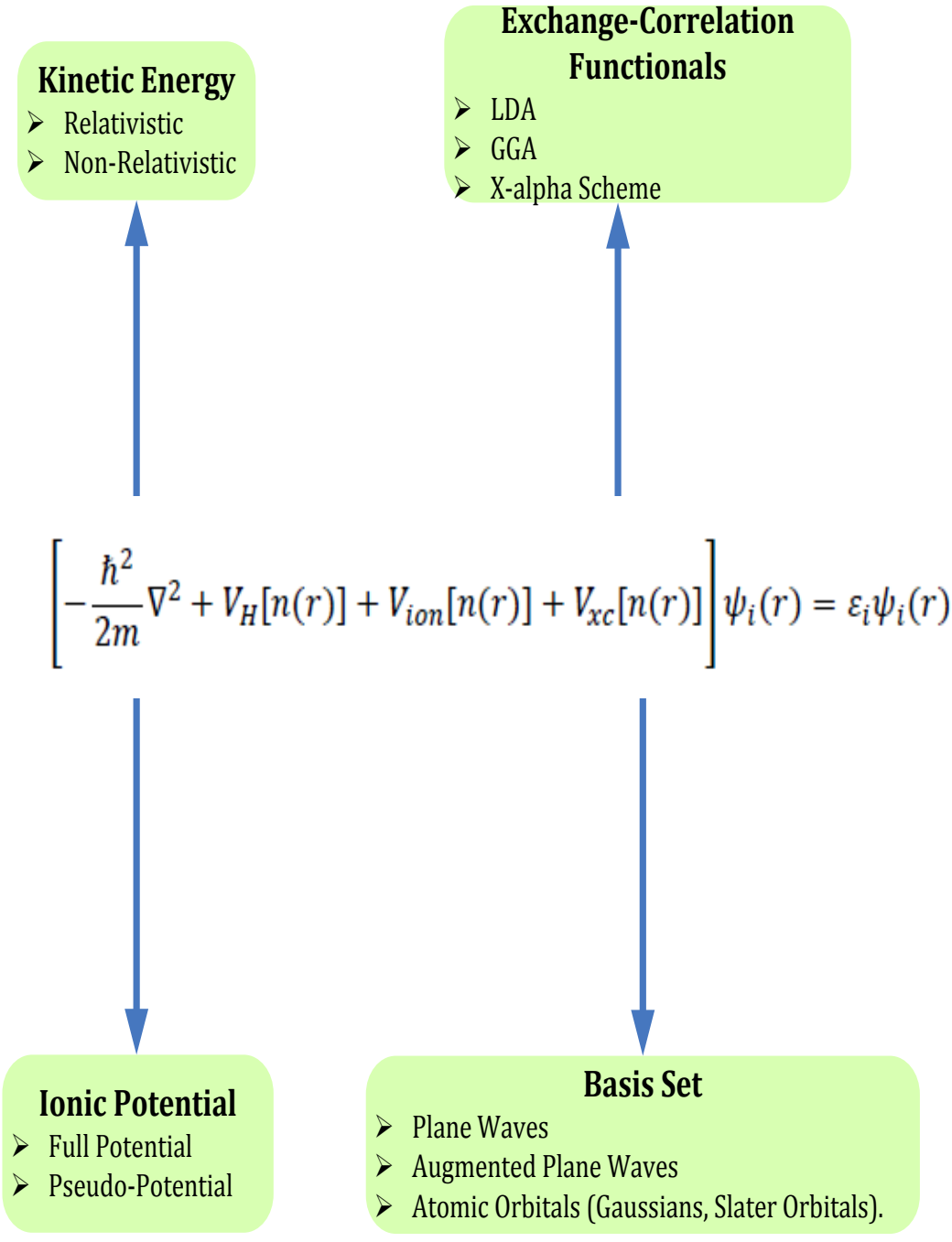

Figure 2.2.1-1: Density Functional Theory and its different aspects[112].

Determination of the correlation energy is remarkably complicated for complex systems. The exchange-correlation energy has been defined as a function dependent on the electron density. The simplest class of approximations is the Local Density **A**pproximation (LDA) which is suggested by Kohn-Sham (1965) and this approximation is the backbone of all the total-energy pseudopotential calculations.[111]

2.2.2. Local Density Approximation

The exchange-correlation functional is assumed to be the electron energy density of the system resembling that of a slowly varying homogenous electron gas in space.

The Local Density Approximation (LDA) is the simple scheme of the approximations. The functional is assumed to be the electron energy density of the system replicating that of a homogeneous electron gas.

"*It uses only the electron density, n(**r**), at a spatial point **r** to determine the exchange-correlation energy density at that point. The exchange-correlation energy density is taken to be that of a uniform electron gas of the same density. The exchange part of the functional is defined as the exact expression derived for a uniform electron gas106. The available versions of LDA differ only in their representation of correlation. All modern LDA correlation functionals are based on Ceperly and Alder's (CA's) 1980 Monte Carlo calculation[113] of the total energy of the uniform electron gas".*

-stated by the authors in the paper: "*Modelling Simul.Mater.Sci.Eng.13 (2005) R1- R31*".

Assuming the exchange-correlation energy in the LDA to be equal to the exchange-correlation energy for the uniform electron gas, the mathematical relation for the LDA functional is outlined as follows:

$$E_{xc}[n(r)] = \int \varepsilon_{xc}^{hom}[n(r)]n(r)\, d^3r \quad (36)$$

The analogous exchange-correlation potential is found from the derivative of the above density equation. Again, the mapping of the exchange correlation as a function of density and the exchange correlation as a function of the inter-electronic spacing is expressed by the following relation:

$$n(r)^{-1} = \frac{4\pi}{3} r_s^3 \quad (37)$$

The estimation of the correlation energy for a uniform electron gas has been calculated by Wigner.[114] The quantification has been done using an interpolation between the high density (r<1) and the low density (r>1) limits.

$$\varepsilon_c = 0.44/(r_s + 7.8) \text{ (In Hartree)} \quad (38)$$

Perdew-Wang[115] and Perdew-Zunger[116] parameterized the Ceperly-Alder (CA) correlation data in the high and the low density limits.[117]

An expression dependent on the distance between the two electrons has been derived by the Kohn-Sham for pure exchange.

$$\varepsilon_c = 0.4582/r_s \text{ (In Hartree)} \quad (39)$$

LDA disregards the correction terms in the exchange-correlation energy owing to the non-uniformity in the electron density. The computations performed using the LDA are known to give the proper results in spite of the imprecise quality of the approximation. It has been shown by Jones and Gunnarsson[118] that the Local Density Approximation (LDA) gives the correct sum rule for the exchange-correlation hole. Thus the LDA is shown to offer the single global minimum energy value for non-spin-polarized systems.[111]

All the different versions of LDA fluctuate only under the various portrayal of the correlation. Again, within the different functionals, when the surface energies and the properties of oxides need to computed, LDA always remains favoured over GGA, as LDA provides a better result.[119]

2.2.3. Pseudopotentials

The spatial distribution of the electronic charges of the valence electrons determines the ground state and the electronic properties of a system. The electronic wavefunctions can be defined using a unique set of the plane waves, as stated by the Bloch's Theorem. But the strongly bound orbitals of the core and also the rapid deviation of the valence electron wavefunction in the core region involve a huge set of plane waves to expand the electronic wavefunctions. Thus the computation process becomes highly expensive, being dependent on the number of electrons involved. The energy of the valence electrons is normally smaller than the energy of the core electrons by three orders of magnitude. Also the energy variation under the influence of bonding or the ionic configurations is deduced from the energy of the valence electrons. The computation of the total energy might not be precise but the variation in energy has a considerable consequence which leads to the importance of a pseudo-atom.

The pseudopotential is created by considering the pseudo wavefunctions and pseudo-particles to be alike all-electron wavefunctions and the electrons. Thus the pseudo-particles and the pseudo-wavefunctions are used in the calculation. Hence, the pseudopotential is typically the Coulombic interaction among the ionic core and the pseudo-electrons which forms an additional term to the Kohn-Sham Hamiltonian.

The wavefunction for a single particle is thus displayed as:

$$\emptyset = \psi + \sum_{core} \alpha_c \psi_c \quad (40)$$

where ψ is the wavefunction term for the concerned valence electron,

ψ_c is the wavefunction of the core electrons and

α_c maintains the orthogonality (hence no overlap) between ∅ and ψ_c

which follows: $$\langle \emptyset | \psi_c \rangle = 0 \quad (41)$$

Thus the Hamiltonian can be written down as the summation of the kinetic energy term and the term involving the pseudopotential.

$$H = KE_0 + v_{psp} + v_{Hartree} + v_{xc} \quad (42)$$

The pseudopotential must be equal to the actual potential in both spatial arrangements as well as in the absolute charge density magnitudes. The pseudopotential is developed such that the scattering properties as well as the phase shifts for the pseudo-wavefunctions remain similar to that of the valence wavefunctions of the ion and core electrons. The phase shifting property of the ion core is reliant on the angular momentum.

Hence, a local pseudopotential is defined by the pseudopotential which ignores the dependency on the angular momentum terms. So, the local pseudopotential represents the function dependent on the nuclear distance or, the difference among the wave vectors in the plane wave basis states.

The first order energy dependency of ion-scattering from the ion core has been shown to be correct when the pseudo and the real wavefunctions are identical outside a core region.[120] The norm-conserving pseudopotentials are members of the class of the local

and non-local pseudopotentials where both the real and the pseudo wavefunctions are identical outside the core region.

The pseudopotential is fabricated by performing an all-electron calculation utilizing an exchange-correlation functional on a segregated atom in both the ground and excited state. Self-consistent calculations provide an estimate of the electronic density, the eigenvalue and also the eigenfunction. Further computation is carried out involving the valence electrons, with the exchange-correlation functional remaining intact and the adjusted parameters (the convergence norm being generally the cutoff radius for the core). The outcomes are tweaked to replicate the all-electron calculation results for the eigenvalue and the eigenfunction. The pseudopotential for the atom is determined from the set of parameters obtained from the best optimized values. The better the optimized values, the better estimate of the exact nature of the wavefunction can be obtained.

The proper figure of merit of the quality of pseudopotential is to measure how well the outcomes of the identical all-electron calculations are replicated. Thus, the interchangeability of the pseudopotential created sufficient interest, ensuing different categories of pseudopotentials. First-principle, Empirical, Semi-empirical and model techniques are widely considered and utilized.

The experimental data for the band structure is used to best fitting for the empirical pseudopotentials, but the drawback is the interchangeability and the fitting parameters which are employed to elucidate the properties. The finest outcomes will always be observed for the fitted parameters when a property is in direct relation to an algorithm. The Semi-Empirical and model methodology allows bit more flexibility while fitting in the algorithm.

First principle pseudopotentials (Ab-initio) employ the Density Functional Theory to obtain a pseudopotential which has been discussed in the report.

The earliest Pseudopotential created by the first principle method diverges when the cut-off radius is in close proximity of the nucleus (i.e. r→0). This class of pseudopotentials are generally referenced as the hard-core pseudopotentials. Instead, the soft-core pseudopotentials[120] provide converged results in the vicinity of the nucleus (i.e. r→0).

The methodology to create the pseudopotentials includes the generalized norm-conserving pseudopotentials (GNCPPs) of Hamman,[120] soft-core pseudopotentials by Troullier-Martin[121] and the non-norm-conserving ultrasoft pseudopotentials by Vanderbilt.[122] During the analysis of the soft-core pseupotentials, the electron density is generally assumed to be split up into the core and the valence electrons. Hence, the overlapping characteristic of the two electron states, valence and core, has been ignored. But the Non-Linear core correction[123] augments a fractional core correction charge to the exchange-correlation functional with the semi-core charge density because of the non-interacting core and valence electrons and is applicable to all different types of pseudopotential schemes.

Thus, the ultrasoft pseudopotentials are favoured to give the enhanced outcomes even for an additional expense in computation.

2.2.4. Plane Wave Basis Sets and Bloch's Theorem

The prominent difficulty of dealing with the infinite number of electrons moving in a stationary field of an infinite number of ions can be solved using the Bloch’s Theorem. The wavefunction of the infinite crystal can be expressed as the domain wavefunctions of the reciprocal space vectors (Bravais lattice). The Bloch's theorem employs the periodic

property of a crystal and hence the infinite number of wavefunctions decreases to the total number of electrons in the unit cell.

Thus the wavefunction can be expanded as the product of a wave resembling term and a component involving the cell periodicity[141]:

$$\psi_{i,k}(r) = f_i(r)e^{(ik.r)} \quad (43)$$

The first part of the expression represent the cell periodic term of the wavefunction. This term can be further expanded using plane waves. The finite plane waves have the wave vectors replicating the reciprocal lattice vectors (G) of the crystal. The expanded form is as follows:

$$f_i(r) = \sum_G c_{i,G} e^{(iG.r)} \quad (44)$$

Thus the electronic wavefunction (each) can be represented as the summation of the plane waves:

$$\psi_{i,k}(r) = \sum_G c_{i,k+G} e^{\{i(k+G).r\}} \quad (45)$$

Thus, with the help of the Bloch Theorem, the problem of the infinite electrons is linked with the identical problem for the reciprocal space vectors (at the first Brillouin zone). The solution is to calculate the finite wavefunctions at specific periodic cells, k, of the Brillouin zone.

The Kohn-Sham equation is needed to be solved at each of the k-points to converge (under the consideration of large k-points). This leads to a highly expensive computational process. The wavefunctions for the entire k-space can be imitated using the wavefunctions at single specific k-points in such a way that an identical wavefunction is made available at an adjacent reciprocal k-space.

Different approaches (Chadi-Cohen,[124] Monkhorst-Pack[125]) have been recommended to attain more accurate space charge density of the system by sampling the reciprocal space and finally interpreting the Kohn-Sham equation at unique k points of the Brillouin Zone. The more dense the k-point grid is, the lesser the error margin but with a higher computational expense.

The k-point wavefunctions are built up using a unique plane wave basis set including the infinite plane waves. The impact of the plane waves with lesser kinetic energy is much higher than the waves with higher kinetic energy. Thus the plane wave basis set can even be reduced to a finite extent.

In principle the plane wave series is condensed to include the terms up to a certain defined energy (cut-off energy). The kinetic energy can be found from the second order derivative of the wavefunction, and is evaluated from the Bloch's wavefunction expansion as:

$$Kinetic\ Energy = \frac{\hbar^2}{2m}|k+G|^2 \leq Cut-off\ Energy \qquad (46)$$

The limiting factor for the cut-off energy saves the computational expense as the amount of the plane waves per k point is also reduced. An error is generated in the overall energy of the system due to the lesser number of the G-vectors employed. The error can be reduced using the higher cut-off energy during computation.

The plane wave basis set reduces the Kohn-Sham equations to a much simpler set and the process becomes highly efficient. The reciprocal space replication can be done using the Fast Fourier transformation technique to convert from the real to the reciprocal space.

Furthermore, the absence of any Pulay terms[126] and the stresses in the Hamiltonian make the computed Hellmann[127]-Feynman[128] force to be equivalent to the derivative of the overall energy relative to the ionic position. The convergence criterion being simple is dependent solely on the cut-off energy.

A highy converged outcome involves large number of plane waves even with all the advantages of employing the plane waves. Although the local atomic wavefunctions are not exactly matched in the plane waves, useful information can be extracted from the projection analysis using the Gaussian or Wannier functions.

2.2.5. Scalability

The computational process of the Kohn-Sham equations is an expensive method. The computing power of 17.59 PetaFLOPS/s (quadrillions of calculations per second) has already been achieved in 2012 and research is going on to reach 1 ExaFLOPS (10^{18}) (one quintillion FLOPS) by 2018. This level of computational power has been absent even in the last decade. The future of the Density Functional Theory looks really bright with better and higher available computing power, larger system sizes can be considered for calculation. The diagonalisation of the Hamiltonian with N plane waves requires an Order of complexity of $O(N^3)$. The memory requirement involves an Order of Complexity $O(N^2)$. The orthogonalisation process with N_b number of bands has the order of $O(NN_b^2)$, which is highly expensive.

However the computational power must be utilised wisely and the convergence criterion must be utilised through the proper utilization of the minimum feasible basis set and the k point grids.

2.2.6. Application

The Density Functional Theory (DFT) can be used in studying the ground state properties of different metals, insulators and semiconductors. The theory can also predict the properties for the complex materials (e.g. proteins, carbon nanotubes) along with the regular bulk materials. The current work focuses on the structural properties of the III-N semiconductors.

The pseudopotential techniques in the LDA and GGA are applied by Froyen-Cohen,[129,130,131] Yin-Cohen,[132,133] Garcia[134] to analyse the structural properties of cohesive energy, bulk modulus as well to compute the pressure dependency during phase transitions in different semiconductors (e.g. GaAs, AlAs, GaP, AlP, Si). Interesting information has also been shown by Garcia *et al*[134] in his paper which deems that the results of LDA for the semiconductors are not getting improved by the GGA usage. The computation of the electronic charge dispersal and the total energy curves for the crystal phases of GaAs and Si proves the reliancy on the atomic volume by Yin and Cohen.[132,133] The bandstructures and the fundamental properties of the III-Ns are estimated with the help of DFT by Yoshida *et al.*[135] The elastic properties of the wurtzite class of semiconductors are computed using DFT by Xiao-Ju *et al.*[136] DFT has also been employed to verify the dependency of the different structural properties of GaN on the strain.[137] The pressure dependency of the electronic, structural and optical properties using the pseudopotential approach for the Gallium Nitride (GaN) has been assessed by G.Y. Gao *et al.*[138] More importantly, Wang-Ye[139] illustrated, through the usage of DFT, the dependency of the phonon and the dielectric properties of the III-nitrides, arsenides and phosphides on pressure. Thus the widespread applications of the Density Functional Theory (DFT) suggest that the predicted material properties can be accurately computed and are the reason for the popularity of the theory.

2.3. k·p Method and Deformation Potential

We need to be able to compare our piezoelectric fields with experiment. That's not easy as direct comparison is impossible. Experimental results are on bandstructure and wavefunctions. We then need to calculate those as a function of piezoelectric field to compare. How do we do it? Methods available are empirical pseudopotential and k·p. The k·p method is widely used model for calculations not only for bulk semiconductors but also lower dimensional systems such as QW, QD and NWs because the calculations are quite precise near the bandedges there. The k·p method is limited to semiconductors, direct or indirect bandgap. It is chosen because of ease and also the already available code[140] . The process is started with the known form of the bandstructure at the bandedges and then applying the perturbation theory the bands away from the high symmetry points are described.[141]

As the work is more focussed on understanding the semiconductor properties, we consider a semiconductor with a bandedge at k_0. We further assume that the Bloch functions and eigenvalues are known for the bandedge, thus the equation:

$$\left[\frac{p^2}{2m} + V(r)\right] \cdot \psi_n(k_0, r) = E_n(k_0) \cdot \psi_n(k_0, r) \qquad (47)$$

As in compound semiconductors mostly, the maximum of the valence band and the minimum of the conduction band occur at the same point in the k-space - at the Gamma point. Such semiconductors are called direct-gap semiconductors. In case of an indirect bandgap semiconductor, the minimum of the conduction band is reached at some other point in the k-space. Thus in most cases, k_0 is the Gamma point (Γ= [000]) in the Brillouin zone and we are considering the direct bandgap semiconductors here.

Assuming each of the band eigenfunction away from Gamma (Γ= [000]) can be expressed as a linear combination of the Bloch functions at Gamma:

$$\psi(k,r) = \sum_n b_n(k)\psi_n(k_0,r)\cdot e^{i(k-k_0)\cdot r} \quad (48)$$

where b_n are the expansion coefficients, to be determined. The secular equation is given as $$\left\|\langle e^{i(k-k_0)\cdot r}\psi_{n'}(k_0,r)|H-E|e^{i(k-k_0)\cdot r}\psi_n(k_0,r)\rangle\right\| = 0 \quad (49)$$

We can rewrite this equation through a simple expansion for the central cell section of the Bloch states.

As $p = -i\hbar\nabla$ and $\nabla\left(e^{i(k-k_0)\cdot r}\psi_n\right) = e^{i(k-k_0)\cdot r}(\nabla + i(k-k_0))\psi_n,$

Substituting, we have

$$\left[\frac{p^2}{2m}+V(r)\right]\psi_n(k,r) = \left[\frac{\{p+\hbar(k-k_0)\}^2}{2m}+V(r)\right]e^{i(k-k_0)\cdot r}\psi_n(k_0,r)$$

$$= e^{i(k-k_0)\cdot r}\left[\frac{\{p+\hbar(k-k_0)\}^2}{2m}+V(r)\right]\psi_n(k_0,r)$$

$$= e^{i(k-k_0)\cdot r}[\frac{\hbar^2}{2m}(k-k_0)^2+\frac{\hbar}{m}(k-k_0)\cdot p+E_n(k_0)]\psi_n(k_0,r) \quad (50)$$

The determinant of the eigenvalue then becomes

$$\left\|\langle\left[\frac{\hbar^2}{2m}(k-k_0)^2+E_n(k_0)-E\right]\delta_{n\prime n}+\frac{\hbar}{m}(k-k_0)\cdot P_{n'n}(k_0)\rangle\right\| = 0 \quad (51)$$

where $P_{n'n}$ is the momentum matrix element inbetween the various band edge states

$$P_{n'n} = \int \psi^*_{n\prime}(k_0,r)\, p\, \psi_n(k_0,r)\, d^3r \quad (52)$$

We can now explicitly write the Energy vs k relationship to second order in perturbation theory:

$$E_n(k) = E_n(0)+\frac{\hbar^2k^2}{2m}+\frac{\hbar^2}{m^2}\sum_{n\neq n\prime}\frac{|k\cdot\langle\psi_{n\prime}(k_0)|p|\psi_n(k_0)\rangle|^2}{E_n(0)-E_{n\prime}(0)} \quad (53)$$

The above equation can also be expressed in terms of effective mass m* as

$$E_n(k) = E_n(0)+\sum_{i,j}\frac{\hbar^2}{m^*_{i,j}}k_i\cdot k_j \quad (54)$$

where

$$\frac{m}{m^*_{i,j}} = \delta_{i,j} + \frac{2}{m}\sum_{n\neq n'} \frac{\langle \psi_{n'}(k_0)|p_i|\,\psi_n(k_0)\rangle\langle \psi_{n'}(k_0)|p_j|\,\psi_n(k_0)\rangle}{E_n(0)-E_{n'}(0)} \tag{55}$$

The equation is valid for conduction band edge and the split-off bands.

For the conduction band, we get

$$E_c(k) = E_c(0) + \frac{\hbar^2 k^2}{2m^*_c} \tag{56}$$

and

$$\frac{1}{m^*_c} = \frac{1}{m} + \frac{2p^2_{cv}}{m^2} * \frac{1}{3}\left(\frac{2}{E^\Gamma_g} + \frac{1}{E^\Gamma_g+\Delta}\right) \tag{57}$$

where E^Γ_g is the band gap at the Gamma point and Δ is the Heavy Hole-Split-Off band separation.

k.p methods are also known as effective mass methods.

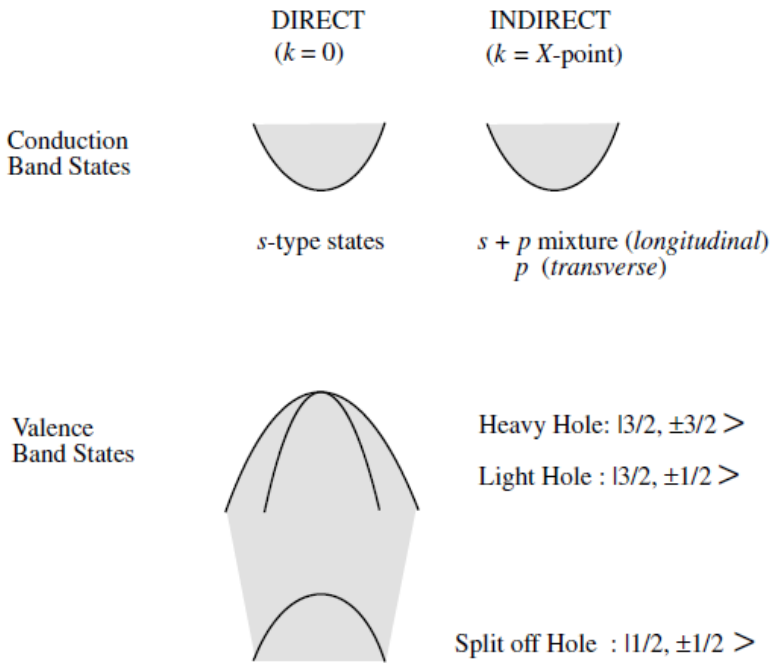

Figure 2.3-1: A schematic showing the nature of the central cell symmetry at the bandedges of direct and indirect semiconductors. Reproduced from Ref [141]

The valence band has the Heavy Hole (HH), Light Hole (LH) degeneracy at the top of the valence band. As we move away from the Gamma point, the strong interaction inbetween the two states gives rise to a splitting among the bands. The split-off (SO) band can also impact the valence band states, as it is much closer to the HH and LH.

Ignoring the conduction band effects in the determinant equation, we finally get a 6x6 eigenvalue equation. Symmetry is considered to get the nonzero elements and form of the matrix equation.

The matrix will now be expressed in the basis of the valence spin dependent p-type states (not exactly p but close: they are combinations of pure angular momentum p states).

The list of the quantum numbers involved:

L	**Spin**	**Angular Momentum**	**Projection of J**
1	**±1/2**	**J**	**m_j**
p_x	↑	3/2	+3/2
p_x	↓	3/2	+1/2
p_y	↑	3/2	-1/2
p_y	↓	3/2	-3/2
p_z	↑	1/2	+1/2
p_z	↓	1/2	-1/2

The Kohn-Luttinger[142] Hamiltonian is then used to describe the Hamiltonian for the valence band in the basis of the angular momentum numbers.

$$H_{KL} = -\begin{bmatrix} H_{HH} & b & c & 0 & ib\sqrt{2} & -i\sqrt{2}c \\ b^* & H_{HH} & 0 & c & -iq & i\sqrt{3}b/\sqrt{2} \\ c^* & 0 & H_{LH} & -b & -i\sqrt{3}b^*/\sqrt{2} & -iq \\ 0 & c^* & -b^* & H_{LH} & -i\sqrt{2}c^* & -ib^*/\sqrt{2} \\ -ib^*/\sqrt{2} & iq & i\sqrt{3}b/\sqrt{2} & -i\sqrt{2}c & H_{SO} & 0 \\ i\sqrt{2}c^* & -i\sqrt{3}b^*/\sqrt{2} & iq & ib\sqrt{2} & 0 & H_{SO} \end{bmatrix} \quad (58)$$

where

$$H_{HH} = \frac{\hbar^2}{2m}\left[(\gamma_1 + \gamma_2)\left(k_x^2 + k_y^2\right) + (\gamma_1 - 2\gamma_2)k_z^2\right]$$

$$H_{LH} = \frac{\hbar^2}{2m}\left[(\gamma_1 - \gamma_2)\left(k_x^2 + k_y^2\right) + (\gamma_1 + 2\gamma_2)k_z^2\right]$$

$$H_{SO} = \frac{(H_{HH}+H_{LH})}{2} + \Delta$$

$$b = \frac{-\sqrt{3}i\hbar^2}{m}\gamma_3\left(k_x - ik_y\right)k_z$$

$$c = \frac{-\sqrt{3}\hbar^2}{2m}[\gamma_2\left(k_x^2 - k_y^2\right) - 2i\gamma_3 k_x k_y$$

$$q = (H_{HH} - H_{LH})/\sqrt{2}$$

$\gamma_1, \gamma_2, \gamma_3$ are the Luttinger parameters or bandstructure parameters.

Because the SO splitting is usually large in most semiconductors, this 6x6 matrix could be reduced to a 4x4 for the LH and HH bands. Thus, the appropriate Hamiltonian for the HH and LH states is then

$$H = -\begin{bmatrix} H_{HH} & b & c & 0 \\ b^* & H_{HH} & 0 & c \\ c^* & 0 & H_{LH} & -b \\ 0 & c^* & -b^* & H_{LH} \end{bmatrix} \tag{59}$$

In terms of fitting parameters, the strain Hamiltonian for the HH and LH states, known as deformation potentials, can be written with the following form:

$$H = -\begin{bmatrix} H_{HH}^{\varepsilon} & H_{12}^{\varepsilon} & H_{13}^{\varepsilon} & 0 \\ H_{12}^{\varepsilon\ *} & H_{LH}^{\varepsilon} & 0 & H_{13}^{\varepsilon} \\ H_{13}^{\varepsilon\ *} & 0 & H_{LH}^{\varepsilon} & -H_{12}^{\varepsilon} \\ 0 & H_{13}^{\varepsilon\ *} & -b^* & H_{HH}^{\varepsilon} \end{bmatrix} \tag{60}$$

where the matrix elements are as follows:

$$H_{HH}^{\varepsilon} = a_d\left(\varepsilon_{xx} + \varepsilon_{yy} + \varepsilon_{zz}\right) - b_d[\varepsilon_{zz} - \tfrac{1}{2}\left(\varepsilon_{xx} + \varepsilon_{yy}\right)]$$

$$H_{LH}^{\varepsilon} = a_d\left(\varepsilon_{xx} + \varepsilon_{yy} + \varepsilon_{zz}\right) + b_d[\varepsilon_{zz} - \tfrac{1}{2}\left(\varepsilon_{xx} + \varepsilon_{yy}\right)]$$

$$H_{12}^{\varepsilon} = -d_d\left(\varepsilon_{xz} - i\varepsilon_{yz}\right)$$

$$H_{12}^{\varepsilon} = \frac{\sqrt{3}}{2}b_d\left(\varepsilon_{yy} - \varepsilon_{xx}\right) + id_d\varepsilon_{xy}$$

Here, a_d, b_d and d_d are the valence band deformation potentials.

For wurtzite structures, the strained Hamiltonian and the deformation potentials are used from the paper of S. L. Chuang and C. S. Chang[143]

Common multi-band k·p models include the 6-band model which includes only valence bands, while the 8-band and 14-band models include valence as well as conduction bands. We can replicate the bulk bandstructure more precisely with the multiband k·p Hamiltonians than the standard 6- or 8-band Hamiltonian. Even with models including a large number of bands (≥15 or 30 after incorporation of the spin degree of freedom), can reproduce the bulk band structure throughout the whole Brillouin zone. [144]

We use the kppw code, developed by our collaborator, Prof. Stanko Tomić at University of Salford, to perform the k·p calculations. The bulk bandstructure parameters extracted from ab initio codes like CASTEP and CRYSTAL are used in the kppw code. The code defines matter at an atomistic level of theory and provides comprehensive information regarding the cell periodic functions along with other important parameters like band edge effective masses, bulk dipole matrix elements and various energy gaps, extracted at various levels of DFT theory. In the kppw code those parameters are used for parametrization of 8-, 14- or 16-band bulk Hamiltonian. The need for effective masses gradually disappears with more bands being included. The code determines the Hamiltonian of the nanostructure as quantum well and quantum dots or any other random arrangement of those including the effects of surface interfacing, strain, piezoelectric and spontaneous polarization field. This code has been utilized for calculations of quantum dots energy bandstructure[144] and in Figure 2.3-2, the wavefunctions for top six hole states and bottom five electron states for a square-based pyramidal InAs/GaAs QD using different models has been illustrated. To identify the effect of the Hamiltonians beyond

the standard 8-band one, model system using several different Hamiltonians with a different level of sophistication has been performed and in Figure 2.3.2, (a)-(g) resemble

(a) The 8-band k·p Hamiltonian consisting of the kinetic part only (without the spin-orbit interaction and strain),

(b) The 8-band k·p Hamiltonian consisting of the kinetic part with the spin-orbit interaction taken into account (but without strain),

(c) The 8-band k·p Hamiltonian consisting of the kinetic part with the interface band-mixing effects taken into account (but without spin-orbit interaction and strain),

(d) The standard 8-band k·p Hamiltonian consisting of the kinetic part with the spin-orbit interaction and strain, as well as the strain-induced linear piezoelectric potential,

(e) The 8-band k·p Hamiltonian consisting of the kinetic part with the spin-orbit interaction and strain, as well as the strain-induced piezoelectric potential and the interface Hamiltonian,

(f) The 14-band k·p Hamiltonian consisting of the kinetic part only (without the spin-orbit interaction and strain)

(g) The 16-band k·p Hamiltonian consisting of the kinetic part only (without the spin-orbit interaction and strain)

(h) The 14-band k·p Hamiltonian consisting of the kinetic part with the spin-orbit-interaction and strain (as well as the strain-induced piezoelectric potential).[144]

While we can observe the effect of different components, the results in Figure 2.3.2 (e) represent the strong influence of piezoelectricity; we are interested in exploiting the non-linear piezoelectricity and the corresponding impact on the electronic properties.

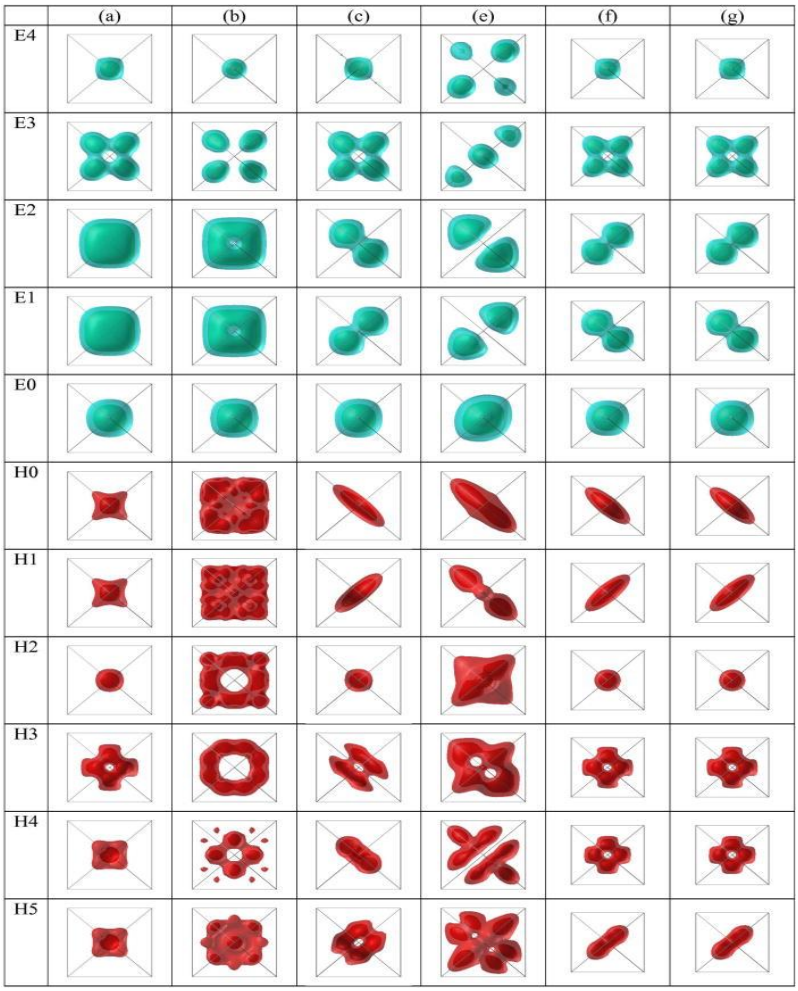

Figure 2.3-2: Wavefunctions of hole and electron states in InAs/GaAs QD using different k·p models (Reproduced from Ref. [144])

The kppw code has also been utilized for electronic structure calculations in QWs[145] and intermediate band solar cells[146]. We will discuss more about our outcomes from the k·p calculations in the next chapter.

3. Non Linear Piezoelectricity

In this chapter, we will discuss non-linear piezoelectricity in the semiconductor materials III-Vs, III-Ns and ZnO. We will also discuss the potential exploitation of the non-linear piezoeffects in devices and applications in later sections of this chapter.

3.1. Review of Previous Works

3.1.1. ZB III-V Semiconductors

3.1.1.1. Introduction

Direct bandgap semiconductors such as GaAs and InAs have the innate ability to easily absorb and emit light and they are extremely popular in device fabrication of photovoltaic solar cells, sensors and LEDs. The piezoelectric effect[147,148]in those semiconductors originates from the lattice mismatch, when two semiconductors are grown epitaxially on top of each other, because such layer by layer growth introduces shear strain. Such effect can be easily observed in QWs grown on (111) substrates, NWs and QDs via the off-diagonal strain tensor. The Piezo effect in QWs and QDs has been demonstrated to be the source of experimentally observed anisotropies in recent years. [59,60,149] A brief review of past work from Grundman *et al*[61], Davies[62] and Stier *et al*[63] shows that only first-order PZ effects have been considered and the experimental PZCs of bulk GaAs and InAs are used while for alloyed semiconductors (InGaAs), the PZCs are typically obtained through linear interpolation of bulk values.

Bester *et al*[150] first made the point that substantial errors are observed in PZ field calculation when the second-order effects are neglected. Later, Migliorato *et al* [151]

demonstrated that the estimates of first- and second-order piezoelectric tensor can be realized through the use of a semiempirical model reliant on input from Density Functional Theory (DFT). According to the work from Bester *et al*,[150] the second-order PZC for InAs and GaAs are predicted to be -0.230 and -0.115 (C/m^2) respectively while Migliorato *et al*[151] points out that there is no reasonable explanation as to why they should be different from the reported experimental value of -0.045 and -0.16 (C/m^2) respectively. Furthermore the method of Migliorato *et al*[151] appears to provide significant improvement compared to that of Bester *et al*[150] (who uses the Linear Reponse technique) and achieves better agreement with the experimental data for $In_xGa_{1-x}As/GaAs$ QWs.

3.1.1.2. Piezoelectric Quantum Well

As discussed before, the polarization components are given by $P_i = e_{ijk}\varepsilon_{jk}$, with ε_{jk} being the strain tensor and e_{ijk} the piezoelectric coefficients. The shear strain (ε_{ij}), the off-diagonal component of strain tensor, is in a direct relation with the PZCs (e_{14}, e_{25}, e_{36}). Due to the presence of ZB symmetry, the expression can be reduced to one PZC value, e_{14}. The expression for the piezoelectric charge originating from the presence of shear strain is then given by

$$\rho(r) = -\nabla \cdot (2e_{14}(r) \cdot [\varepsilon_{yz}(r)i + \varepsilon_{xz}(r)j + \varepsilon_{xy}(r)k]) \qquad (61)$$

From the strain tensor, it is evident that the off-diagonal values of the strain tensor are non-zero for strain in [111] direction. Interestingly, the PZ polarization created in a QW in [111] direction can be inferred from measured quantities. This is where the modelling and detailed study of the polarization in III-V semiconductors is of fundamental importance. The main aspect of studying such QW nanostructure grown on (111) substrates is the presence of an induced PZ field in the growth direction, which simplifies the modelling of experimental data. The results of previous experiments involving photocurrent measurements reveal that the e_{14} values[152,153,154] physically found from

measurement cannot be fitted to the linear interpolation of bulk values of InAs and GaAs for an alloy composition of x <0.3. The modelling results of the photocurrent measurement under low-temperature measurement from Hogg[152]and Sanchez-Rojas[153] reported upto 70% of the interpolated value. On the other hand, under slightly higher room-temperature condition, Cho[156] reported 80% of the interpolated value. Assuming the QW has an ideal structures with sharp interfaces and the width and alloy composition as the fitting parameter, these researchers[152,153,154,155,156] detrermined the e_{14} reduction form electrooptical data.

The work of Ballet *et al*[157] revisited previous work on a QW structure grown on (111) susbstrate with Molecular Beam Epitaxy (MBE) process, but included in the model the presence of Indium segregation at the interfaces. These calculations,[157] later repeated by Migliorato *et al*,[151] demonstrated that the correct value is 86% of the interpolated value, at x= 0.15, corresponding to the value of -0.124C/m^2. Therefore a much smaller reduction than initially hypothesized.

3.1.1.3. Piezo coefficients with Harrison's Model

The conclusions reported in the previous section are valid only within an Indium concentration range $0 \leq x \leq 0.2$ for $In_xGa_{1-x}As$ semiconductor. The large lattice mismatch between two epitaxially grown semiconductors has a negative impact on the crystal quality and no experimental structures with x>0.4 have ever been grown. Different works [152, 153, 154 ,155 ,156, 157 ,158 ,159] have all concluded that it was not possible to have an estimate of e_{14} when x>0.4. Later, Migliorato *et al*[151] obtained estimates of e_{14} for x>0.2 by detailed observation of the reduction of the interpolated values within what is generally referred to as Harrison's model.[57] In order to utilize this method Migliorato *et al*[151] needed first to solve a significant shortcoming: the fact that the calculated piezoelectric charge e_p^* is generally in poor agreement with the experimental value leading to erroneous

determination of the PZC. The way round it was to accept the need for one parameter to be chosen and adjusted to have a better agreement of the theoretical value to the experimental one. Harrison's model of piezoelectricity[57] is very simple, easy to manipulate and can also provide possible analysis of general problems using simple ideas describing the dominant mechanism for stable structures.

The fundamental unit of the III-V semiconductors are tetrahedron, each containing five atoms that build up the crystal structure. One such tetrahedron is subjected to atomic level stress which is then directly related to the hydrostatic strain, the diagonal components of the strain tensor and is responsible for the atomic displacement *dk*. Under influence of very small shear strain (ε_{ij}<0.02), the off-diagonal quantity, very little or negligible atomic displacement is observed.

Kleinman's[58] theoretical work first proposed that the relaxation occurs perpendicular to the direction of the shear strain. The displacement *dk* can be thought as to be linear in the strain and thus, the Kleinman parameter ζ, normally found < 1, is a constant. The Kleinman parameter was assumed to be a constant for a given material before Rideau *et al*[160] and Migliorato *et al*[151] showed otherwise. Fig. 3.1.1.3-1 shows the characterization of ζ on strain parameter ε_{ij} and ε_k respectively from Migliorato's *et al*[151] demonstrating the strong dependence of *dk* on ε_k and a very little dependence on ε_{ij}, for ε_{ij}<0.02.

In the same work, Migliorato *et al*[151]reported for the first time an alternative method to the linear response technique for the evaluation of non-linear effects. He used the tight binding formalism of Harrison[57] but calculated the material dependent parameters using DFT and density functional perturbation theory (DFPT). In Harrison's model[57] the polarization in the $\hat{x}_i$ direction, for any atom at the centre of a tetrahedron, is written as:

$$P_{\hat{k}} = Z_H^* \delta k + \beta \sum_{q=1}^{4} \left(\overrightarrow{r_q} \cdot \hat{k}\right) \delta R_q \qquad (62)$$

where Z_H^* is the atomic effective charge associated with both the cations and anions in the crystalline structure, δk the separation between anions and cations due to internal relaxation of the sublattices and the term β being the transfer parameter.

The term δk can be also written in terms of the so called Kleinman parameter ζ, the shear strain $\varepsilon_{\hat{t}\hat{\jmath}}$ and the lattice parameter *a* as:

$$\delta k = \frac{a\zeta\varepsilon_{\hat{t}\hat{\jmath}}}{4} \tag{63}$$

The transfer parameter is related to the more common encountered polarity α_p, the measure of electric dipole associated with the bond, and this relation is given by $\beta=2\alpha_p(1-\alpha_p^2)$. The two terms in the equation are normally of opposite sign and the polarization is a delicate balance between the difference between the direct dipole ($Z_H^*\delta k$) and bond contributions ($\beta\sum_{q=1}^{4}(\overrightarrow{r_q}\cdot\hat{k})\delta R_q$) resulting from the fact that each of the four atoms located adjacent to the center atom of a tetrahedron is at a distance r_q. δR_q represents the differences in r_q due to the rearrangement of atoms when the crystal structure undergoes internal relaxation due to shear strain in the plane orthogonal to the vector $\hat{k}$.

From Eqs. (62) and (63), it is possible to derive the linear piezoelectric coefficient e_{14}, by dividing Eq. (62) by 2Ω, twice the volume per atom and multiplying times the electron charge *e* and explicitly writing the bond dipole in terms of δk:

$$P_{\hat{k}} = \frac{e}{2\Omega}\frac{a\varepsilon_{\hat{t}\hat{\jmath}}\zeta}{4}\left(Z_H^* - \frac{2}{3}\beta\frac{(1-\zeta)}{\zeta}\right) = e_{14}\varepsilon_{\hat{t}\hat{\jmath}} \tag{64}$$

All the parameters Z_H^*, ζ and β must be known accurately for the model to yield accurate results.[161]

Migliorato *et al*[151] advocated the use of DFT and DFPT to evaluate not just the bulk values but also their dependence on the diagonal components of the strain tensor.

The plane wave calculations in Migliorato *et al*[151] was performed with a set of pseudopotentials provided by Troullier-Martin scheme[162] while the internal sublattice displacement ζ can be calculated provided a strain tensor is given. With a Monkhorst-Pack grid[163] of 4×4×4 and planewave cutoff energy of 50 Ryberg, the lattice constant of InAs and GaAs are reported to be 11.37 and 10.48 a.u respectively.[151]

A simple strain tensor is applied, with an added small shear strain (γ<0.01) onto the hydrostatically compressed lattice. The cation and anion are then relaxed to minimize the cohesive energy. The strain tensor and the simple relation of strain and ζ is given as follows:

$$Strain\ tensor = \begin{pmatrix} 1-\varepsilon & \gamma/2 & \gamma/2 \\ \gamma/2 & 1-\varepsilon & \gamma/2 \\ \gamma/2 & \gamma/2 & 1-\varepsilon \end{pmatrix} \quad (65)$$

$$\delta r = \sqrt{3}\frac{a\zeta\gamma}{4(1+\varepsilon)} \quad (66)$$

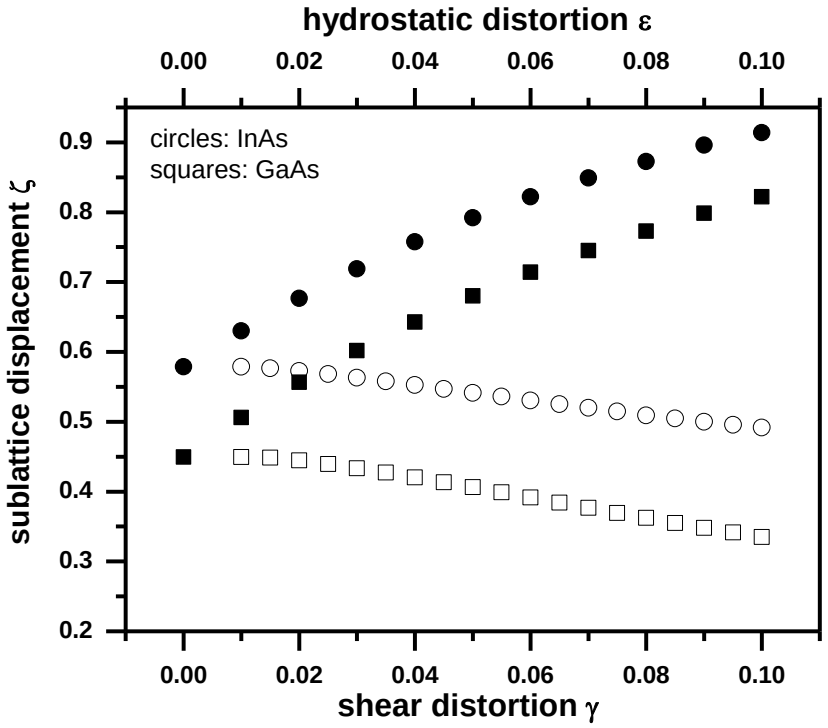

Figure 3.1.1.3-1: Strain dependence of Kleinman parameter of GaAs and InAs (Reproduced from Ref. [151]

The behaviour of ζ on shear and hydrostatic strain is interesting, keeping one of the quantities variable and another fixed. According to the figure 3.1.1.3-1, increasing hydrostatic strain ε increases the ζ parameter but increment in the shear strain γ reduces ζ concluding that piezoelectric charges get decreased with reduced ζ.[151] Also, Wang and Ye[164] noticed and reported the strain dependence on ζ. Further DFT calculations[165] have also been performed to study the influence of combinations of hydrostatic and shear strain. The author[151] reported the strain dependence of ζ for the first time.

3.1.1.4. Bond Polarity, Atomic Effective Charge

The most recent calculation for bond polarity α_p, reported by Wang and Ye[165], involved DFPT to compute the transverse effective charge and then the determination of α_p from tight-binding expression linking the two quantities. The reported values for GaAs and InAs are 0.423 and 0.49 respectively, which are also validated by Shen *et al*,[166] with the bond orbital approximation. Wang and Ye[165] also reported the effect of hydrostatic strain to be a linear reduction of the polarity with an estimated decay of -0.95ε and -1.08ε and for GaAs and InAs respectively. The atomic effective charge Z_H^* is obtained using the expression from Harrison's work of $Z_H^* = Z - 4 + \alpha_p$, where Z is the chemical species column number, extrapolated from experimental data of Falter *et al.* [167] but, this approach is found to overestimate Z_H^*.

Several other studies[166,167,168] have also reported Z* values with much close agreement with experimental data. But even using the crude approximation of $Z^* = Z_H^* + 4\beta/3$ it has been difficult to provide widely agreed values of Z_H^*, with a spread of theoretical and experimental data and a simple approach is used.

DFT calculated α_p and ζ values (using the DFT calculated lattice constants) and Z_H^* are being used as a fitting parameter in Migliorato *et al*[151] to ensure a precise bulk GaAs and

InAs e_{14} PZC experimental value of -0.16 and -0.045 (C/m^2) respectively from equation (64). This process gives the corresponding values of Z_H^* to be 0.43 and 0.54 and found in reasonable agreement with the values of 0.323 and 0.612 respectively from a basic tight-binding calculation.

Table III: Parameters used in calculations from Migliorato's *et al*[151]

			$\boldsymbol{\eta}$	**Second Order:**		
		Bulk	**distortion**	$\mathbf{X\eta + X^2\eta^2 + X^3\eta^3}$		
				$\mathbf{X}$	$\mathbf{X^2}$	$\mathbf{X^3}$
$\boldsymbol{\zeta}$	**GaAs**	0.455	$\boldsymbol{\varepsilon_{\alpha\alpha}}$	5.88	-28.99	75.03
			$\mathbf{2\varepsilon_{\alpha\beta}}$	-0.23	-19.98	102.75
			$\boldsymbol{\varepsilon_{\alpha\alpha} * 2\varepsilon_{\alpha\beta}}$	1.87	47.55	255.05
	InAs	0.58	$\boldsymbol{\varepsilon_{\alpha\alpha}}$	5.42	-25.84	51.67
			$\mathbf{2\varepsilon_{\alpha\beta}}$	-0.45	-11.86	70.78
			$\boldsymbol{\varepsilon_{\alpha\alpha} * 2\varepsilon_{\alpha\beta}}$	1.73	31.37	166.61
$\boldsymbol{\alpha_p}$	**GaAs**	0.423[165]	$\boldsymbol{\varepsilon_{\alpha\alpha}}$	-0.95	0	0
	InAs	0.49[165]	$\boldsymbol{\varepsilon_{\alpha\alpha}}$	-1.08	0	0
$\boldsymbol{Z_H^*}$	**GaAs**	0.43	$\boldsymbol{\varepsilon_{\alpha\alpha}}$	$-4[\alpha_p(bulk) - \alpha_p(\varepsilon)]$		
	InAs	0.54	$\boldsymbol{\varepsilon_{\alpha\alpha}}$			

In first approximation

$$Z_H^* = Z - 4 + 4\alpha_p \quad (67)$$

In reality, this expression overestimates Z_H^* and the difference of $Z_H^* - Z_H^*(\varepsilon)$ gives a reasonable approximation for hydrostatic strain effects and hence the strain dependence of Z_H^* can be derived from the expression for $\alpha_p(\varepsilon)$.

3.1.1.5. Compositional Disorder Effect

The linear interpolation scheme has been shown to give wrong estimates for quantities like polarity as shown by Bouarissa[169] work with empirical pseudopotential within virtual crystal approximation. This is demonstrated through the overestimation of values by 8% compared to the interpolated value of $In_{0.5}Ga_{0.5}As$. In Figure 3.1.1.7.1, such effect has been illustrated and can be associated with the random alloy compositional disorder. Migliorato *et al*[151] demonstrates the expression for composition-dependent polarity and the derived bowing parameter as $\alpha_p = 0.423 + 0.161x + 0.000148x^2$ (68)

As elastic properties for $In_xGa_{1-x}As$ follows Vegard's law, Kleinman parameter ζ does not require any bowing parameter. Rather, Z_H^* needs such scheme to obtain its strain dependence and is achieved by substituting α_p from Eq (68) into Eq (67).[151]

3.1.1.6. Piezo coefficient evaluation

The evaluation of the PZC in the case of hydrostatic and shear deformed crystal requires the modification of equation (64). The polarization needs to be divided by (1-ε) to yield the desired quantity. The equivalent cell volume under strain to first order is given by V' that is found equivalent to V (1+3ε). The theoretical value has been directly compared to the existing experimental one from Migliorato *et al.*[151] The parameter ζ and lattice constant a for intermediate compositions of $In_xGa_{1-x}As$ has been computed through linear interpolation using the scheme described in previous section for Z_H^* and α_p. The values obtained for the PZC is linear as can be observed from Figure 3.1.1.3-1 but found dissimilar to the simple interpolated values between the e_{14} bulk values. Strain effect has also been incorporated to compare with the experimental data and therefore included the

effect of strain for a uniform epitaxial layer of $In_xGa_{1-x}As$ grown directly on GaAs (111) substrate as a function of the composition (x).

The changes in the interpolated parameters ζ, Z_H^* and α_p under strain is calculated using the relationship as defined in earlier section. The modified Eq (64) is then used to evaluate the PZC e_{14} and the results of the scheme have been summarized in Table III.

3.1.1.7. Important Discussion Review

This section will discuss the works and the differences of the two models from Migliorato *et al*[151] and Bester *et al*[150]. Firstly, it should be highlighted here that photocurrent spectrum fitted results from Migliorato *et al*[151] are different to the linear terms from Bester *et al*[150]. The reader should have understood by now that the PZC e_{14} value is considerably modified under strain. Migliorato *et al*[151] demonstrate major influence of the incremental shear and hydrostatic strain on the elastic properties, in particular the Kleinman parameter.

Also, it should be noted that figure 3.1.1.7-1 shows the PZC as a function of strain that a sufficiently thick epitaxial layer of uniform composition (x) would undergo when grown on GaAs (111) substrate and not to be confused to be a simple function of composition, which is misunderstood by many readers. Therefore, the unstrained bulk value for InAs in figure 3.1.1.7-1 does not match exactly with the plotted quantity of the strained InAs on GaAs (111).

Major differences between the two models of Migliorato *et al*[151] and Bester *et al*[150] lie in the linear term and the former model[151] is applied to reproduce the experimental value of e_{14}. As no such process has been applied in latter work[150], the linear term predicts larger estimates.

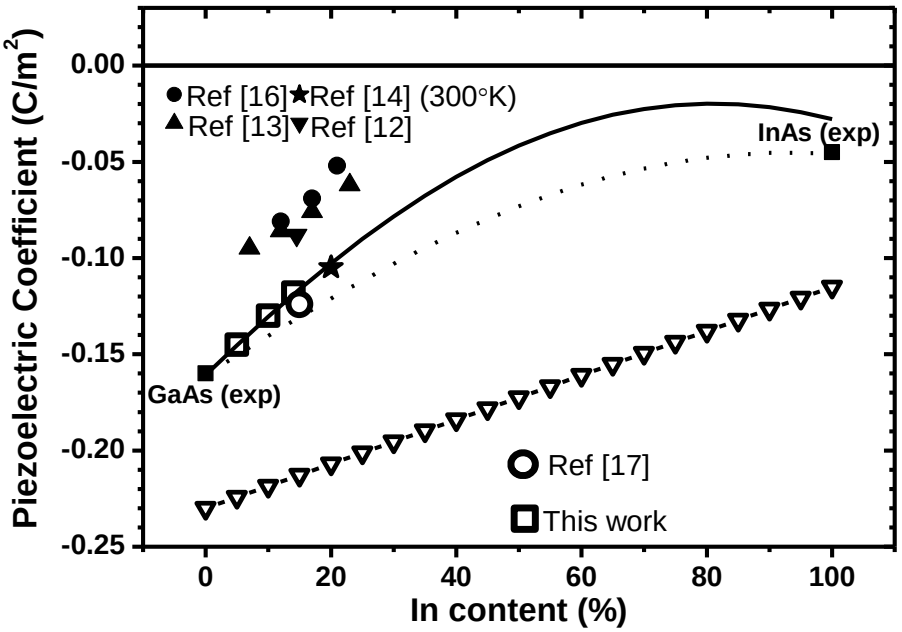

Figure 3.1.1.7-1: Piezoelectric coefficient dependence on In compositions (Reproduced from Ref. [151])

The PZ field is often reported to be in the range of 120-165 kV/cm for In composition in the QW between x=0.15 and x=0.21. [152,153,154,155,156,157]

Such measurements rely on the assumption that the maximum of the oscillator strength is reached at flat band condition when the applied bias compensates the internal PZ field. However, it is assumed that a constant bandgap exists across the well region, while if there is a nonuniform stoichometric profile, then, at different applied bias, the maximum of the oscillator strength and the flat-band condition can be observed.

But the PZ field estimates are somewhat unreliable and there is clearly a conflict on the field predictions when varying In compositions is considered.[151] In case of 10nm wide QW with x=0.15, the PZ field is estimated to be 220kV/cm using theoretical expression[141]. Even with an assumption of 30% reduction of e_{14} value from the interpolated values the field is reported to be 165kV/cm. Furthermore, a field of 190kV/cm is instead expected when 16% reduction in e_{14} is used while including diffused

interfaces (In segregation). This suggests the importance of In segregation for the huge discrepancy in the reported values of e_{14}. An 11nm wide of QW, for x=0.15, is predicted to have a PZ field of 80 kV/cm from Bester *et al*[150] and the value is much smaller than the reported value[152,153,154] and is 42% of the most realistic estimate[157]. Instead, Migliorato *et al*[151] predicts the PZC which results in a much better match in the PZ field estimation to Ballet's work[157]. This is clearly owing to the similar methodology used in evaluating the field and the values of e_{14} are identical.

3.1.2. Previous Work: pseudomorphically grown semiconductors

3.1.2.1. Bond Polarity and Kleinman

In the work of Garg *et al*[170], an extension of the previous work from Migliorato *et al*[151] was presented, where the strain dependence was extended from a selected number of strains to a full set of strains for biaxially strained materials.

The bond polarity value α_p was evaluated using DFPT and the CASTEP software package, with the applied strain tensor on the unit cell is given by

$$Tensor = \begin{pmatrix} 1-\varepsilon_{xx} & 0 & 0 \\ 0 & 1-\varepsilon_{yy} & 0 \\ 0 & 0 & 1+\varepsilon_{zz} \end{pmatrix} \quad (69)$$

Diagonal strain components have non-zero values only, with strain ranges from - 0.01 to 0.1. The strain components in the x direction and y-direction are identical while it is different across the z direction.

A k-point grid of 4x4x4 is used with LDA and ultrasoft pseudopotential[171] and a 1000eV energy cutoff to get fairly good convergence of 1% error for different combinations of k-point grid and cutoff energy. The bond polarity is obtained by evaluating the following

expression with $\Delta Z = 1$for III-V compounds from the born charge calculated from DFPT for GaAs and InAs as a function of the parallel or perpendicular strain component.

$$Z^* = -\Delta Z + 4\alpha_p + 4\alpha_P(1 - \alpha_p^2) \quad (70)$$

Figure 3.1.2.1-1 reveals the strain dependence of the bond polarity α_p value of GaAs and InAs, following the repeating trend of the Born effective charge Z*. Hence with hydrostatic pressure, a decrease in the bond polarity α_p is observed.

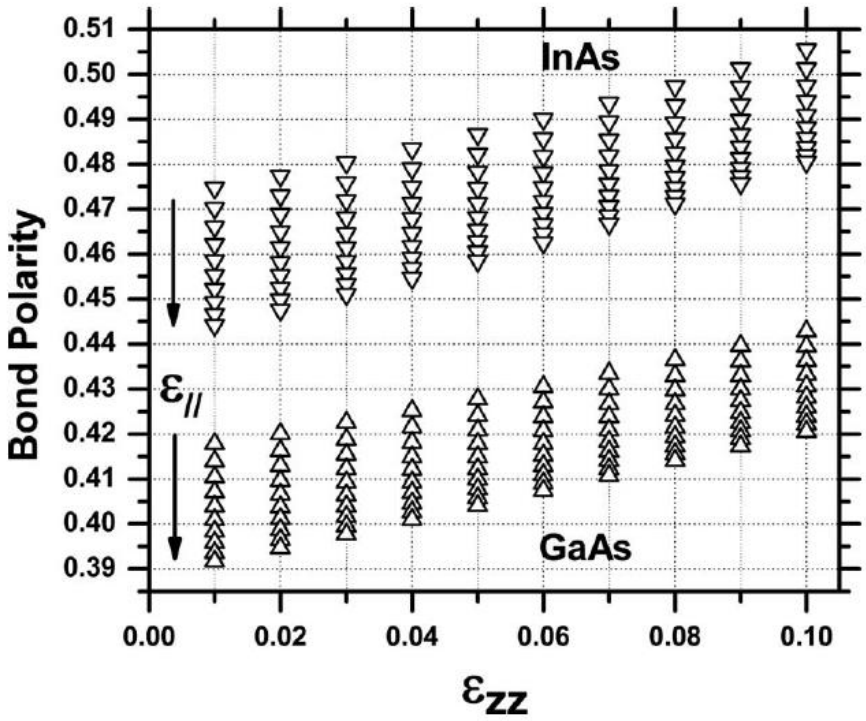

Figure 3.1.2.1-1: Bond Polarity plots of GaAs and InAs. Dependence of the bond polarity on the applied strain for GaAs and InAs. For each value of the perpendicular strain, each point corresponds to a different value of the parallel strain that ranges from -0.01 to +0.1, (top to bottom) as indicated by the arrows. (Reproduced from Ref[170])

The DFT calculations for the Kleinman parameter were performed with the CASTEP[172] software package, applying the following strain tensor

$$Tensor = \begin{pmatrix} 1 - \varepsilon_{xx} & \gamma/2 & \gamma/2 \\ \gamma/2 & 1 - \varepsilon_{yy} & \gamma/2 \\ \gamma/2 & \gamma/2 & 1 + \varepsilon_{zz} \end{pmatrix} \quad (71)$$

Since the atomic displacement is obtained from the DFT calculations in fractional coordinate, the data is converted to the Cartesian coordinate before working out the internal sub-lattice displacement ζ. This is the equivalent of the Kleinman parameter ζ, which is evaluated with following equation

$$dr = \frac{1}{(1+\varepsilon)} \frac{\sqrt{3}}{4} a\, \gamma\, \zeta \qquad (72)$$

where *dr* is the displacement of the cation to anion, a being the lattice constant, *γ/2* the off-diagonal tensor or shear strain and *ε* the hydrostatic strain.

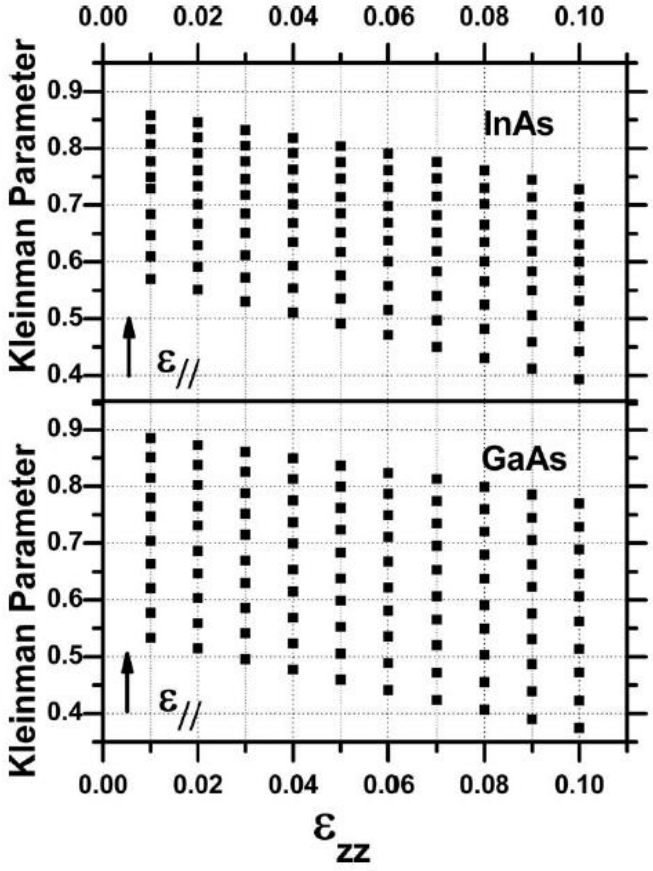

Figure 3.1.2.1-2: Kleinman parameter plots of GaAs and InAs (Reproduced from Ref[170])

The Kleinman parameter ζ, vs perpendicular strain ε_{zz} and parallel strain for GaAs and InAs is demonstrated in Figure 3.1.2.1-2, showing a unique trend, of strong strain (hydrostatic) dependence of Kleinman parameter.

3.1.2.2. Piezoelectric coefficients

Garg *et al*[170] also calculated the PZCs by fitting of polynomials to the DFT data and found that once all second order effects are incorporated, a single PZC will not be able to reproduce the strong dependence on the combination of strain in in-plane and off growth direction plane. In fact, a random combination of diagonal components of strain (e_{xx}, e_{yy} and e_{zz}) requires the usage of 3 coefficients in e_{14}, e_{25} and e_{36}. In this work, second order effects are considered in 3 effective coefficients. However, we can still obtain the full second order PZ tensor if the polynomial fitting is performed. However in Garg *et al*[170], this was not performed as combinations of strain involving e_{xx}=e_{yy} were included in the calculations. The part of the motivation of the work was to extend the previous work to a more generalized strain tensor to obtain the second order PZCs.

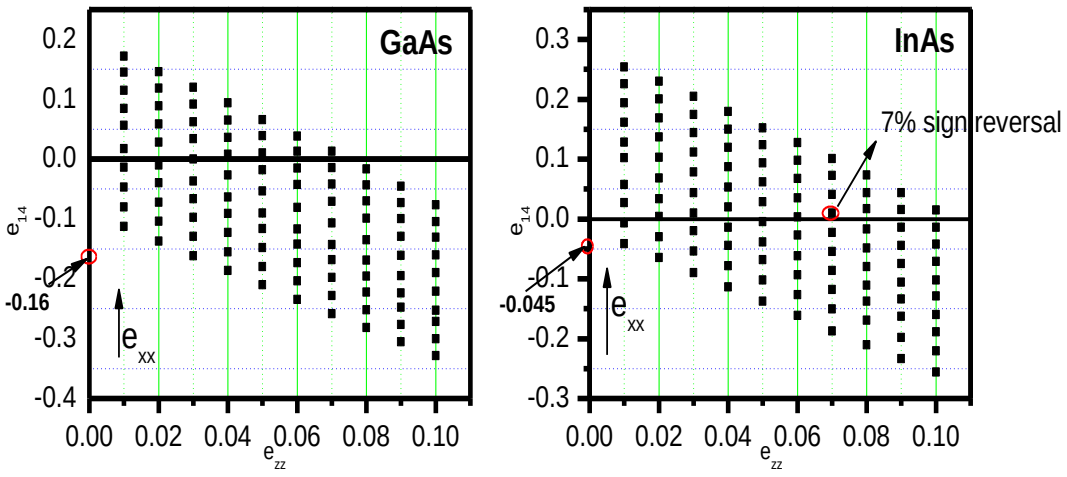

Figure 3.1.2.2-1: Piezoelectric coefficients plot for GaAs and InAs

In Figure 3.1.2.2-1, the PZCs are shown to be highly strain dependent in x, y and z direction. When InAs grows epitaxially on top of GaAs there is 5-7% of lattice mismatch and at that point, PZC is observed to turn from negative to positive giving a 7% sign reversal.

3.1.3. More recent work on non-linear piezoelectricity in ZB materials

In recent work from Tse *et al*[173], the linear, quadratic and cubic piezoelectric coefficients related to diagonal terms of the strain tensor for both GaAs and InAs zincblende crystals are estimated, given in Table IV. After conditions are imposed on the coefficients based on the cubic symmetry of the crystal, a reduced set of PZCs for the fitting equation is found:

$$e'_{lm} = e_{lm} + \sum_{n=1}^{3} e_{lnm}\,\varepsilon_n + \sum_{n\le n'=1}^{3} e_{lnn'm}\varepsilon_n\varepsilon_{n'} + \sum_{n\le n'\le n''=1}^{3} e_{lnn'n''m}\varepsilon_n\varepsilon_{n'}\varepsilon_{n''}, \quad (73)$$

The magnitude of these extra terms are assessed and it is concluded that while linear and quadratic terms are likely to necessitate inclusion even in the limit of small strain, cubic terms should only be included when the material undergoes significant (around 10%) strain.

Table IV: Linear and non-linear coefficients obtained from DFT data. For second and third order terms the parameters are invariant upon cyclic permutation of the *n* indexes.

Parameter			GaAs	InAs
e_{lm}			-0.160	-0.045
e_{lnm}	l=n	$e_{114}=e_{225}=e_{336}$	-0.666	-0.653
	l≠n	$e_{124}=e_{235}=e_{316}$	-1.646	-1.617
		$n \Leftrightarrow n'$		
$e_{lnn'm}$	l=n=n'	$e_{1114}=e_{2225}=e_{3336}$	-0.669	-3.217
	l=n≠n'	$e_{1124}=e_{1134}=e_{2215}=e_{2235}=e_{3316}=e_{3326}$	-2.694	-5.098
	l≠n=n'	$e_{1224}=e_{1334}=e_{2115}=e_{2335}=e_{3116}=e_{3226}$	-1.019	1.590
	l≠n≠n'	$e_{1234}=e_{2135}=e_{3126}$	-5.636	-1.962
		$n \Leftrightarrow n' \Leftrightarrow n''$		
$e_{lnn'n''m}$	l=n=n'=n''	$e_{11114}=e_{22225}=e_{33336}$	-0.840	21.063
	l=n=n'≠n''	$e_{11124}=e_{11134}=e_{22215}=e_{22235}=e_{33316}=e_{33326}$	-0.241	12.112
	l≠n=n'=n''	$e_{12224}=e_{13334}=e_{21115}=e_{23335}=e_{31116}=e_{32226}$	-9.168	-15.072
	l≠n=n'≠n''	$e_{12234}=e_{21135}=e_{31126}$	-1.471	-7.450
	n≠n'≠n''	$e_{11234}=e_{21235}=e_{31236}$	-4.725	-4.909

This section completes the review of previous works and from the coming section, the results of the current work with thorough discussion is presented.

3.2. Results on III-Nitride Semiconductors

Among III-V semiconductors, the III-N family is the one for which piezoelectricity influences more the optical and electrical properties.[174] This is because the piezoelectric coefficients (PZCs) are typically one order of magnitude larger than other III-V materials[47] and because the polarization vector is in most cases parallel to the growth direction.[175] The calculation of PZ properties in semiconductors is often affected by uncertainties in the correct values of the PZCs and in the case of wurtzite (WZ) crystals by the additional problem of determining the spontaneous polarization (P_{sp}) component.[47] However for III-N second order PZCs had not yet been reported before this work, making it difficult to assess the influence of second order piezoelectricity in nanostructures.

3.2.1. DFT Calculations

The elastic deformation and Z*, for both the bulk and strained cases, were evaluated by using planewave pseudopotential, with pseudopotentials derived with the Troullier-Martin scheme,[162] density functional theory in the local density approximation (DFT-LDA)[116] and density functional perturbation theory (DFPT), with pseudopotentials derived with the Hamann scheme,[176] within the CASTEP[172] code. Single-particle orbitals expressed in a plane-wave basis set with kinetic energy of up to 10^3 eV, and Brillouin zone summations of up to 10x10x6 Monkhorst-Pack k-point grids[163] were sufficient to converge the simulations below a remaining error of about 1% for multiple combinations of k-point grids and kinetic energy.

The dynamic effective charge was computed from the Born charge matrix, studied via the Berry phase approach[177] by applying a finite electric field perturbation in periodic boundary conditions. The matrix was then diagonalized and an average of the eigenvalues was taken as the effective charge. Both its bulk and strain dependence were determined in the same way.

WZ crystals are characterized by 3 independent quantities: the a in-plane, the c off-plane lattice parameters and u, the deformation from the ideal structure. The u parameter is at the origin of the P_{sp} effect as even in the absence of external strain the tetrahedrons are asymmetric, resulting in only 3 of the 4 bonds being equal in length to each other. Strain induced polarization arises from additional modifications of the cation positions relative to the anions under the effect of external pressure. One major advantage of the present approach is that both the spontaneous and strain induced polarization effects are described within the same model; hence the results we will present for the PZCs and the P_{sp} are uniquely linked. Furthermore only one PZC (e_{31}) was used as input, while the other ones (e_{33} and e_{15}) are calculated.

3.2.2. Linear Piezoelectric coefficients

The DFT calculated equilibrium values for a, c and u are presented in Table V for GaN, AlN and InN, together with Z* and the resulting bond polarity α_p. The results of our calculations yielded similar values to those reported earlier.[47,178] In the same table we report the experimental values of e_{31} used to fit Z_H* in our models, together with the obtained values of Z_H* which are much smaller than those of Z*, as explained earlier. Z_H* is the atomic charge, already explained in more detail in section 1.3.

The prediction of our model shows a substantial agreement with reported experimental values of e_{33} for bulk III-N (data in brackets). For e_{15} instead our predictions are always slightly larger than previously proposed values. It is also worth noting that the sign of e_{15} as predicted by our model is negative for all III-N materials studied. In the literature both positive[51,179] and negative[180] values of e_{15} have been reported, but we have identified this as being the result of a misprint contained in Muensit *et al*[51] when reporting the experimental values from Tsubouchi and Mikoshiba.[52]

Table V: Physical parameters of Group-III Nitrides (GaN, AlN and InN) calculated in this work. In brackets comparison with other calculated or experimental values.

Parameters	***GaN***	***AlN***	***InN***
a (Å)	3.155	3.063	3.523
c (Å)	5.149	4.906	5.725
u (Å)	0.376	0.382	0.377
Z*	2.583	2.553	2.850
α_p	0.517	0.511	0.578
Z^*_H	0.70	0.85	0.65
P_{sp} (C/m^2)	-0.007(-0.029_{th})[47]	-0.051 (-0.081_{th})[47]	-0.012 (-0.032_{th})[47]
e_{31}(C/m^2)	-0.55 (-0.55_{exp})[51]	-0.6 (-0.6_{exp})[51]	-0.55 (-0.55_{exp})[53]
e_{33} (C/m^2)	1.05 (1.12_{exp})[51]	1.47 (1.50_{exp})[51]	1.07 (0.95_{exp})[53]
e_{15} (C/m^2)	-0.57(-0.38_{th})[180]	-0.6 (-0.48_{exp})[52]	-0.65 (-0.44_{th})[180]
e_{311}(C/m^2)	6.185	5.850	5.151
e_{333}(C/m^2)	-8.090	-10.750	-6.680
e_{133}(C/m^2)	1.543	4.533	1.280

The frequently cited work of Bernardini and Fiorentini[47] reported the value of Muensit *et al*[51] rather than the original experimental work and since many authors referred to their work[180] when listing PZCs, the error propagated. The compilation from Vurgaftman and Meyer[181] also contains the erroneous positive sign. We have shown in our previous work on zincblende GaAs and InAs[151] that Z_H* needs to be roughly 25% of the value of the dynamic effective charge (Z*) in order to obtain values of the PZ polarization in agreement with experiment.

3.2.3. Internal Displacement (u) and Effective Charge (Z*)

We examined the strain dependence of the internal displacement parameter (u), to observe the impact of combinations of perpendicular strain and isotropic parallel strain.[182] The dependence of *u* on *a* is illustrated in fig.3.2.3-1.

In Figure 3.2.3-1 we demonstrate the distribution of the internal displacement parameter (u) with parallel and perpendicular strain (varying from -10% to 10%) calculated with parameters from our model.[183]

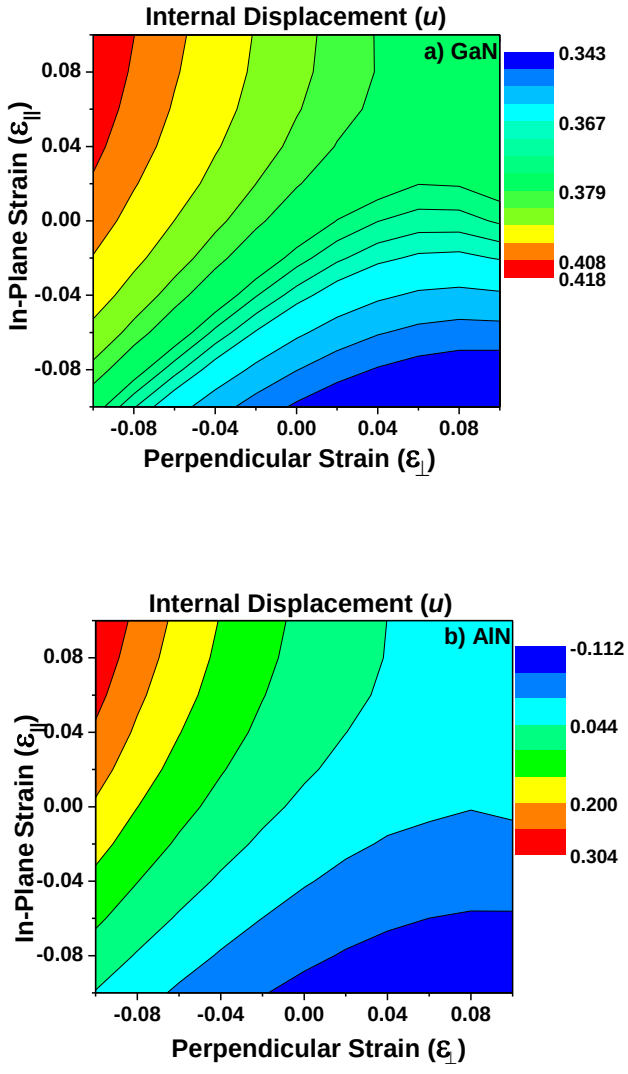

Figure 3.2.3-1: Strain dependence of internal displacement parameter (u) as a function of in-plane and perpendicular strain (from -0.1 to 0.1 in steps of 0.02) for a) GaN, b) AlN and c) InN respectively. Reproduced from work in Ref [182]

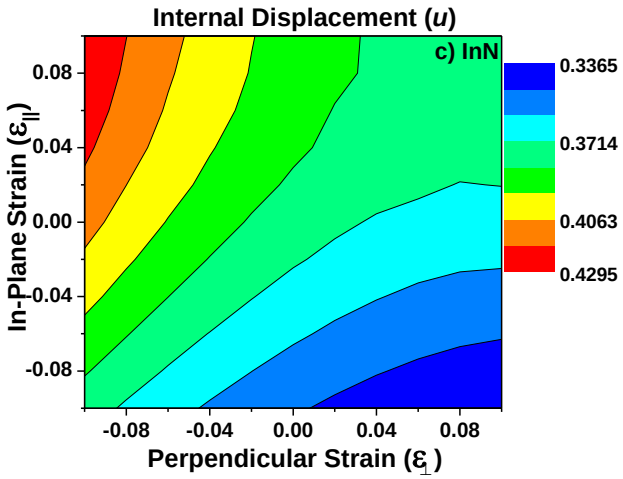

The results are quite interesting as we can observe a wide variation of the u parameter with strain and can be tuned for different combinations of strain applied on the system.

Also, we tried to investigate the strain dependence of Z* for all III-N materials for various arrangements of strain along in-plane and perpendicular to growth plane directions.

The outcomes of the Z* calculations reflect an unusual trend of non-linearity of dependence on strain and is valid in all three materials, namely GaN, AlN and InN.

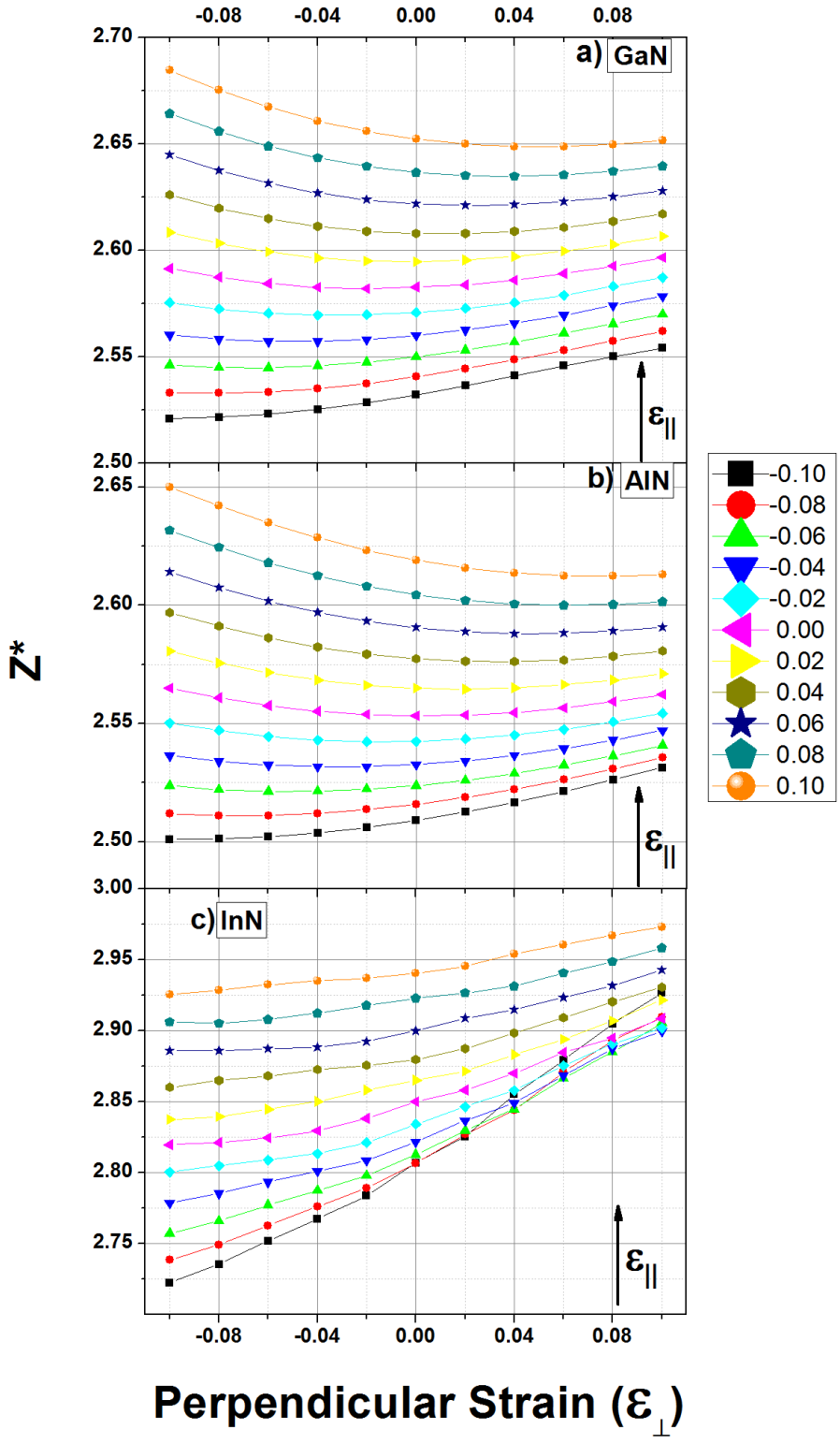

Figure 3.2.3-2: Z* as a function of perpendicular strain (from -0.1 to 0.1 in steps of 0.02) along with in-plane strain, following similar steps as perpendicular strain, for a) GaN, b) AlN and c) InN respectively. The legend define the different values of in-plane strain.

We have observed similar trends in polarization as well and contrary to linear trends, Z* also shows dependence of second order effects on strain. Figure 3.2.3-2 resembles the strain effects on Z* for strain along perpendicular as well as in-plane strain varying ±10% with steps of 2%.

The effective charge was used in our model later on to evaluate the bond polarity:

$$Z^* = 4\alpha_p + 4\alpha_p(1 - {\alpha_p}^2) - \Delta Z \quad (74)$$

with $\Delta Z = 1$.

3.2.4. Spontaneous Polarization

The most striking difference between our predictions and earlier reports (data in brackets in Table V) is however the values of the P_{sp}, for which no direct experimental data is available. The calculation of the P_{sp} followed exactly the same methodology used for determining the PZCs once the value of Z_H* was identified. The values that we calculated are between 25% and 65% of the values reported in the literature.[47,180] This is not surprising since often the P_{sp} has been calculated using a simple dipole model with charges equal to the transverse effective charge (Z*). The simple dipole model is equivalent to the first term in our model derived from Harrison's original formulation.[57] Since in our model we use Z_H*, the atomic charge, while earlier work tended to use Z* (which is roughly 3-4 times larger) our values are proportionally smaller. The problem that calculating both the PZCs and P_{sp} using Z* leads to grossly overestimated PZCs has been pointed out by Bernardini and Fiorentini.[47] Furthermore we note the existence of experimentally extrapolated values of the P_{sp} [184,185,186] which are substantially smaller than those given in the literature.[47,180]

3.2.5. Strain dependence of the polarization

We also studied the strain dependence of the total polarization (strain induced plus P_{sp}), to determine whether the second order PZ effect in the strain has relevance to WZ crystals. Non-linear polarization effects have already been reported for the III-N semiconductors,[187,188] however, to the best of our knowledge, no comprehensive list of second order PZCs has been reported.

Our previous work on ZB InGaAs[151,170] showed that second order effects in the strain arise from a non-linear displacement of the interpenetrating cation and anion fcc sublattices. Such non-linearity was revealed in our previous work even using DFT-LDA. Furthermore the effective charges and hence the bond polarity also appear to have a second order dependence on the strain, though the effect is weaker. In WZ crystals such behaviour is also present leading overall to a non-linear behaviour of the total polarization.

In Figure 3.2.5-1 we show the total polarization as a function of combinations of parallel and perpendicular strain (varying from -0.1 to 0.1) calculated with our model (circles) and compared with the predictions from the linear model (dashed lines) using parameters compiled by Bernardini and Fiorentini.[47]

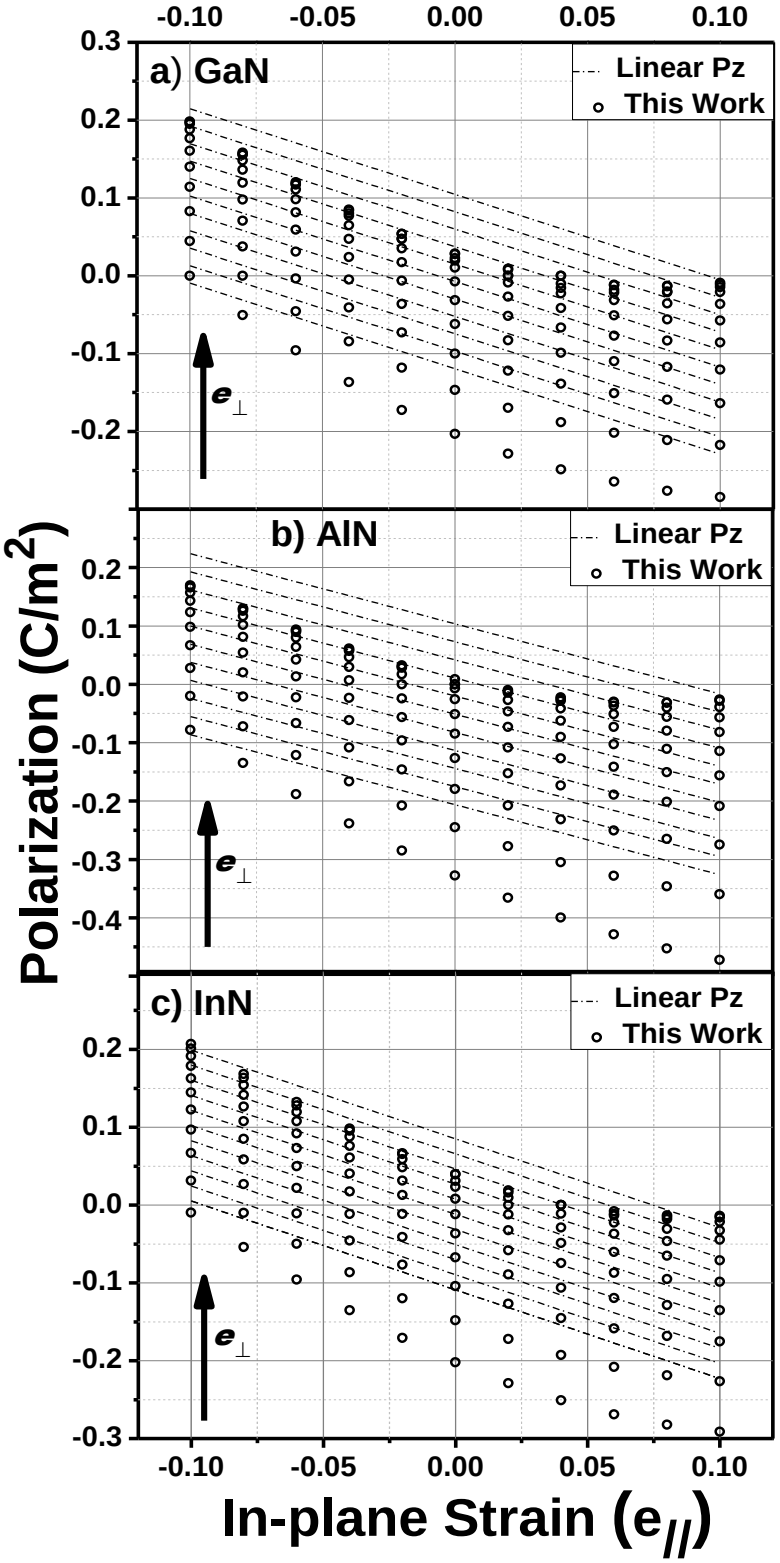

Figure 3.2.5-1: Comparison of the total polarization as a function of perpendicular and parallel strain calculated in this work (circles) and that calculated using the linear model with parameters from Ref [47] (dashed lines). The perpendicular strain varies from -0.1 to 0.1 in steps of 0.02. . Reproduced from the work of Ref [183].

The first obvious difference between the two models is the reduced values of the P_{sp} which offset the various lines of constant stress along the c-axis. Furthermore our model has second order terms that result in the bowing of the various lines, as expected from a second order model with quadratic dependence.

For parallel strain in the (0001) plane not exceeding ±0.08, and large strain along the c-axis (i.e. perpendicular strain), our model always predicts significantly reduced positive values of total polarization for the tensile case, and greatly increased values for the compressive case, compared to the linear model. As an example, a thin film GaN layer pseudomorphically grown on AlN, GaN would be strained by -3% in the growth plane ($\varepsilon_{//}$) and by +6% along the c-axis ($\varepsilon_{\perp}$) resulting in a linear polarization of +0.095 C/m^2 but a substantially lower second order value of +0.06 C/m^2. This is clearly a large correction and cannot be neglected.

It is worth noting that if one removed the P_{sp} and only considered strain induced PZ polarization, for small strains the results of the two models would always coincide, as expected. With larger strain instead the second order terms become more important and deviations between the two models become more pronounced. It is only when the different values of the P_{sp} term are introduced that one notices that for e.g. large compressive strain in the plane the two models appear to coincide. However this is purely coincidental and has no physical significance. What has significance instead is that our model predicts a much larger negative and a smaller positive range of attainable PZ fields for strain in the range ±10%.

3.2.6. Second Order Piezoelectric coefficients

By fitting our data with a second order polynomial we have also obtained second order PZCs for quadratic terms in the strain containing parallel and perpendicular strain components (but not for those containing shear coefficients); the results are presented in Table V, where the subscripts 311, 333 and 133 refer respectively to a double strain in the plane, perpendicular to the plane and the combination of both parallel and perpendicular strain. The coefficients given in Table V allow us to express the strain dependence of the magnitude of the total PZ polarization in the direction orthogonal to the growth plane as

$$P_{Tot} = P_{sp} + e_{33}\varepsilon_{\perp} + 2e_{31}\varepsilon_{//} + e_{311}\varepsilon_{//}^{\ 2} + e_{333}\varepsilon_{\perp}^{\ 2} + e_{133}\varepsilon_{//}\varepsilon_{\perp} \qquad (75)$$

At present we have not evaluated the second order dependence of the polarization due to shear strain in the growth direction or growth plane, connected to the PZC e_{15}. Such dependence could have a potential impact on nanostructures such as quantum dots, but not on 2-dimensional thin films which are the focus of this work, for which Eq (75) is valid.

3.2.7. Comparison with experimental results on binary materials

To test the validity of our method and the PZCs obtained (listed in Table V) we compared with the experimental values for AlN/GaN superlattices. [189,190,191,192]

For this comparison we have evaluated the field in the AlN and GaN regions (conventionally referred to as the barrier (b) and well region (w) respectively) using the well known superlattice equations.[186]

$$F_z^w = \frac{\left(P_{SP}^b + P_{PZ}^b - P_{SP}^w - P_{PZ}^w\right)}{\epsilon^w + \epsilon^b (L_w/L_b)} \qquad (76)$$

$$F_z^b = -\frac{L_w}{L_b} F_z^w \qquad (77)$$

In Eqs. (76) and (77) the spontaneous and strain induced polarizations (P_{sp} and P_{PZ}) combine to give a resulting field in the z direction of growth. The field F also depends on the dielectric constant of the material (ϵ) and the relative lengths L_w and L_b of the well and barrier material.

For the relative dielectric constant we used values[183] of 10.0, 8.5 and 15.3 for GaN, AlN and InN respectively, while using a linear interpolation between binary values for the alloys. Comparison between our calculated fields (to first and second order) in the well region (GaN) and experimental values for several superlattices differing only in the L_w/L_b ratio is presented in Table VI. We also show the results of the calculations using the widely used parameters of Bernardini and Fiorentini[47] (previous work). For this material combination the second order effect is small, as the GaN region is unstrained for growth on GaN on sapphire.

Hence in this case the field is mainly produced by the difference in P_{sp} which with our parameters is 0.044 C/m^2. Our calculated values are in excellent agreement with all available experimental data, with the exception of one where the agreement is however satisfactory (the case of L_w/L_b = (0.8 ±0.26)/(2.8±0.52)). Furthermore our model appears to produce much closer agreement compared to using the parameters from previous work.[47]

Interestingly another independent theoretical work[193] has attempted to calculate the barrier and well fields in the framework of DFT (in the generalized gradient approximation and also in the self interaction corrected scheme). Their predictions, based on calculating the interface electrostatic potential difference in superlattice structures, appear also consistent with both the experimental data and our calculated values (Table VI). The substantial agreement confirms the correctness of our PZCs for GaN and AlN. In particular it validates the proposed lower values of the P_{sp} term, which is probably the most interesting outcome of our model.

TABLE VI: Experimental and calculated values of the piezoelectric field in various quantum wells comprising binary GaN, AlN and InN combinations. The calculated values in this work have been obtained both to first and second order for comparison. We also calculated (previous work) the corresponding values using the first order parameters of Bernardini and Fiorentini.[47] The last column provides the estimates of the ratio of the well width to the barrier width used in the superlattice equations.[184]

Quantum Well	*Experiment* (MV/cm)	*This work (to II order)* (MV/cm)	*This work (to I order)* (MV/cm)	*Previous work* (MV/cm)	*Lw/Lb*
GaN/AlN	10.2[189]	10.30	10.10	10.65	2.6/100[189]
GaN/AlN	8.0[190]	8.06	7.91	8.43	2.5/6[190]
GaN/AlN	10.0 ±1.0[191]	9.00 ±0.50	8.80±0.50	6.00 ±1.00	(0.8 ±0.26)/ (2.8±0.52) [191]
GaN/AlN	5.04[192] (5.19÷4.76 $_{th}$)[193]	5.06	4.95	4.76	2.3/1.9[192]
GaN/AlN	6.07[192] (6.09 $_{th}$)[193]	6.07	5.98	6.55	1.4/1.9[192]
InN/GaN	9.25 $_{th\ (InN)}$[194] 8.13 $_{th\ (GaN)}$[194]	9.62 8.24	8.29 7.10	6.93 5.90	4.7/6[194]
InN/GaN	5.21 $_{th\ (InN)}$[194] 11.17 $_{th\ (GaN)}$[194]	6.61 12.2	6.10 9.79	5.85. 7.89	7/4[194]
InN/GaN	3.99 $_{th\ (InN)}$[194] 8.52$_{th\ (GaN)}$[194]	7.11 11.51	6.50 10.05	5.70 7.33	9.3/6[194]
InN/GaN	6.32$_{th\ (InN)}$ [194] 6.84$_{th\ (GaN)}$[194]	9.32 8.70	8.13 7.57	7.2 5.84	7/8[194]

We have also attempted a similar comparison with superlattice structures comprising InN/GaN layers. Unfortunately we could not find any experimental data to verify our predictions. However theoretical values[194] have been calculated with the same method used by Cui *et al.*[193] The calculated values for the 3 methods discussed are listed in Table VI.

In the Figure 3.2.7-1, we show the comparison of the fields in the well region between our calculated fields (cross) with the experimental fields (squares) along with the linear

model[47] (triangles) with different estimates of the ratio of the lengths of the well and the barrier used in the superlattice equations.[184]

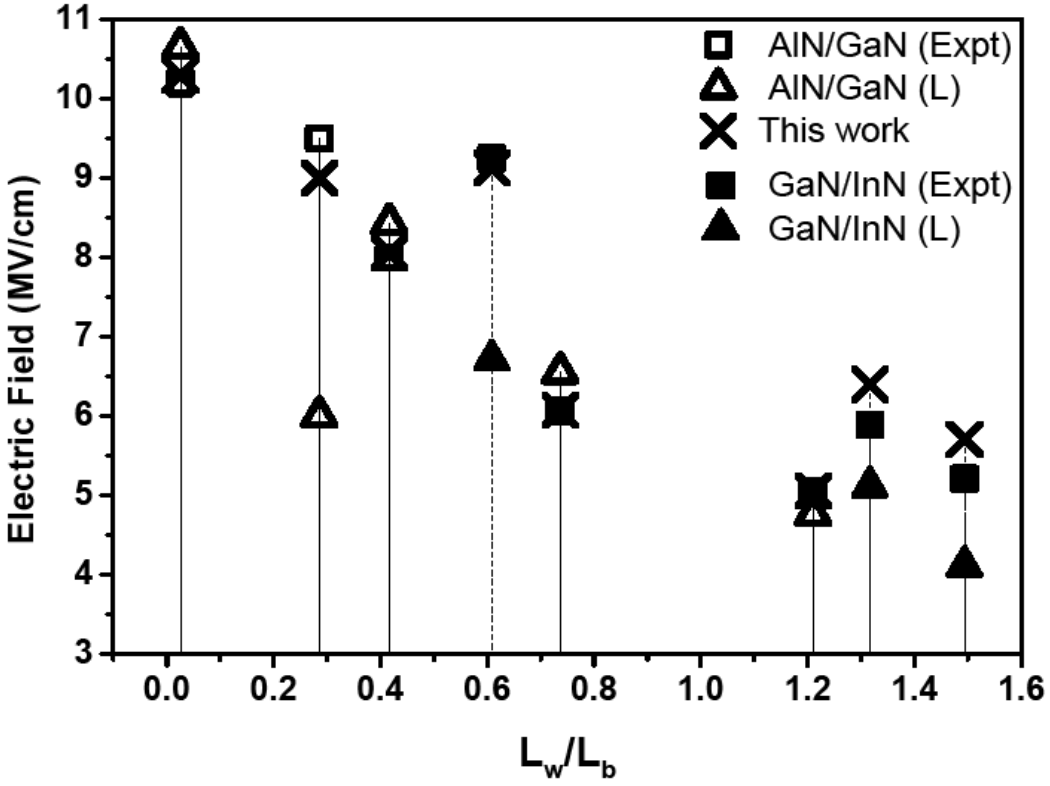

Figure 3.2.7-1: Comparison of the fields in the well region between our calculated fields (cross) with the experimental fields (squares) along with the linear model (triangles) with different estimates of the ratio of the lengths of the well and the barrier used in the superlattice equations.[186] The linear model parameters are taken from Ref.[47]. We compared the field in GaN/AlN (hollow symbols) and InN/GaN (solid symbols) QWs. Reproduced from this work of Ref [195]

The difference between the values of P_{sp} for InN and GaN is only 0.005 C/m^2 and hence this case is a stronger test for the strain induced polarization. It is difficult to make conclusions based on the obtained data, as our model does not always agree with that of Shieh *et al.*[194] In fact the two models seem to either agree for the barrier or the well values, but not for both. It is possible that the structures used in the calculations differ by some aspect, but we cannot draw any conclusions here other than again the linear model using parameters from Bernardini and Fiorentini[47] leads to substantial differences from our calculated values of the field.

3.2.8. Comparison with experimental results on alloys

Given that a significant amount of experimental data for AlGaN/GaN and InGaN/GaN quantum wells (QWs) exists the validity of our model can be further tested. A complication of treating alloys is that a significant parabolic dependence in the composition for all PZCs is present.[196] To test our parameters quantitatively we have therefore introduced a parabolic alloy dependence in all our coefficients, including the second order ones. The procedure we used was to apply to our parameters the same percentage deviation of the $Al_{0.5}Ga_{0.5}N$ and $In_{0.5}Ga_{0.5}N$ from the linearly interpolated values given in Ambacher *et al*[196] for the classic model of Bernardini and Fiorentini.[47] Then we could easily fit a parabolic dependence in essence equivalent to that given in Ambacher *et al*.[196]

Table VII: Experimental and calculated values of the piezoelectric field in various quantum wells comprising AlGaN/GaN and InGaN/GaN alloys. Experimental values for the GaN/InGaN structures were digitally extracted from Fig. 3 of Ref [53]. The calculated values have been obtained including the first and the second order parameters from this work and with the parameters from Bernardini and Fiorentini[47] (previous work), in both cases including the parabolic alloy dependence.[196] In brackets, for comparison, we also show the values obtained including a simple linear interpolation of the piezoelectric parameters. The last column contains the values of the ratio of the well width to the barrier width used in the superlattice equations.[184]

Quantum Well	*Experiment* (MV/cm)	*This work (to II order)* (MV/cm)	*This work (to I order)* (MV/cm)	*Previous work* (MV/cm)	*Lw/Lb*
$Al_{0.17}Ga_{0.83}N$/GaN	0.76[184]	0.760 (1.010)	0.775	1.205 (1.730)	3/50[184]
$Al_{0.65}Ga_{0.35}N$/GaN	2.00[185]	2.090 (2.350)	2.130	2.170 (2.590)	6/3[185]
GaN/$In_{0.06}Ga_{0.94}N$	0.61[53]	0.606 (0.610)	0.594	0.544 (0.530)	3/3
GaN/$In_{0.09}Ga_{0.91}N$	1.00[53]	0.997 (0.980)	0.980	0.766 (0.756)	3/3
GaN/$In_{0.11}Ga_{0.89}N$	1.33[197]	1.325 (1.310)	1.290	1.210 (1.180)	3/3[197]
GaN/$In_{0.12}Ga_{0.88}N$	1.60	1.603 (1.610)	1.575	1.500 (1.450)	3/6
GaN/$In_{0.22}Ga_{0.78}N$	3.09	3.097 (3.120)	3.000	3.132 (3.231)	3/8

Using the corresponding parameters that define the quadratic dependence on alloy composition (given in Table VIII) we have then compared directly with the values of the PZ field in the QW region reported for a variety of QW sizes and compositions for both AlGaN/GaN[184,185] and InGaN/GaN[197] structures in Table VII. It is also worth noting that the reported values of the PZ field in QWs are not direct measurements but rather a value derived from electro-optical characterization of confined levels. Again our comparison is based on calculating the PZ fields in the QW region using Eqs (76) and (77).

TABLE VIII: Quadratic dependence on alloy composition for ternary nitride alloys ($Al_xGa_{1-x}N$, $In_xGa_{1-x}N$). The parameters are for the equation: $Y=Ax^2 + Bx + C$

System	*Y*	*A*	*B*	*C*
$Al_xGa_{1-x}N$	P_{sp}	-0.025	-0.019	-0.007
	e_{31}	0.064	-0.114	-0.550
	e_{33}	0.141	0.279	1.050
	e_{311}	0.674	-1.000	6.185
	e_{333}	1.055	-3.715	-8.090
	e_{133}	0.340	2.650	1.543
$In_xGa_{1-x}N$	P_{sp}	-0.001	-0.005	-0.007
	e_{31}	-0.368	0.368	-0.550
	e_{33}	0.119	-0.099	1.050
	e_{311}	0.635	-1.669	6.185
	e_{333}	1.182	0.228	-8.090
	e_{133}	0.226	-0.489	1.543

A comparison between experimental values of the PZ field in different quantum wells, the predictions obtained with the parameters from Bernardini and Fiorentini[47] and those obtained with the second order parameters of this work, with and without the parabolic dependence on the alloy composition, are presented in Table VII. It is obvious that the parabolic dependence on alloy composition is essential in obtaining PZ fields in the range

of values of experiment, but for all structures there is a substantial improved agreement between our model compared to the widely used one of Bernardini and Fiorentini.[47]

Just like for the binary materials, the AlGaN/GaN structures are more sensitive to difference in spontaneous polarization, while in the InGaN/GaN structures the strain induced polarization and hence the second order coefficients play a more important role. This is also confirmed by the fact that the difference between first and second order tends to increase as the In content is increased, a consequence of sharply increasing strain.

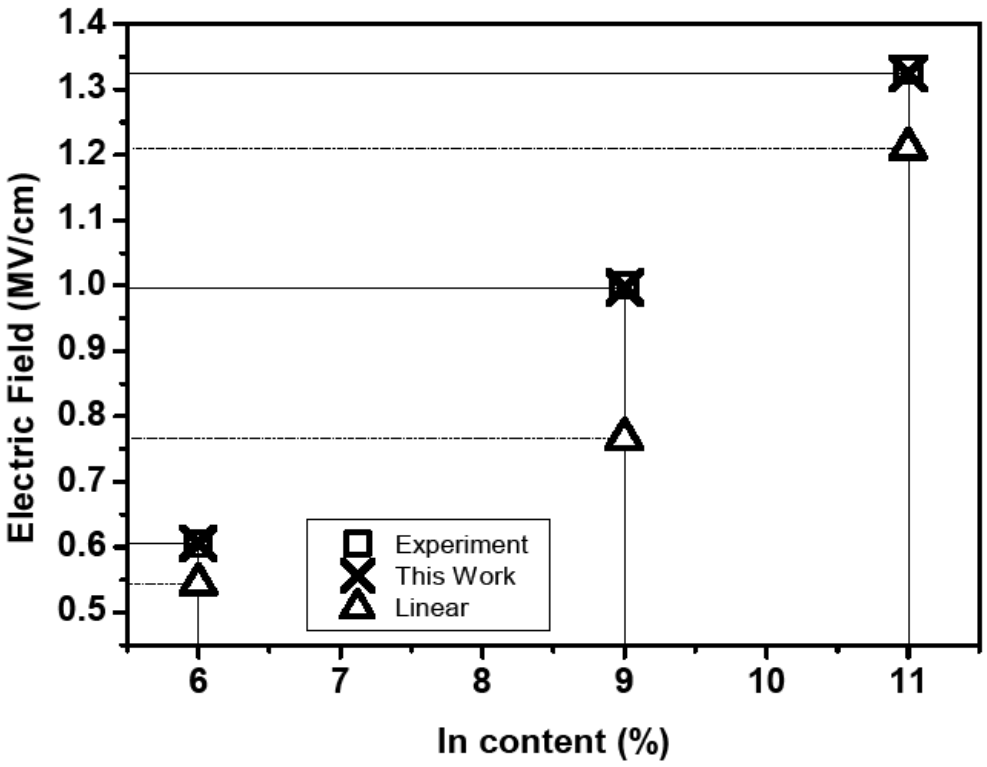

Figure 3.2.8-1: Comparison of the calculated field values (cross) of InGaN/GaN QWs in the well region on different alloy composition and $L_w = L_b$, with the experimentally reported values (squares) and the estimates with the parameters of the linear model (triangles).[47] Reproduced from the work of Ref [195]

In Figure 3.2.8-1, we have compared the experimental values[53,184] of the PZ field in InGaN/GaN QWs, having different alloy composition while the length of the well and barrier were taken as equal, with those obtained from this work with second order

parameters and the estimates with the parameters of the linear model.[47] For all the structures having various alloy composition, we have found a much better agreement using our model with the experimental work compared to the linear model.[47] The agreement between the QW field in the well region and the experimental values strongly favours the validation of our PZCs for InN in real nanostructures.

3.2.9. Matching spontaneous polarization in nitride alloys

As an interesting case we will now discuss the values of the P_{sp} in the ternary alloys AlGaN and InGaN. In Fig. 3.2.9-1 we compare the values of P_{sp} for the $Al_xGa_{1-x}N$ (squares) and $In_xGa_{1-x}N$ (circles) alloys as a function of the molar fraction, as evaluated in

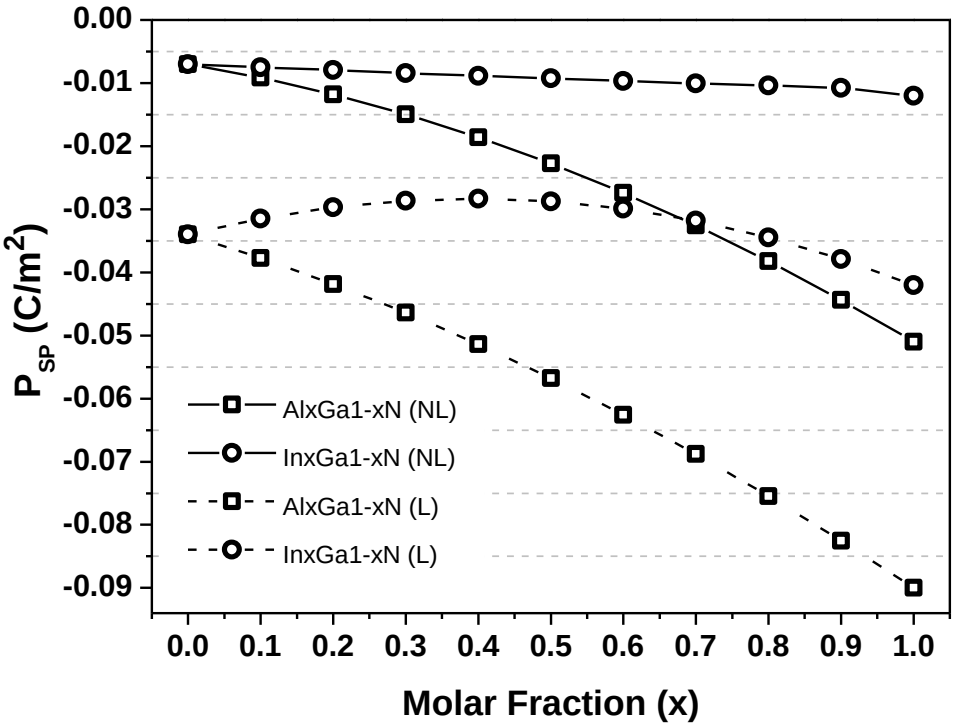

Figure 3.2.9-1: Comparison of the spontaneous polarization (P_{sp}) for the $Al_xGa_{1-x}N$ (squares) and $In_xGa_{1-x}N$ (circles) alloys as a function of the molar fraction x, calculated in this work (solid lines-non-linear model (NL)) and those calculated using the linear model with parameters from Ref [196] (dashed lines-linear model (L)). The quadratic dependence in the molar fraction, with parameters from Table IV was used to evaluate the data within the solid lines. Reproduced from the work of Ref [183].

this work (solid lines) and as calculated using the linear model with parameters from

Ref [196] (dashed lines).

The quadratic dependence in the molar fraction for the P_{sp} values in this work was introduced using the parameters from Table VIII. Firstly we notice that the model used for the dashed lines predicts that only In rich InGaN with In content of at least 80% would exhibit the same spontaneous polarization as an AlGaN alloy. For this to happen, the Al content would have to be low, up to about 20%.

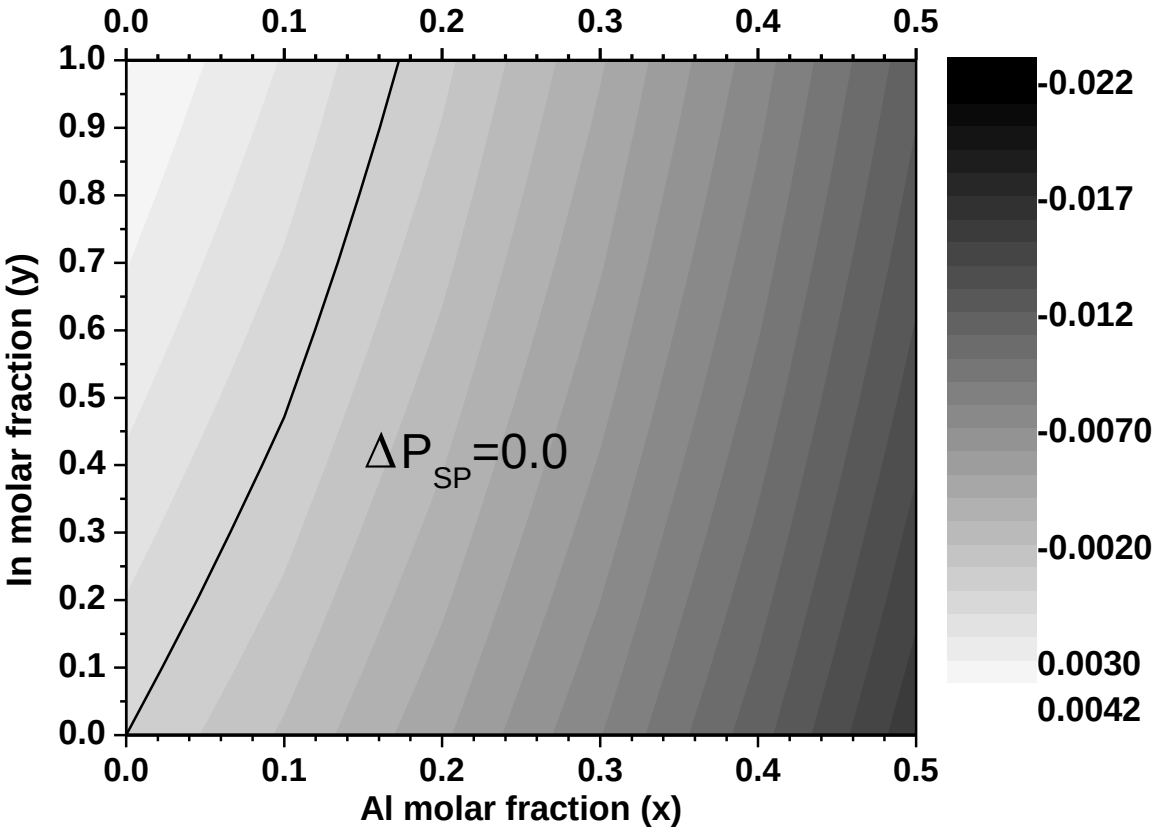

Figure 3.2.9-2: Mapping of the difference in the spontaneous polarization (P_{sp}) between $Al_xGa_{1-x}N$ and $In_yGa_{1-y}N$ for $x \leq 0.5$ and $0<y<1$. The solid line illustrates the region where such difference vanishes ($0<x<0.17$). Reproduced from the work of Ref [183].

The data presented in the solid lines, which uses our reduced values of the P_{sp} term, shows that instead this equality can be easily achieved at low In and Al contents. In Fig. 3.2.9-2 we show the mapping of the difference in P_{sp} between $Al_xGa_{1-x}N$ and $In_yGa_{1-y}N$ for $x \leq 0.5$ and y between 0 and 1.

A line exists where such difference vanishes for values of x between 0 and 17%. Because of the inherent difficulty of growing In rich InGaN alloys the fact that it is possible to find vanishing P_{sp} differences for low enough In and Al fractions, means the possibility of designing layers where, according to Eqs. (76) and (77) the PZ field is entirely due to the strain induced polarization and is reduced compared to having materials with a difference in the P_{sp} terms.

In conclusion, we have calculated both the P_{sp} and the first and second order PZCs, in the framework of ab initio DFT and DFPT in conjunction with the semi empirical formulation of Harrison.[57]

Compared with previous calculations, which used only the linear theory of piezoelectricity and large values of the P_{sp}, our model, where a significant role of second order piezoelectricity and much smaller values of the P_{sp} are proposed, provides a much better agreement with available experimental data of the PZ field in the quantum well regions for various III-N materials and their alloys.

Furthermore we showed that our model predicts that by choosing particular values of the molar fractions in AlGaN and InGaN alloys it is possible to match the spontaneous polarization terms and reduce the total piezoelectric field to the strain induced one alone. This could have applications in the design of optoelectronic devices.

3.3. ZnO Semiconductors

As we already discussed in the first chapter, the recent discovery of the applicability of ZnO nanowires as mechanical energy sensors has originated a new field, Piezotronics. The proposition of combining piezoelectric and electronic properties using semiconductor materials has great potential for the realization of self-powering devices, nanogenerators and flexible electronics.

In II-VI semiconductors, like the III-N semicondutors, strain with a component along the polar axis of the crystal leads to the generation of electrical dipoles. In a wurtzite crystal such dipoles are linked to the diagonal strain tensor components and the resulting piezoelectric field is along the polar axis [0001]. Though the piezoelectric field in semiconductors has for a long time been treated as linear effect in the strain, the influence of non-linear components has already been discussed in zincblende III-V and wurtzite III-N semiconductors earlier in the chapter 3.

In this section, we will discuss the recent work on the quadratic piezoelectric coefficients (PZCs) of ZnO[198] and demonstrate that the magnitude of the coefficients is such that cannot be omitted in any calculation of the polarization field.

Similar to the behaviour of the polarization in III-N semiconductors, we observed the polarization to be non-linear as well in ZnO and the total polarization equation is identical to (75) with all the values in Table IX.

Note that in our model smaller values of the spontaneous polarization are predicted compared to previous calculations[47,199]. This is an expected result and the reason behind it is explained in detail in our previous work on wurtzite III-N semiconductors[183].

Table IX. Calculated and measured physical parameters for ZnO used in the calculations. Comparisons between our calculated values and other calculated and/or experimental ones are given in brackets.

Parameters	
a (Å)	3.18 $(3.25^{47})_{th}$
c (Å)	5.16 $(5.207^{47})_{th}$
u	0.375 $(0.375^{47})_{th}$
Z*	2.164 $(2.11^{47})_{th}$
α_p	0.67 $(0.69^{200})_{th}$
Z_H*	0.23
C_{33} (GPa)	176^{201}
C_{13} (GPa)	84^{201}
P_{sp}(C/m^2)	-0.01 $(-0.057^{47}, -0.047^{199})_{th.}$
e_{33} (C/m^2)	1.15$(1.22 \pm 0.04,^{202} 0.96^{54})_{exp}$
e_{31} (C/m^2)	-0.61$(-0.51 \pm 0.04,^{202} -0.62^{54})_{exp}$
e_{311} (C/m^2)	3.98
e_{333} (C/m^2)	-5.59
e_{313} (C/m^2)	1.21

The dependence of the total polarization on strain in the range -0.08 to + 0.08 according to the classic linear model (LM) and our non-linear (quadratic) model (NLM) is shown in Figure 3.3.1. The main feature is that the NLM appear to predict compared to LM, more positive values of the polarization. This is part a result of the smaller values of the spontaneous polarization but also due to non-linear effects which manifest through the coefficients e_{333} and e_{133} when the strain is sufficiently large.

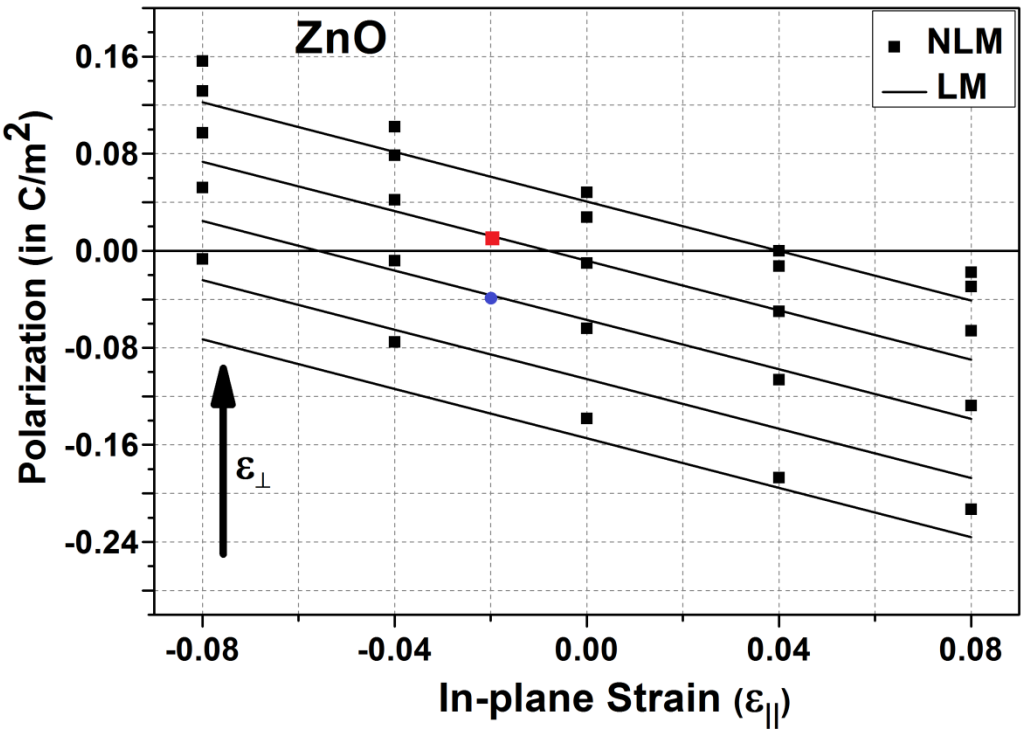

Figure 3.3-1: Dependence of the total polarization (C/m^2) on strain in the range -0.08 to + 0.08 according to the classic linear model (LM) and our non-linear (quadratic) model (NLM). The red square and blue dot resemble the NLM and LM prediction at -2% In-plane strain. Reproduced from Ref [198].

We also notice that in same cases the LM and NLM predict opposite signs for the polarization, e.g. around 2% compressive parallel strain and no perpendicular strain gives a value of the total polarization of -0.04 C/m^2 or +0.01 C/m^2 using the LM (in blue dot) or NLM (red square) respectively.

Thus, we have estimated the linear and quadratic piezoelectric coefficients of ZnO wurtzite crystals and the magnitude of the quadratic terms is significant and necessitates inclusion even in the limit of small strain.

3.4. Applications and Devices

This section explores the effect of non-linear piezoelectricity in applications and devices and its potential exploitation in III-V, III-N and II-VI semiconductors and nanostructures. We will discuss about the influence in the QW based devices, then progressing to the NWs and finally QD properties will be explored in the coming sections.

3.4.1. Quantum well based LED optical properties

The performance of the LED based devices has long been affected and limited by the much published issue of efficiency droop.[203,204] One of the major factors limiting the light output power is the presence of in-built polarization fields that originate from the wurtzite crystal structure of III-N semiconductors.[205,206,207,208] Such fields can be high enough to localize carriers at the interfaces and create, through Coulomb repulsion, energy barriers that hinder carrier transportation. With the aim of circumventing such issues much work has recently been concentrated on producing devices on non-polar and semi-polar crystal orientations.[209,210,211,212] However, the output powers at high injection current of these devices currently do not outperform the best devices grown on (0001) planes (c-planes).[208,213,214]We calculated the field dependence of blue and green InGaN-based LEDs on hydrostatic pressure.

The device performance would be strongly enhanced if such fields were sizeably reduced in InGaN c-plane grown structures which are currently grown on either sapphire or silicon substrates. We have recently shown[215] that there is a correlation between the value of the internal field and the reduction of the efficiency in c-plane GaN-based LED devices. This was revealed using optical efficiency measurements as a function of applied hydrostatic pressure of commercially-available blue and green polar multi-quantum well (MQW) LEDs with indium content of 14% and 26%, respectively, well widths of 3nm in

both LED types, and barrier widths of 13 nm in blue and 16nm in green LEDs. Applying pressure from 0 to 1GPa led to a reduction of ~4% in the light output power for both LEDs at an operating current of 260mA. In order to correlate this effect with the value of the polarization field we estimated, the piezoelectric field in the quantum well region have been calculated using both the linear piezoelectricity (LP) model of Bernardini and Fiorentini[47] and the more accurate recently reported non-linear[187,188,196,216,217]model (NLP) of Pal *et al*.[183]

We reported[215] that the LP model predicts a reduction of the field of around 2%, which should result in increased optical efficiency, which is the opposite effect to the experimental observations. In contrast, the NLP model predicts an increase of 4% in the strength of the piezoelectric field which is consistent with our experimental observations of a decrease in the optical efficiency with increasing hydrostatic pressure.

Whilst we observe an inverse proportionality and linear scaling between the efficiency and the value of the piezoelectric field in the active region as calculated using the NLP model, the radiative recombination rate is expected to show a stronger (quadratic rather than linear) increase with reducing internal polarization field strength due to the enhancement of the optical matrix element in Fermi's golden rule. This discrepancy can be attributed to the fact that the experimental output power is increased by the radiative recombination rate but decreased due to non-radiative processes,[218] resulting, in this case, in an approximately linear rather than quadratic dependence on the applied pressure.

We now investigate the dependence of the internal field on applied tetragonal pressure i.e. a combination of tensile (in the growth plane) and compressive (along the c-axis) strain, instead of hydrostatic pressure, which is equal in all directions, used in our experiments.

A very recent work by Suski *et al* [219] showed that in order to correctly reproduce optical experimental data for nitride based LED structures, we need to implement NLE. The pressure dependence of the PL peak energy has been evaluated experimentally and compared with k·p calculations involving both our non-linear model of piezoelectricity as well as the classic linear model. The impact of NLE has been tested and it has been observed that NLE provides much improved estimates. The interesting aspect of the results suggests that with linear model of piezoelectricity the theoretical predictions completely disagree with the experimental observations and follow the negative slope, even with implementation of NLE. While, the predicted values using our non-linear model shows the correct positive slope and implementation of NLE makes the theoretical outcomes closer to the experimental data. In Figure 3.4.1-1, triangles represent the linear PZ model with LE and NLE while circles and squares are the non-linear PZ model with LE and NLE respectively. The experimental results are marked in the blue hatched rectangle. The authors also compared to another model of piezoelectricity and termed it as nonlinear piezoelectricity due to dependence of the first-order piezoelectric constants on deviatoric strain, but referred to our more accurate and complete model as second order piezoelectricity to differentiate the two models.

This clearly suggests the importance of the non-linear PZ model and also the effect of the NLE in the theoretical calculations for much precise outcome.

This prompted the inclusion of the effects of non-linear elasticity (NLE)[103] in the calculations, performed in a similar framework as previously used.[183]

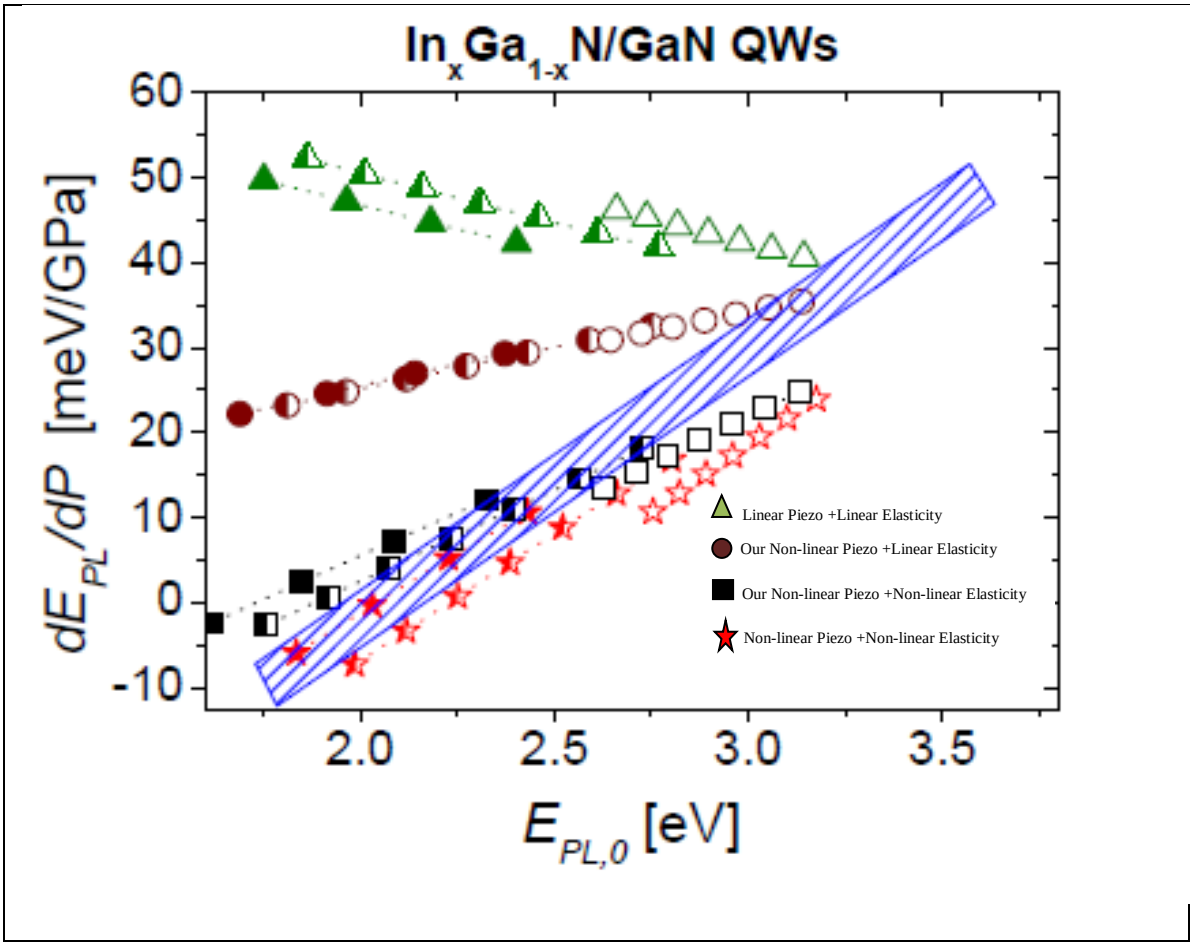

Figure 3.4.1-1: Comparison between the experimentally determined dependence of dE_{PL}/dP vs $E_{PL,0}$ and the results of the k.p calculations performed for $In_xGa_{1-x}N$/GaN QWs with x= 0.1 (empty symbols), 0.2 (half-filled symbols), and 0.3 (solid symbols). Triangles, circles, squares, and stars correspondto the theoretical results obtained using (i) linear piezoelectricity and linear elasticity, (ii) second-order piezoelectricity and linear elasticity, (iii) second-order piezoelectricity and nonlinear elasticity, (iv) nonlinear piezoelectricity (due to dependence of the first-order piezoelectric constants on deviatoric strain) and nonlinear elasticity, respectively. The hatched rectangle represents the experimental results. (Reproduced from T. Suski *et al.*[219])

We studied a typical active region of an LED structure containing a series of $In_xGa_{1-x}N$/GaN multi quantum wells grown on a GaN layer, assuming that no residual strain from the substrate is present. For blue and green emission we used indium compositions of x=0.14 and x=0.26, respectively, and a typical structure with a 3nm/3nm well to barrier ratio. The build-in field in the quantum well region can be estimated from the super-lattice equations Eq. (76) and Eq.(77) from Chapter 3.2.7.

The relation between parallel and perpendicular strain components is evaluated using the following equations[103]:

$$C_{\alpha\beta}(P) = \sum_{n=1}^{4} C_{\alpha\beta,i} P^n \quad (78)$$

$$\varepsilon_{\perp} = -\frac{2C_{13}(P)}{C_{33}(P)} \varepsilon_{||} \quad (79)$$

where P is the internal pressure, $C_{\alpha\beta,i}$ are the NLE parameters and $C_{\alpha\beta}(P)$ are the final pressure dependent elastic parameters, taken from Lepkowski.[103]

Using the relationship for the pressure-induced strain from Thomas *et al.*,[220] Figure 3.4.1-2 shows the relative change in compressive strain with hydrostatic pressure.

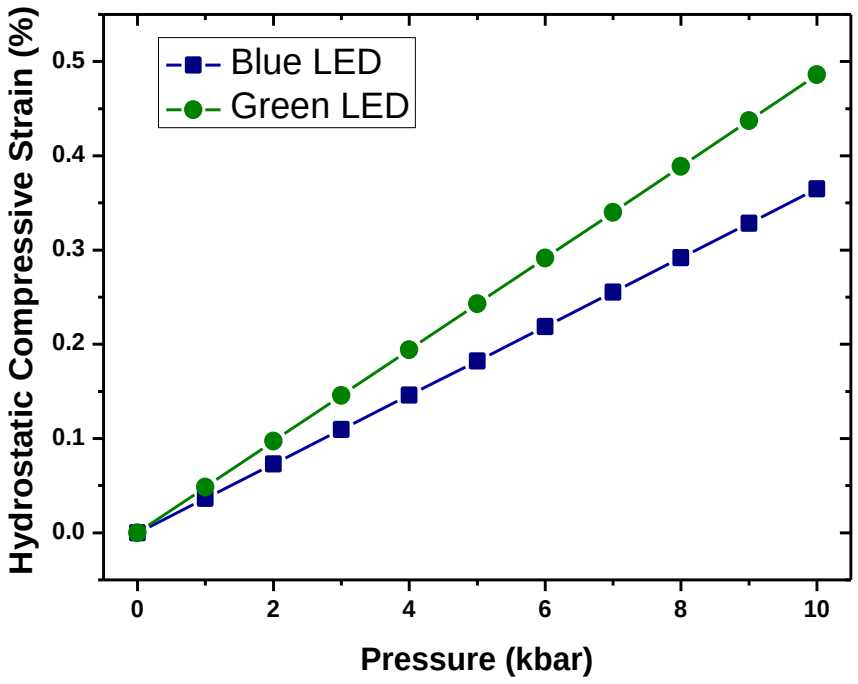

Figure 3.4.1-2: The proportional change of the hydrostatic compressive strain within the LEDs as a function of pressure.[215]

In Figure 3.4.1-3 we show the dependence of the total polarization (spontaneous plus strain induced polarization) in the well and barrier region as a function of tensile strain (evaluated from NLE) in the plane orthogonal to the c-axis for the blue (a) and the green (b) LED structures. Note that vanishing tensile stress in this plot equates to the situation encountered in devices when the entire structure is lattice matched in the c-plane to the

GaN lattice parameter. Essentially the tensile strain on the abscissa of the graph needs to be interpreted as an additional tensile strain but not as the overall strain.

Therefore the polarization results from both the parallel strain due to the lattice mismatch between the bulk values of the InGaN and GaN lattice parameters and an additional (hypothetical) tensile strain. However we have also taken into account any additional compressive strain in the c-axis originating from the additional tensile strain in the c-plane.

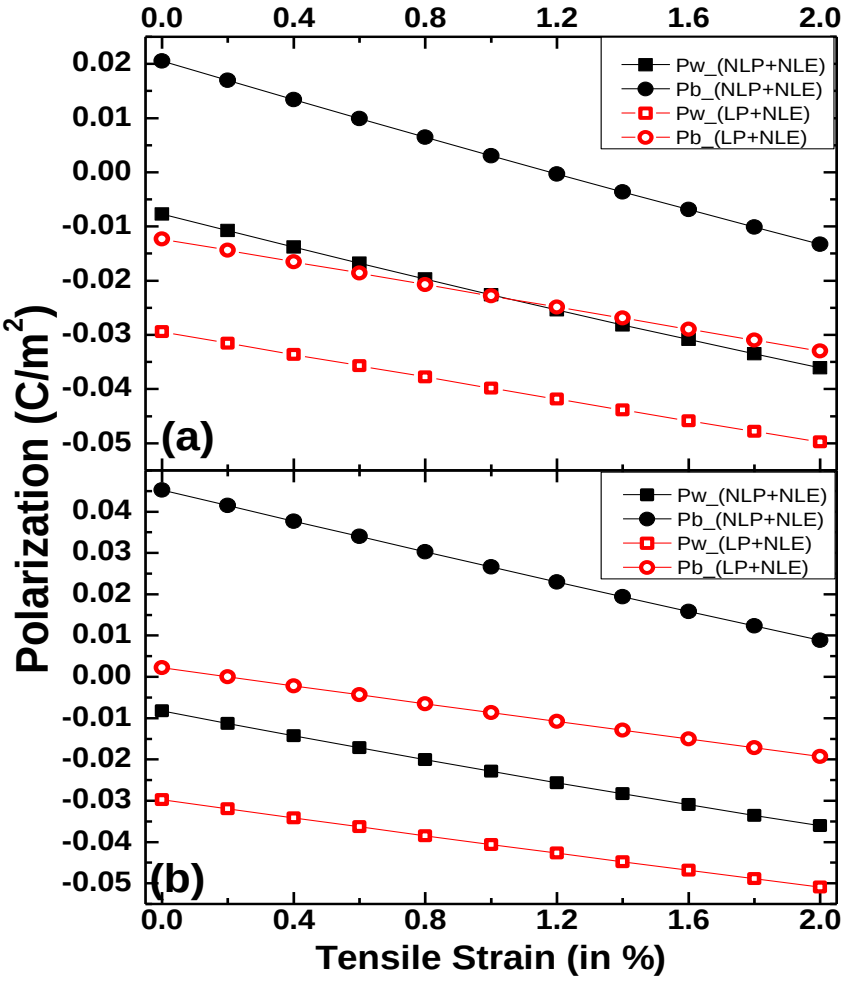

Figure 3.4.1-3: Dependence of the total polarization (spontaneous plus strain induced polarization) in the well and barrier region as a function of tensile strain (evaluated from NLE) in the c-plane for both the blue (a) and the green (b) LED structures. Reproduced from the work in Ref [215]

Though both well and barrier polarizations, for both blue and green LED structures, show a similar slope as a function of additional tensile strain, the magnitude of the polarizations, when calculated using LP and NLP parameters, are substantially different. This is primarily a result of the much smaller spontaneous polarization terms of NLP compared to LP. In both cases of blue and green LEDs the polarization calculated with NLP is always stronger (more positive) than that calculated with LP.

Significant differences between the two models arise when the polarizations shown in Figure 3.2.1-3 are used with the superlattice equation (Eq. (76) and Eq. (77)) from Chapter 3.2.7) in order to calculate the fields in the barrier and well regions. In Figure 3.2.1-4 we show the dependence of the piezoelectric field in the MQW region as a function of the tensile strain in the c-plane as used in Figure 3.2.1-1 for both the blue and the green LED structures.

For comparison we show the results obtained using the LP model, the NLP model and the NLP model with the addition of NLE. Unlike LP, the NLP model combined with NLE leads to a pronounced reduction of the piezoelectric field as a function of increasing tensile strain in the well region.

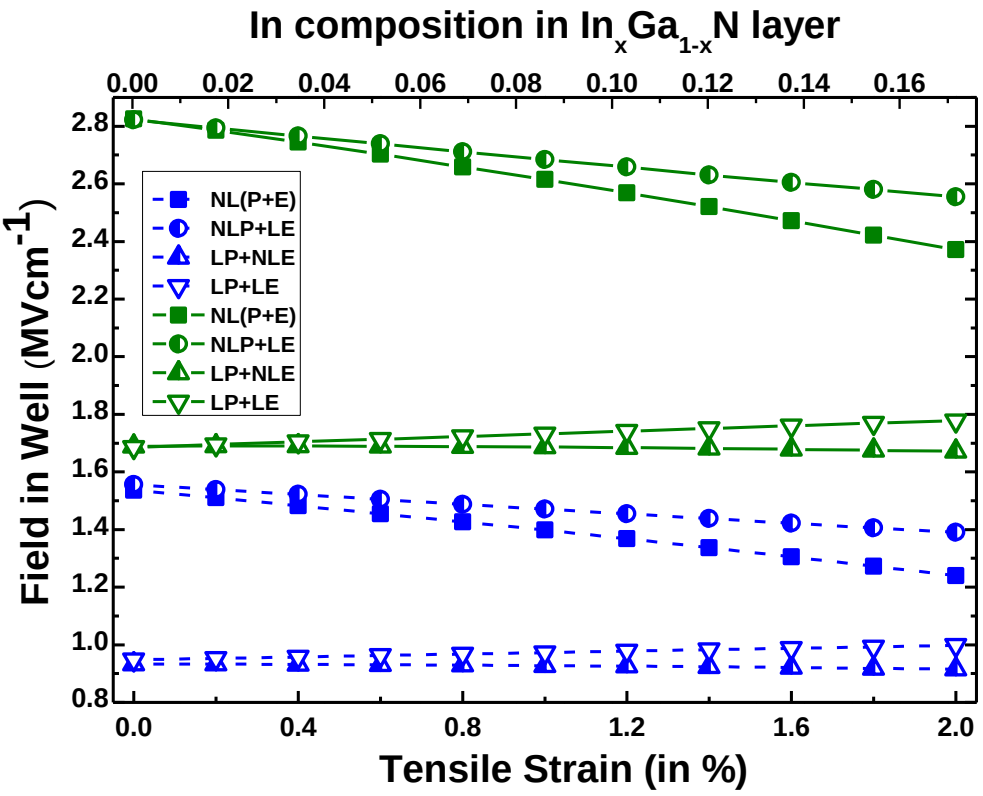

Figure 3.4.1-4: Dependence of the piezoelectric field in the well region as a function of tensile strain in the c plane, for both the blue and the green LED structures. We compare the calculations using the LP model, the NLP model and the NLP model with the addition of NLE. Reproduced from the work of Ref [221]

For example, a 1% additional tensile strain would result in a change of the piezoelectric field from 1.54 MVcm^{-1} to 1.40 MVcm^{-1} in the blue LED and from 2.825 MVcm^{-1} to 2.615 MVcm^{-1} in the green LED. Such reduction is also larger compared with the case of using the NLP model with LE. On the top axis of Figure 3.4.1-4 we show the In composition of a relaxed $In_xGa_{1-x}N$ intermediate layer (see Figure 3.4.1-5) between the substrate and LED structure which would generate the corresponding additional tensile strain as shown on the bottom axis. Thus if the MQW region was grown on a relaxed $In_{0.09}Ga_{0.91}N$ layer then an additional tensile strain of around 1% in the growth plane would be present throughout the active region of the device.

This data suggests that one effective way to reduce the detrimental effects of the presence of internal piezoelectric fields inside the active region of c-plane of InGaN LED devices

is to use an InGaN metamorphic layer (Figure 3.4.1-5). The compositions proposed of up to 9% In is in the achievable range for crystal growth.[221] Metamorphic layers have been demonstrated[222] to start strained and lattice matched to the substrate while subsequently relaxing towards their bulk lattice parameter, providing a virtual substrate on which the new layers then can be grown. Partial relaxation after about 10-20nm seems to favour the growth of subsequent layers lattice matched with the new virtual substrate. In this way, with the metamorphic layer inserted before the MQW region, the subsequently deposited material would feel a strain reduction in the InGaN layers and a strain increase in the GaN barriers.

Inevitably, such a layer could provide an additional source of dislocations (though it could also stop threading dislocations propagating from the substrate), it would also substantially reduce the piezoelectric field in the active region.

Additionally, the large conduction band discontinuity between InGaN and GaN can affect mobility of the n-type carriers,[223] but since the problem in bipolar devices such as LEDs is with hole transport, it should not significantly affect device performance.

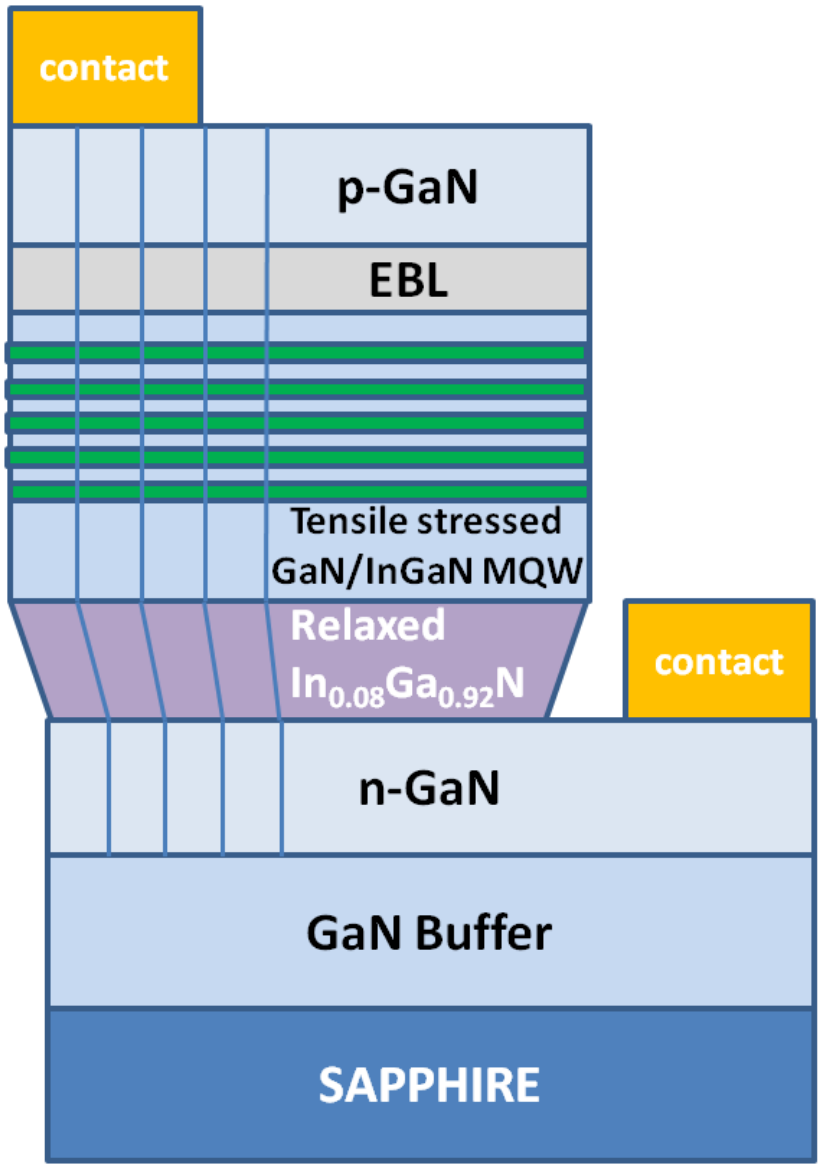

Figure 3.4.1-5: Proposed c-plane InGaN LED device structure using a metamorphic layer before the MQW region which is grown on the top of n-type GaN layer. Reproduced from the work of Ref [221]

Since a 1% additional tensile strain reduces the internal field by ~9% and ~8% for the blue and green LEDs, respectively, and since we have showed how a field reduction can be linked to a comparable increase in optical efficiency,[215] we believe a metamorphic intermediate InGaN layer could produce significant benefits for improved device performance. Having all the recent advances and increased level of control achieved in crystal synthesis and MOCVD growth of nitride compounds, the inclusion of a relaxed layer of InGaN with a modest In concentration is simply a matter of experimentally finding the correct growth conditions. Furthermore it should also make the deposition of

the MQW region easier as it would reduce the lattice mismatch between the well and barrier regions. Such an increased tensile strain as in our proposed structure in Figure 3.4.1-5 is likely to vanish in the subsequent layers deposited after the MQW region, due to the typically large thickness. Therefore one can expect that the electronic blocking layer (EBL) and p-doped GaN region could be grown without additional need to significantly alter growth conditions compared to the case where the metamorphic layer was not included.

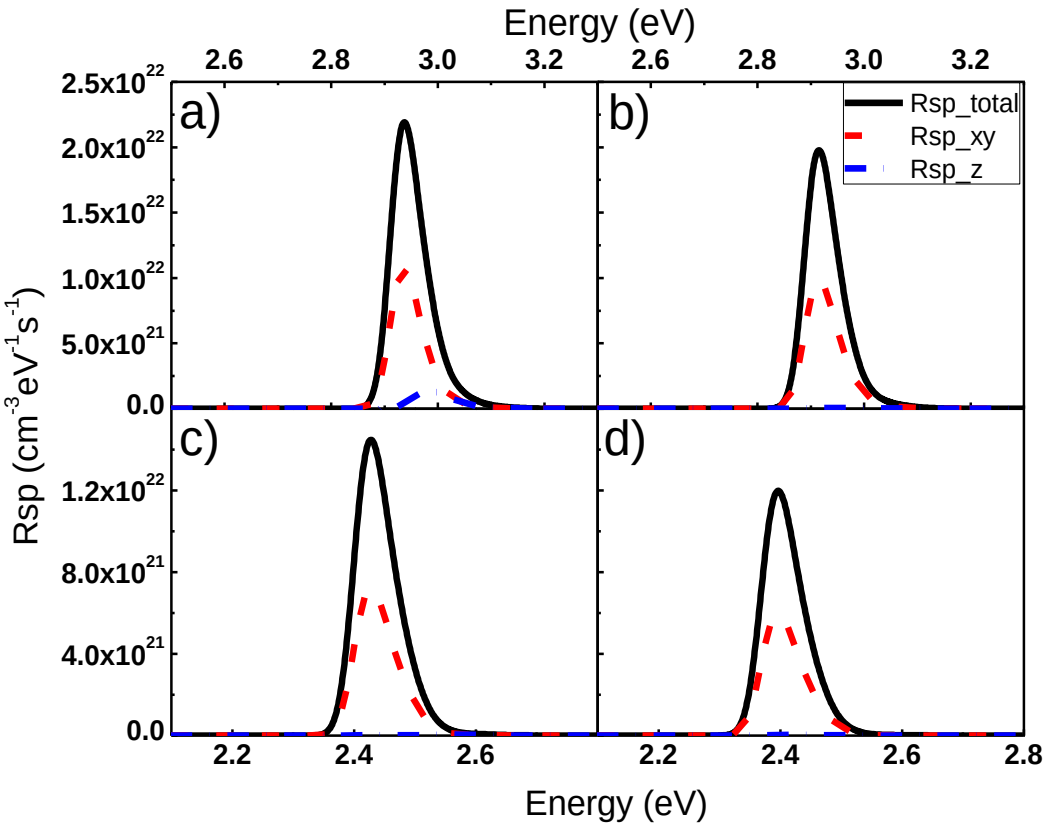

Figure 3.4.1-6: Spontaneous emission spectra at injection carrier density equal to 2.5 x 10^{12} cm^{-3} for both the blue (x=14%) and green (x=26%) LED structures having $In_xGa_{1-x}N$/GaN quantum wells with metamorphic layer (a and c) and the conventional quantum well structure (b and d). Reproduced from the work of Ref [221].

It is also worth mentioning that though direct comparison is difficult, these predictions had to some extent already been made by Shieh *et al*,[194] who by modelling the band offsets and interface polarization of InN/GaN superlattices as a function of strain had

concluded that the strain conditions were an unrecognized degree to which device properties could be potentially controlled.

To further test our proposal we calculated the spontaneous emission spectra for the Green and Blue LED with and without the metamorphic layer. We utilized a self-consistent Poisson and 6 X 6 k·p Schrödinger solver (developed by our collaborator, Prof. Yuh-Renn Wu's research group at National Taiwan University, Taiwan) to solve iteratively until convergence. The k·p method[224] is used for calculating the valence and conduction band levels within the effective mass approximation. We use the polarization-dependent optical matrix elements:

$$\text{x – polarized: } |\langle S|p_x|X\rangle|^2 \left(\left|\langle\psi_l^e|\psi_{m1}^h\rangle\uparrow + \langle\psi_l^e|\psi_{m5}^h\rangle\uparrow\right|^2 + \left|\langle\psi_l^e|\psi_{m2}^h\rangle\downarrow + \langle\psi_l^e|\psi_{m6}^h\rangle\downarrow\right|^2\right)/4$$

$$\text{y – polarized: } \left|\langle S|p_y|Y\rangle\right|^2 \left(\left|\langle\psi_l^e|\psi_{m1}^h\rangle\uparrow - \langle\psi_l^e|\psi_{m5}^h\rangle\uparrow\right|^2 + \left|\langle\psi_l^e|\psi_{m2}^h\rangle\downarrow - \langle\psi_l^e|\psi_{m6}^h\rangle\downarrow\right|^2\right)/4$$

$$\text{z – polarized: } |\langle S|p_z|Z\rangle|^2 \left(\left|\langle\psi_l^e|\psi_{m3}^h\rangle\uparrow + \langle\psi_l^e|\psi_{m4}^h\rangle\downarrow\right|^2\right)/4, \quad (80)$$

in the expression for the spontaneous emission rate[225], which for electron-hole pair recombination in a quantum-confined active region is given by (in Gaussian CGS units):

$$R_{sp} = \int d(\hbar\omega)\frac{4\pi^2 e^2\hbar}{n^2 m_0^2\hbar\omega}\frac{1}{2\pi^2}\sum_{n,m}\int dk \sum_{\sigma,\hat{\varepsilon}}|\hat{\varepsilon}P_{nm}^{\sigma}(k)|^2$$

$$\times\,\rho_{\hat{\varepsilon}}(\hbar\omega)\,\delta(\mathrm{E}_n^e(\mathrm{k}) - \mathrm{E}_m^h(\mathrm{k}) - \hbar\omega) \times [\mathrm{f}^e(\mathrm{E}_n^e(\mathrm{k}))][1 - \mathrm{f}^h(\mathrm{E}_m^h(\mathrm{k})] \quad (81)$$

where $\rho_{\hat{\varepsilon}}$is the (in general) polarization-dependent photon density of states.

In Figure 3.4.1-6 we show the difference in emission strength, by comparison of the spontaneous emission spectra for both the blue (x=14%) and green (x=26%) LED structures having $In_xGa_{1-x}N$/GaN quantum wells with metamorphic layer (Fig 3.4.1-6a and Fig 3.4.1-6c) and the conventional quantum well (Fig 3.4.1-6b and Fig 3.4.1-6d).

At injection carrier density equal to 2.5 x 10^{12} cm^{-3}, the conventional LED structures light emissions is significantly lower than the proposed ones with the metamorphic layer. The results are summarized in Table X.

Table X: Wavefunction overlap, peak emission energy, peak spontaneous emission rate and integrated spontaneous emission for both the blue (x=14%) and green (x=26%) LED structures having $In_xGa_{1-x}N$/GaN quantum wells with and without metamorphic layer

LED Structure	*Overlap*	*Emission Energy (eV)*	*Peak Spontaneous Emission rate Rsp(max) (10^{22} ($cm^{-3}eV^{-1}s^{-1}$))*	*Integral of Spontaneous Emission Rate (Rsp) (10^{21} ($cm^{-3}eV^{-1}s^{-1}$))*
Blue with ML	0.5070	2.94	2.190	1.801
Blue without ML	0.4525	2.92	1.975	1.619
Green with ML	0.3652	2.42	1.447	1.214
Green without ML	0.3329	2.40	1.197	1.003

The results clearly indicate that the addition of tensile strain to the active region is beneficial to the efficiency of LED devices. We also noticed that a similar proposition was experimentally reported by Zhang and Tansu[226], who used InGaN substrates with In composition of 15%. Such substrate would act precisely as the metamorphic layer proposed in this work. Zhang and Tansu[226] reported that the structure grown on InGaN substrate exhibited spontaneous emission rates twice or thrice as large as the conventional structures.

We can now theoretically confirm their result and the interpretation given by Zhang and Tansu[226], who attributed the improved performance to interplay between strain and internal polarization fields. However we need to stress that only the non-linear theory of

piezoelectricity calculates correctly the reduction in the polarization field in the Quantum Well regions that is the origin of the increased spontaneous emission rate.

In conclusion, we have analyzed the strain dependence of the piezoelectric field in the active region of two pseudomorphically strained $In_xGa_{1-x}N$ MQWs with different In content and designed for blue (x=0.14) and green (x=0.26) light emission. A significant reduction of the total internal piezoelectric field as a function of tensile strain is found in both cases, when both non-linear piezoelectricity and non-linear elasticity models are taken into account in the calculations. Since tensile strain could be generated by growing the QW region on a semiconductor layer with a lattice parameter larger than that of GaN, a proposal to use a relaxed InGaN metamorphic layer has been presented. We have evaluated the optical matrix elements and the resulting spontaneous emission rate for the proposed structures and confirmed that, consistent with experimental data in the literature, an increase of the optical emission can be predicted. Since we have previously experimentally showed that the change in value of the internal piezoelectric fields is proportional to the change in optical efficiency, LED devices made using the proposed structures are expected to increase their light output power by up to 10%.

3.4.2. Quantum Nanowire properties

Nanowires (NWs) have been gaining major attraction in nanoscience studies as well as in applications in nanotechnology.[7,8,9,10,11] Over the last decade, the research field of semiconductor NWs has seen exponential growth with much focus on the synthesis, fundamental properties along with the potential applications.

The NWs are 1-dimensional systems having one quantum direction unconfined for electrical conduction, which allows NWs to be used in unique applications requiring electrical conduction rather than tunnelling transport. NWs have high aspect ratio with wire-like structures and typical diameters involved ranges from a few to hundreds of nanometers. A variety of semiconductor systems, including Group II-VIs, III-Vs and Si/Ge, have been exploited to synthesize NWs to date with different and interesting morphologies.[31,32,33]

As a result of the high surface to volume ratio and the size, these wires show significantly different behaviour in optical, thermal, mechanical, magnetic and electrical properties from the bulk material. The NWs provide an exciting framework to apply the "bottom-up" approach (Feynman, 1959)[227] for the design and modelling of nanoscience applications. The exploitation of these unique and novel properties of the NWs have resulted in widespread applications from nanophotonics, piezotronics, thermoelectrics, energy harvesting.[228,229]

III-nitride semiconductors based NWs are getting more explored for prospective applications in LEDs,[25] piezotronics,[27] photovoltaics,[230] lasers,[231,232] high speed/power electronics,[233,234] and other applications.

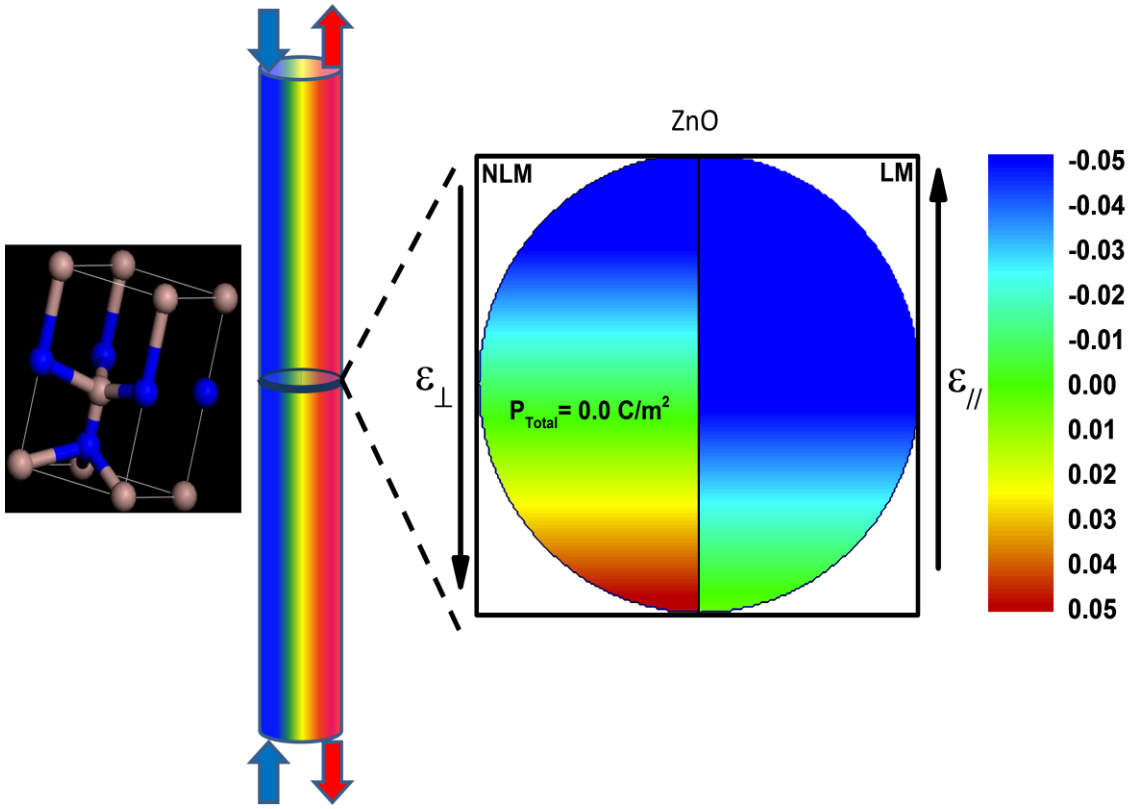

Figure 3.4.2-1: A schematic of the nanowire under strain and the corresponding impact on the cross-section due to piezoelectric polarization.

In our recent work on ZnO semiconductors, we showed calculations of the total polarization in ZnO nanowires and reported that for particular strains originating from an external force, our non-linear model (NLM) of piezoelectricity predicts both positive and negative polarizations in the nanostructure whereas the linear model (LM) only predicts negative values. We have considered Linear Elasticity in calculations for both models. A schematic diagram of a strained nanowire is shown in Figure 3.4.2-1.

A cross section of a ZnO NW under strain is shown in Figure 3.4.2-2, where the perpendicular (parallel) strain $\boldsymbol{\varepsilon}_{\perp}(\boldsymbol{\varepsilon}_{||})$ varies from -2.8% (+2.8%) to +2.8% (-2.8%).

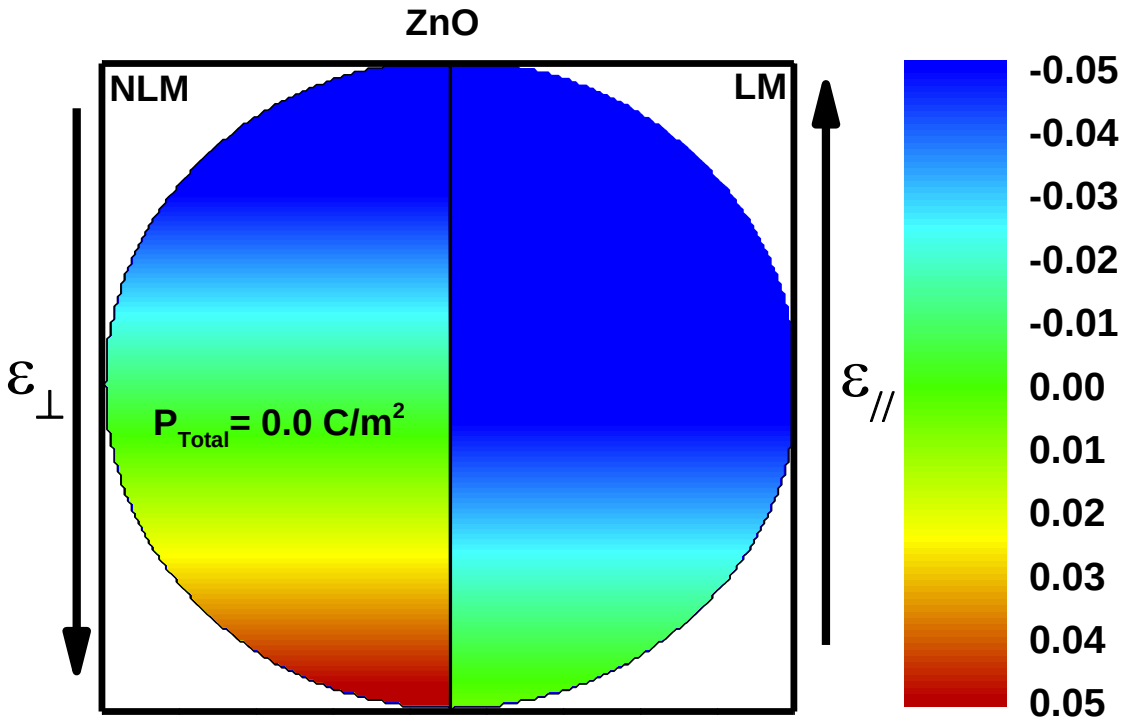

Figure 3.4.2-2: Variation of the polarization (C/m^2) in a cross section of a ZnO nanowire. The perpendicular (parallel) strain varies from -2.8% (+2.8%) to +2.8% (-2.8%). The calculated polarization of the non-linear (quadratic) model (NLM) is on the left half and the classic linear model (LM) on the right. Reproduced from the work of Ref [198].

Distinct differences are observed between the predictions of the LM and NLM. While the NLM predicts a gradient of the polarization ranging from -0.08 C/m^2 at the compressed end of the section, to +0.06 C/m^{2}at the tensile end, the LM polarization instead ranges from -0.12 C/m^2 to 0.0 C/m^2 within the same range of strains.

This clearly demonstrates how the LM and NLM can produce opposite predictions.

The present work constitutes the calculations in the Nitride NWs namely, GaN and InN. We tested the classic LM[47] and our NLM[183] by calculating the polarization in a GaN and InN nanowire subjected to a bending force deforming the cylindrical shape into an arch.

This time in addition we also included the effects of non-linear elasticity (NLE)[103] which have been recently reported to be important for precise calculations. For simplicity we assumed that such deformation would result in a polarization that is isotropic for each circular cross section of the nanowire. We also assume that the resulting perpendicular strain $\varepsilon_{\perp}$ is antisymmetric along the section of the bent cylinder. Since in most materials compressibility is always lower than the ability to withstand tensile deformation, this is a correct assumption only for small strains.

The perpendicular strain is related to the parallel strain $\varepsilon_{||}$ through the elastic constants of the material from Lepkowski[103], and through Eq.(76) and Eq.(77) used in Chapter 3.2.7. Then, the combination of parallel and perpendicular strain is used Eq. (75) from Chapter 3.2.6 to evaluate the polarization.

In Figure 3.4.2-3 and 3.4.2-4 we show the variation of the polarization for the case of GaN and InN respectively, where the perpendicular (parallel) strain $\boldsymbol{\varepsilon}_{\perp}(\boldsymbol{\varepsilon}_{||})$ varies from -4% (+4%) to +4% (-4%). There are marked differences between the predictions of the LM and NLM using the NLE parameters.

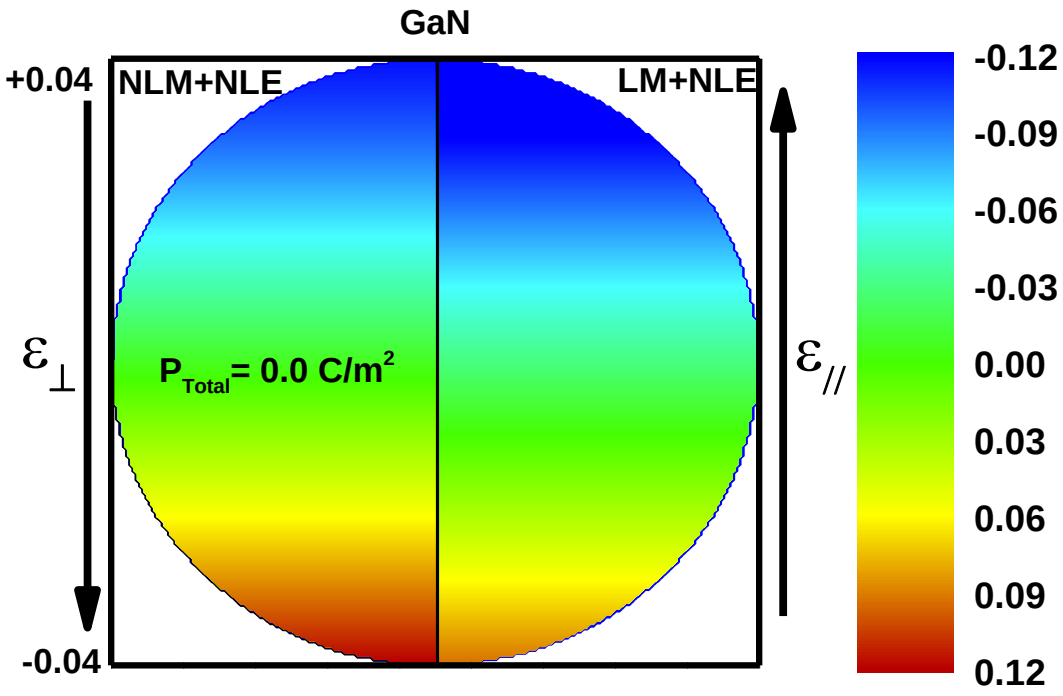

Figure 3.4.2-3: Variation of the polarization (C/m^2) in a cross section of a GaN nanowire. The perpendicular (parallel) strain varies from -4% (+4%) to +4% (-4%). The calculated polarization using NLE parameters of the non-linear (quadratic) model (NLM) is on the left half and the classic linear model (LM) on the right.

In particular, For GaN, the NLM predicts a gradient of the polarization ranging from -0.12 C/m^2 at the compressed end of the section, to +0.12 C/m^2 at the tensile end. The LM polarization instead ranges from -0.15 C/m^2 to +0.09 C/m^2 within the same range of strains.

The case of InN NWs also illustrates similar effect as in GaN NWs. For InN, the NLM predicts the polarization gradient to be ranging from -0.11 C/m^2 at the compressed end of the section, to +0.08 C/m^2 at the tensile end. The LM polarization instead has a range from -0.14 C/m^2 to +0.05 C/m^2 within the same set of strains.

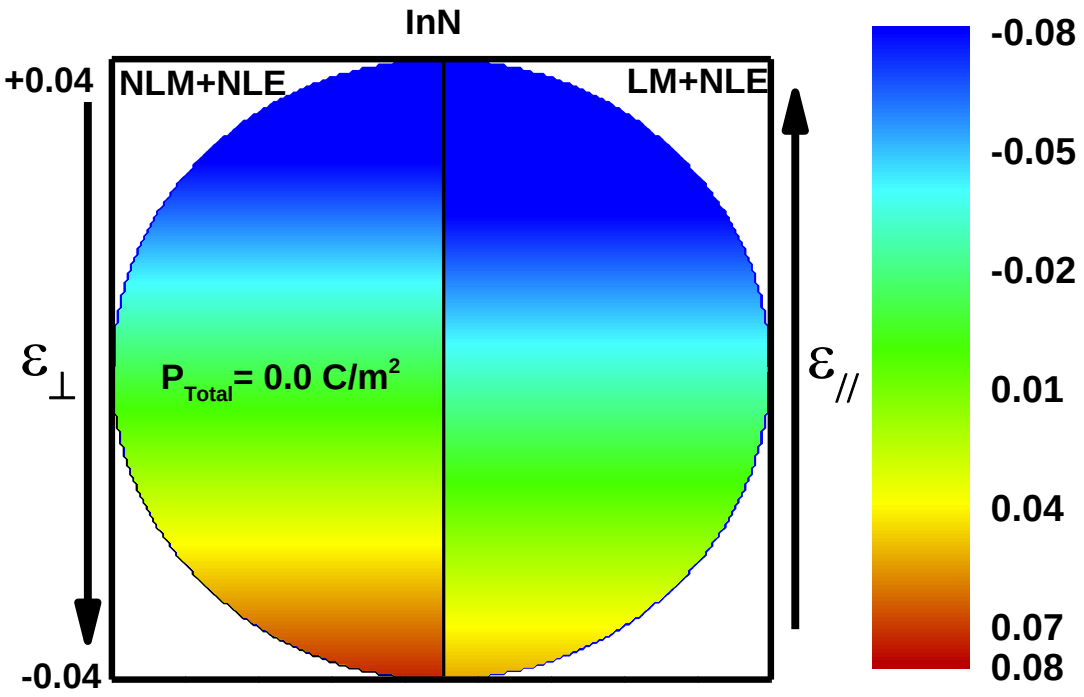

Figure 3.4.2-4: Variation of the polarization (C/m^2) in a cross section of a InN nanowire. The perpendicular (parallel) strain varies from -4% (+4%) to +4% (-4%). The calculated polarization using NLE parameters of the non-linear (quadratic) model (NLM) is on the left half and the the classic linear model (LM) on the right.

Thus the Group III-Nitride NWs show improved predictions of the polarization in NLM compared to the LM unlike ZnO, where we have starking difference between the two models and demonstrated opposite predictions in NLM and LM models.

This is the fundamental set of calculations for the ZnO and Nitride NWs and more calculations needs to be done to observe the effect in NW's optical and electronic properties, critically important for several prospective applications.

3.4.3. Quantum Dots based Devices

3.4.3.1. III-V Quantum Dots

In epitaxially grown InAs/GaAs Quantum Dots the piezoelectric field is directly responsible for lifting the energy degeneracy of the otherwise indistinguishable p-type electron wavefunctions.[59,60,235] This is typically not the only cause of symmetry breaking, as in real structures structural (shape and crystal) asymmetries also play a vital part. We therefore discuss the differences between the piezoelectric potential distributions in the same nanostructure according to the conventional linear model (LM), the non-linear model (NL1) of Tse *et al*[173] and the non-linear model of Beya-Wakata *et al* (NL2)[46]. The results are shown in Figure 3.4.3.1-1.

The InAs/GaAs Quantum Dot used in the calculation is a square-based truncated pyramid with base width of 20 nm, height of 5 nm and a top width of 10 nm. We are showing the PZ potential energy on a (001) plane intersecting the truncated pyramid at 1.5 nm, 2.5 nm and 3.5 nm from the base (30%, 50% and 70% of the total height). There are significant differences. For instance the magnitude of the potential energy is certainly much larger for NL2 compared to LM or NL1 near the top of the pyramid, while it appears comparable closer to the base. This difference closer to the top of the pyramid, where strains are typically larger[236], is the obvious result of the much larger values of e_{124} PZC.

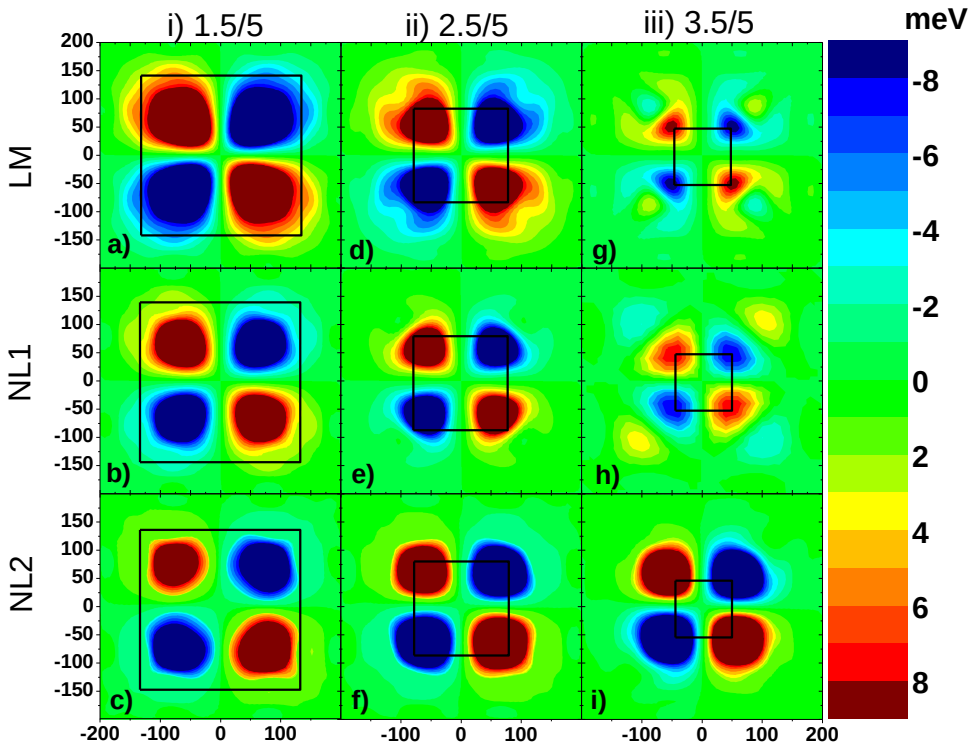

Figure 3.4.3.1-1: Contour plots of piezoelectric potential energy of an InAs/GaAs Quantum Dot displayed columnwise on a (001) plane intersecting the pyramid at 1.5nm, 2.5nm and 3.5nm respectively from the base of the dot: a) Linear Model, b) Our Model and c) Beya-Wakata Model [46]

There are also differences between the spatial distribution of the potential energy between the linear and non-linear models. Closer to the top of the pyramid the linear model appears to have a double structure on each lobe that in NL1 is spatially well separated while it is not at all present in NL2. At the bottom of the pyramid instead it is the LM that predicts the largest magnitude and spatial extension of the potential. Furthermore NL1 and NL2 are comparable in magnitude but NL1 is slightly larger.

We further performed electronic structure calculations of the p-type electron (e1 and e2) energies and wavefunctions using both the full 8-band and 14-band k.p formalism, including the kinetic part with the spin-orbit interaction, strain, the interface Hamiltonian as well as the strain-induced piezoelectric potential. The details of the method used can be

found in Tomić and Vukmirovic´.[140] Both the 14-band and 8-band calculations yield the same result for the difference in energy of the p-state electron wavefunctions within 0.2 meV. Since the electron wavefunctions tend to be spatially located at the bottom of the pyramid, the PZ potential calculated using the LM has the largest energy difference (18.1±0.1 meV). NL1 and NL2 give an energy difference of 10.2±0.1 and 7.85±0.05 meV respectively. The difference between the NL1 and NL2 models is significant. We also tested the influence of quadratic vs. cubic terms in NL1 and concluded that in truncated pyramidal Quantum Dots the quadratic terms are certainly very significant but the cubic terms only add a small positive correction of 0.1 meV. Hence the strain is not sufficiently large to motivate inclusion of the cubic terms.

It is also noticeable that while both NL1 and NL2 under particular strain combinations predict the possibility of positive values of the PZC, in neither of these present calculations this appears to be the case. In Migliorato *et al*[151] it was proposed that the linear PZ field alone was able to account energy differences of the p-type electron wavefunctions in both InAs/GaAs and InGaAs Quantum Dots. The experimental values of these splitting were given in the same work as between 5-8 meV, close to the theoretical prediction. However the experimental data also suggested that the [110] p-electron wavefunction should have been higher in energy compared to its $[1\bar{1}0]$ counterpart. This could have been explained by the PZ field switching from negative to positive as a result of the strain in the nanostructure. However, in truncated pyramidal Quantum Dots not even non-linear models appear to predict a switch of the sign of the piezoelectric potential energy. One cannot exclude that some shapes or sizes of Quantum Dots other than the one used in this work could have strain large enough to be able to switch the polarization from negative to positive. But at present we have to conclude that in experimental observations the degeneracy is mostly due to shape anisotropy counteracting and entirely reversing the effect of the piezoelectric field.

We tested whether in semiconductor InAs/GaAs truncated pyramidal Quantum Dots only quadratic or also cubic terms should be taken into account in electronic structure calculations and confirm that in such structures the strain is not large enough to necessitate inclusion of the cubic piezoelectric coefficients, although corrections due to the linear and quadratic terms (in the diagonal strain components) have a magnitude comparable to the conventional linear model (e_{14} times γ) where the piezoelectric polarization depends only on the shear components of the strain tensor.

3.4.3.2. III-N Quantum Dot Properties

Semiconductor Quantum Dot (QD) systems are an emerging technology as the ideal source of entangled photons ("on demand") for use as single photon sources (SPSs). These SPSs are the building blocks for device applications in secure all-optical quantum-cryptography and quantum information processing.

The current prospect of such devices is based on using Zincblende QD structures. [237,238] QDs based on nitride semiconductors unlock a novel blue and ultraviolet spectral region for the SPSs with the present structures.[239] III-N QDs are also important for applications[240,241,242,243,244,245,246,247] in LED technology and photovoltaic devices.

In contrast to GaN/AlN QD system, the wutzite $In_xGa_{1-x}N$/GaN QDs which emit in the IR region provide an extra degree of freedom in the design of SPSs by varying the indium mole fractions, *x*, of the $In_xGa_{1-x}N$ QD material. In order to control the device operation of InGaN/GaN quantum dot (QD) based optoelectronic devices, the relationship between the excitonic structure and the geometry of the dots needs to be established. This is highly challenging due to the presence of the effects of strain, band mixing, quantum confinement and electron-hole Coulomb interaction present in any quantum-dot system. Furthermore, wurtzite QDs also exhibit a strong built-in electric fields induced by both spontaneous and non-linear piezoelectric polarizations. [183]

Wurtzite InGaN/GaN QDs are favourable for use in SPS devices to be operated at higher temperatures owing to the presence of larger bandgap, band offsets and effective masses compared to the InAs/GaAs system, leading to stronger quantum-confinement effects. The shorter wavelengths of the InGaN/GaN system might be helpful in reducing the sizes of the transmitter and receiver optics for applications in free-space cryptography.[239,248] The emission of InGaN/GaN QDs can be tuned in the green and blue; depending on the Indium content, to have a potentially viable complete visible spectrum. This wavelength range corresponds to the best sensitive range of the ultrafast single-photon detectors.[248] Also, there have been previous reports of InGaN QD based single–dot spectroscopy experiments[249,250] and recent studies on photon-correlation[251,252] to improve the extraction efficiency for emission and detection of single photons from the dots.[253]

SPS applications need larger values of the biexcitonic shift, described as the transition energy difference between the energy of the biexciton to exciton decay and the exciton energy itself. This enables better spectral separation of the transition lines.[239] The built-in electric field has already been recognised to be localizing the electrons at the top and holes at the bottom of the QD.[174,254] Hence, the interaction between the two excitons that form the biexciton complex is dominated by the electron-electron and hole-hole repulsive forces compared to the attractive interaction of the electron and the hole when spatially separated.[255,256] Since with increasing QD height the attractive interaction decreases, the biexcitonic shift increases to the extent of rendering the biexciton unbound. This argument favours the choice of a large QD height. However, for the purpose of quantum efficiency, the optical transition matrix element of the excitonic transition requires to have a sizeable magnitude and this element becomes smaller with increasing QD height (because of the electron and the hole wavefunctions being spatially separated).[254]

Hence according to the argument, small QDs are preferable. Thus, the most suitable QD geometry for SPS applications should comprise of reconciliation between the opposite conditions and it demands a comprehensive exploration of the excitonic properties of InGaN QDs as a function of their geometry and composition.

In this work, we present a systematic study aimed to provide insight into the morphological factors determining the performance of the optimal SPSs based on $In_xGa_{1-x}N$/GaN QD in general and, in particular, variation of the SPSs emission wavelength with In concentration in the QDs.

In our theoretical model single particle electron and hole states of wurtzite $In_xGa_{1-x}N$/GaN QDs were modelled using 8-band $k \cdot p$ Hamiltonians,[143] including second order piezoelectricity (with our parameters) and P_{sp}, strain effect, spin-orbit interaction and crystal-field interaction and additional terms. We obtained the (bi)exciton states using configuration interaction (CI)[257] method and the correction terms for the hexagonal lattice have been introduced using the adapted Makov-Payne method[258] by adding the first few terms in the multipole expansion (monopole, dipole, and quadrupole) in order to compensate the effect of the mirror charges induced by periodic boundary conditions. [259] In this way the model fully replicates the electronic and excitonic structure of an *single* QD.**Error! Bookmark not defined.** Finally we computed the biexcitonic shift, namely the difference between the energy of the exciton transition line and the energy of the transition line from the biexciton to exciton state as shown in Figure 3.4.3.2-1.

The biexcitonic shift is given by $B_{XX} = (E_{XX} - E_X) - E_X$ and in order to obtain bound biexcitons, B_{XX} needs to be negative.

Also, for SPS applications, the value of B_{XX} needs to as large as possible, which provides good spectral separation of the two lines.[239]

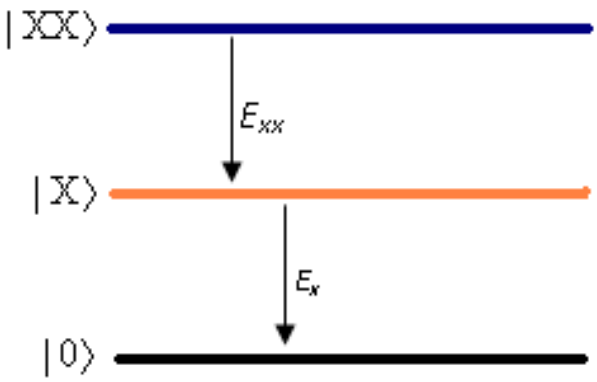

Figure 3.4.3.2-1: Schematic diagram of energy positions of unbound, entangled, and bound biexcitons where $|0\rangle$, $|X\rangle$ and $|XX\rangle$ stands for ground, exciton, and biexciton state respectively.

The importance of the built-in electric field in localizing the electrons at the top of the dot and holes at the bottom of the dot is already known.[174,254] Hence, the stronger repulsive *e-e* and *h-h* interactions between spatially separated electron and hole determine the interaction between two excitons forming a biexciton.[255,256] Thus, in QDs with larger heights, the biexciton remains certainly unbound and B_{xx} increases with increment in height owing to a decrement in the attractive part of the interaction. This certainly supports the proposition that SPSs require large QD heights.

However as it is also important to have a large optical transition matrix element for the exciton transition p_x[239] and large QDs are unsuitable as this element becomes small due to spatial separation of *e* and *h* wavefunctions.

To determine the ideal compromise, the following optimization function[259] has been used to achieve the above conditions as

$$\Xi = (E_{XX} - 2E_X) ln(p_x^{(x)}/p_x^{(0)}) \quad (82)$$

where, $p_x^{(0)}$ is equal to $10^{-4} p_x^{(x),max}$ (10^{-4} is used as a scaling parameter) and $p_x^{(x),max}$ is the max value of $p_x^{(x)}$ for all the QDs. The maxima of the optimization function has small dependence on the $p_x^{(0)}$, when changed within reasonable limits.

Hexagonal truncated pyramidal shapes were used in our work. The dimensions of the QD depend on two parameters, namely the diameter D of the circumscribed circle around the hexagon at $z = 0$ and the truncated pyramid angle between the pyramid facets and base (taken as $\alpha = 30^{o}$) while the QD depends mainly on the aspect ratio (D/h) where *h* represents the QD height. The calculations are performed over a wide range of QDs with In content ranging from 10% to 70%.

For SPS calculations the QD height was varied in the range *h*=1.5nm to *h*=5nm with steps of 0.2nm or 0.1nm. The diameter to height ratio *D/h* was varied from 6 to11 with a step of 1. In calculating the biexcitonic state to be bound or unbound, the aspect ratio (*D/h*) of 4,5,6,7 was considered. The height of the QDs was kept in the range *h*=1-2.1nm with step changes of 0.1nm. Large dots with diameter larger than 30 nm were discarded in the calculations for both cases as the electron and hole wavefunctions become spatially separated by a very large extent and also absence of strong exchange-correlation effects.

The calculations aimed at determining the physical factors affecting the performance of InGan/GaN QD based SPS applications are now discussed.

All the CI calculations involved single particle electron (N_e=12) and hole (N_h=18)states, including both spin polarizations. In InGaN/GaN QDs, the biexciton shift depends on the exciton energy and is being calculated over a wide range of alloy composition in Figure 3.4.3.2-2.

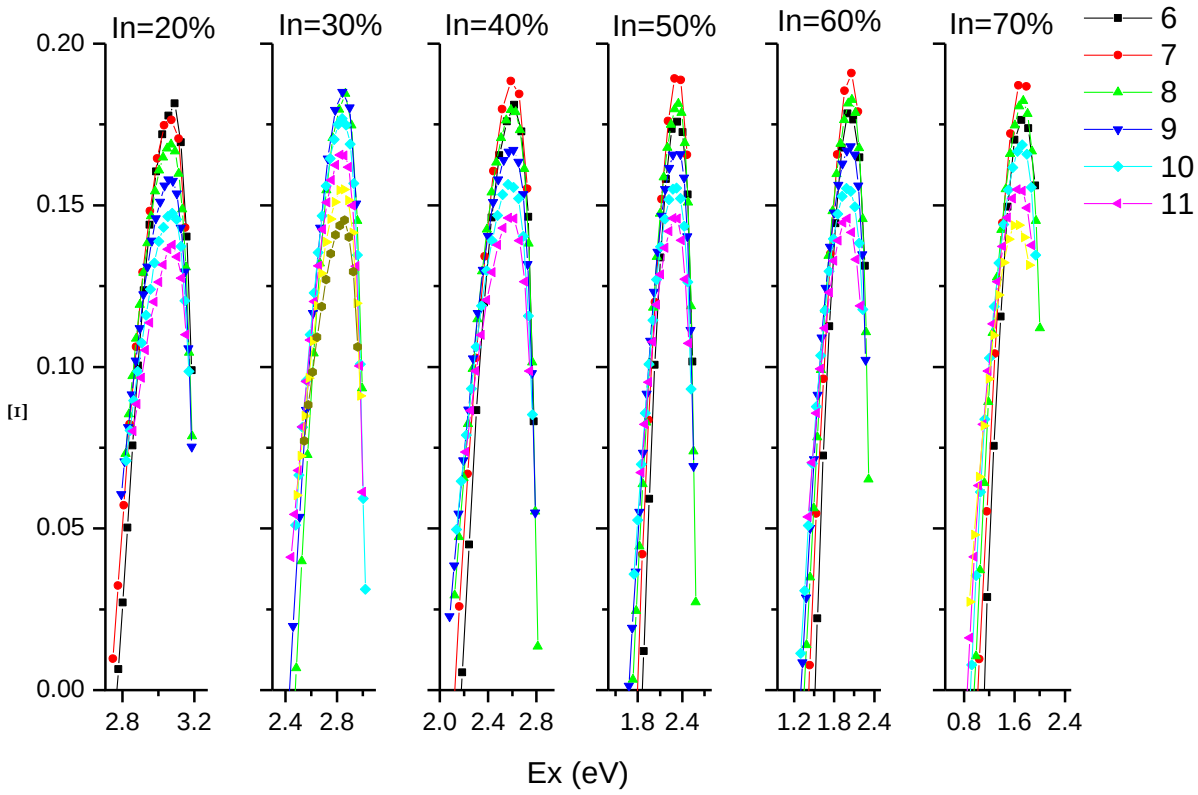

Figure 3.4.3.2-2: The dependence of the optimization function defined as $\Xi(E_{XX})$ on exciton energy for different values of aspect ratios (D/h) and different In concentration in InGaN QDs: (a) In= 20%, (b) In= 30%, (c) In= 40%, (d) In= 50%, (e) In= 60% and (f) In= 70%.

The In concentration in the InGaN QDs was varied from 20% to 70% and for different D/h ratios of 6,7,8,9,10 and 11.

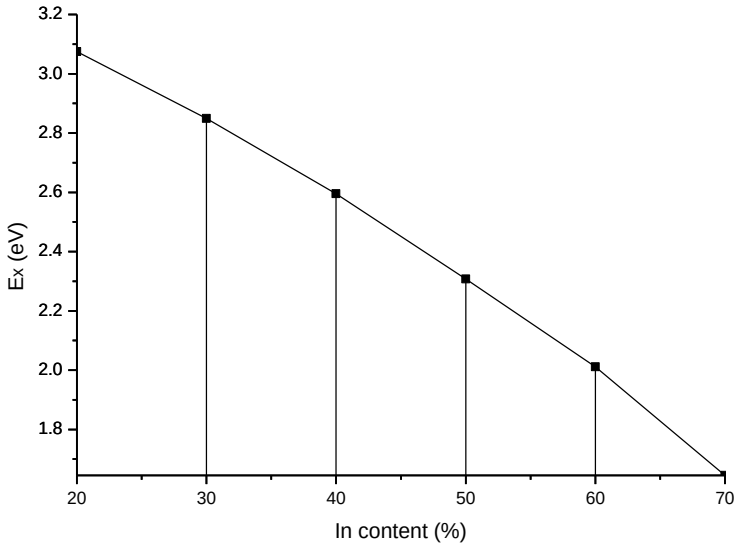

Figure 3.4.3.2-3: Variation of the optimized SPS emission energy/wavelength vs In concentration in QDs

The best choice of size and composition for the InGaN dots are shown to emit over a wide range of the visible spectra, from 1.7-3.1 eV, as evident in Figure 3.4.3.2-3. Hence the emission energy can be tuned in such dots by small variation of the Indium content.

Another important aspect of the excitonic structure at InGaN/GaN QDs is to assess whether the biexciton is bound or unbound. Recent experiments have reported bound biexcitons in small III-N based QDs. [255,260]One of the major shortcomings on the Hartree approximation based theoretical approaches is the lack of implementation of the electron-correlation effects in the model while in principle a CI based approach is capable of calculating such correlations correctly. The direct Coulomb energy of the excitons in a QD can be compensated by the exchange-correlation effect in smaller QDs.

Here, we analysed the impact of our non-linear model with the second order parameters on the QDs formed by $In_xGa_{1-x}N$.

We have calculated for a series of smaller InGaN QDs, the excitonic and biexcitonic states with In content varying from 10% to 70% and as shown in Figure 3.4.3.2-4, we found that using the parameters from our model, bound biexcitons are achievable over a wide range of structures having an alloy composition varying from 20% to 70% and with the exception of the case of 10% In content. All calculations for the exciton and biexciton have been performed for a series of InGaN QDs with aspect ratios (D/h) of 4, 5, 6 and 7 and the outcomes suggest the presence of bound biexcitons across different sizes of the QDs under consideration.

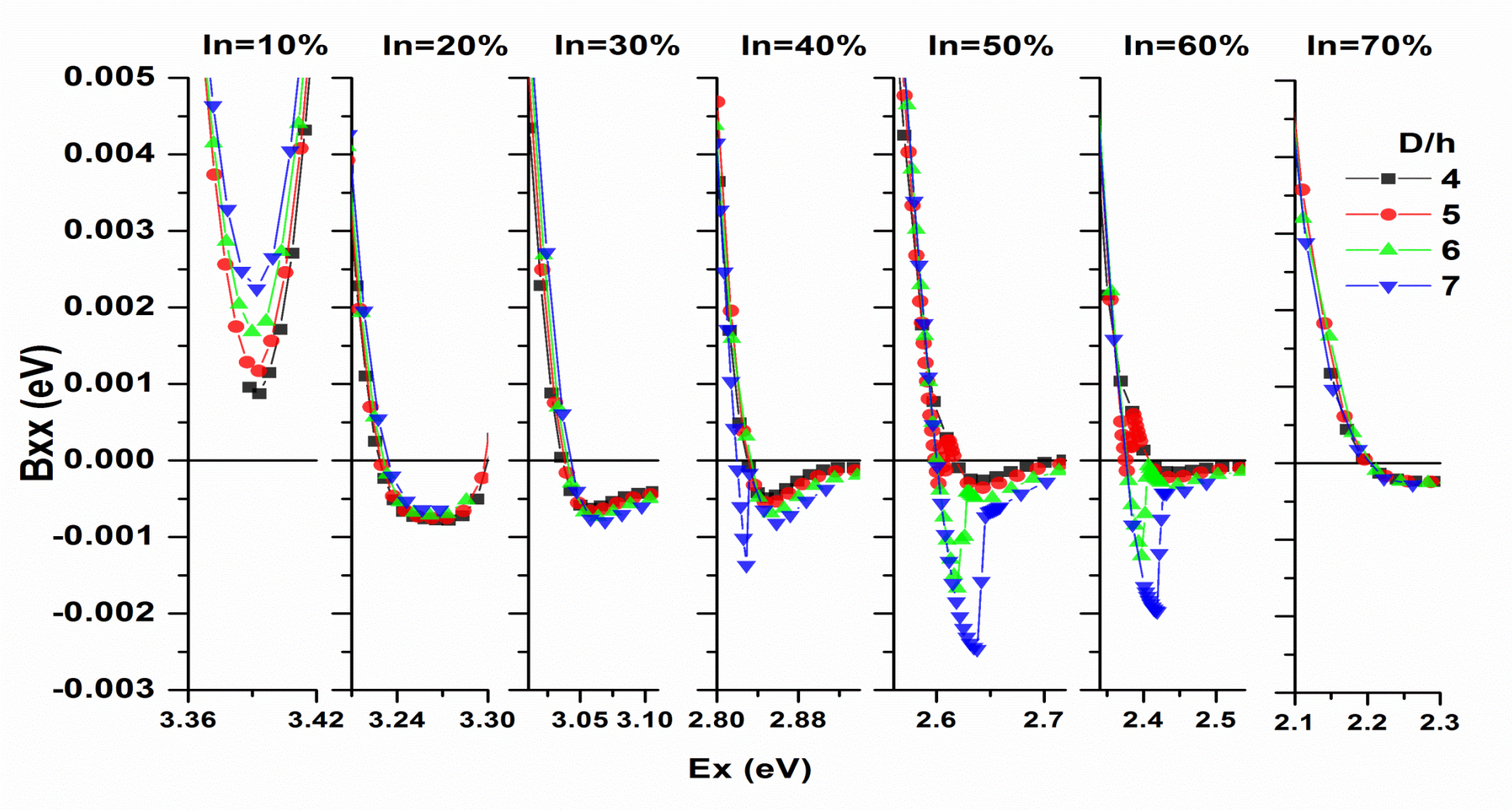

Figure 3.4.3.2.4: Variation of the bound biexcitons appearances for different In concentrations in InGaN QDs: (a) In=10%, (b) In=20%, (c) In=30%, (d) In=40%, (e) In= 50%, (f) In= 60% and (g) In=70% for a range of aspect ratio.

As the alloy content gets lower, the QDs also exhibit shallower confinement leading to lesser number of electron and hole states. This results in unbound biexcitonic states. Another interesting outcome of our calculation for the case of 50% In content and aspect ratio (D/h=5) is that we can observe multiple crossovers providing three different regions of bound biexcitons which could be further exploited in devices. The variation of the alloy composition significantly impacts on the energy of the bound and biexciton state and with the rise in In content in the dots, the emission energy region also shifted towards higher energy.

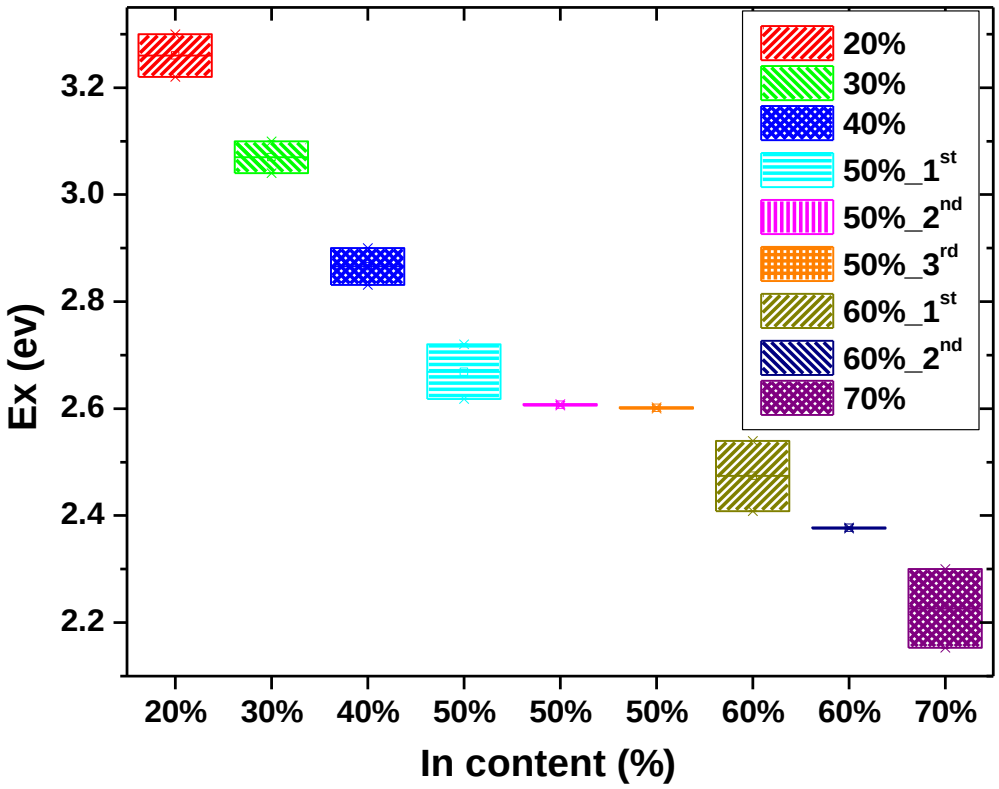

Figure 3.4.3.2-5: Tunability of the bound biexciton (Bxx = 0) emission energy vs In concentration in InGaN QDs.(The coloured boxes represent the different regions of bound biexcitons across different In content in the alloy composition. 50% and 60% In concentration has multiple regions for D/h=5 and are marked as 1st, 2nd and 3rd respectively).

We also considered the particular case of bound biexcitons with negative biexcitonic shift where gradual increment of 10% in the In content provides the tunability of the emission region from 2.15-3.30eV covering the visible light spectra as evident from Figure 3.4.3.2-5. Thus, InGaN QDs can be used for highly tunable devices by regulating the emission region of the bound biexcitons over wide visible spectra through alloy composition.

In Table IX, we show the variation of the excitonic emission energy with the In alloy composition in InGaN/GaN QDs. Thus, similar to QW nanostructures, the effect of strain induced PZ polarization with second order coefficients and P_{sp} has a large influence over the excitonic properties of QDs.

TABLE IX: Alloy composition dependence of the excitonic energy levels in InGaN/GaN quantum dots for bound biexcitons (having a negative biexcitonic shift Bxx<0). The calculations are done over different aspect ratios (D/h) of 4, 5, 6 and 7.

Alloy content (%)	Excitonic energy (eV)
20	3.251
30	3.043
40	2.832
50	2.610
60	2.394
70	2.219

The impact of these findings is widespread as QDs of InGaN can be used for futuristic devices. The tunability of the emission spectra of the excitons and biexcitons in InGaN QDs for different composition of alloy will be of great interest for development of futuristic optoelectronic devices such as multi-exciton generation solar cells and applications based on photon entanglement. Also, the excitonic properties of InGaN QDs remain similar for different sizes of the dots. The non-linear model of piezoelectricity applied in this work has been effective by a substantial amount in the QDs along with the QWs made of III-N materials. In summary, we have shown that with suitable variation of the In concentration between 20% and 80% in single $In_xGa_{1-x}N$/GaN QDs it is possible to design SPS that emit in entire visible spectral region. Using the CI method that include the effect of electron exchange-correlations interactions we have shown that in small QDs, the exchange-correlation effect is sufficient enough to compensate for the increase of the direct Coulomb energy of two excitons in a QD.

4. Conclusions

In this thesis, the author has discussed the origin of non-linear piezoelectricity and its influence on the polar III-V, III-N and II-VI semiconductors. The field of piezotronics and its research potential has also been reviewed in much detail. The research arena has wide range of applications in self-powered circuits for wireless sensors, nanorobotics, interfacing between human and computer, medical science, tactile sensors imitating human skin, nanogenerators for portable devices, solar cells, LEDs and other optoelectronic devices.

In recent years, a new theoretical understanding of the nature of the PZ polarization and resulting electric fields in semiconductor crystals has emerged [150,151] which advocated the necessity to include non-linear piezoelectric coefficients (PZCs) even in the limit of vanishing strain in order to correctly estimate the effect of the presence of strain induced electric fields on the electro-optical properties of polar semiconductor nanostructures.[152,153,154,157] Such studies have demonstrated that the assumption that the PZ effect is a linear effect in the strain is incorrect and that the magnitude of the second order PZCs is of the same order of magnitude as the first order, even in the range of [-0.1÷0.1] of strains, which is typical for nanostructures.[151] Furthermore non-linear effects, because of their ability to switch the sign of the PZ polarization from negative to positive depending on the applied strain[170], have been shown to provide an additional and unexpected degree of freedom in the design of optoelectronic components.

Although previous works were performed for the zincblende III-V semiconductors[151,170], this work focuses almost completely on the effect of non-linear piezoelectricity in III-Nitride semiconductors in the Wurtzite phase and the strain dependent non-linear PZCs are reported for the first time. The calculations of the parameters for both the

Spontaneous Polarization and the first and second order PZCs of Group III-Nitrides, in the framework of ab initio DFT and DFPT in conjunction with the semi empirical formulation of Harrison[57] has been performed.

Other models[47,180] of piezoelectricity have been proposed and controversy arose because they give different results for PZCs and in particular, the spontaneous polarization values. It was always difficult to pinpoint the origin of the discrepancy but there was a suspicion that it was due to an incorrect understanding of what the quantity Z* is compared to Z_H^*.

In the case of ZB III-As semiconductors, the experimental data from InGaAs QW was never conclusive to determine which model is correct. Instead, the III-Nitride semiconductors offer more data in the form of the spontaneous polarization and 3 PZCs. It was therefore believed that such material system could have provided the correct test bed for our model.

Although our non-linear model on piezoelectricity is self-consistent and provides the PZC and Spontaneous Polarization values within the same regime, the model utilizes Z_H^* as a fitting parameter, typically found to be 25% to 65% of the widely used effective charge (Z*). This might create some scepticism about the model and the outcomes but the model is verified by the precise predicted field estimates in close agreement with the experimental results.

It has been demonstrated that compared to previous calculations of linear theory of piezoelectricity and larger spontaneous polarization, the new non-linear model to second order described in this work with much reduced Spontaneous Polarization provides more precise predictions to available experimental data for the piezoelectric field in the quantum well for various III-N materials and their alloys.

More interestingly, there has been a debate within the scientific community about the sign of one of the PZC, e_{15}, and the issue has been dealt with through investigation of the

existing literature. The correct sign of e_{15} has thus been found in our research work validating with the original experimental result.

Also, by selecting particular values of the molar fractions in AlGaN and InGaN alloys, predictions of matching the spontaneous polarization terms and reduce the total piezoelectric field to the strain induced one alone. This could have applications in the design of optoelectronic devices.

In order to validate even more the model and its prediction, the author has analyzed the strain dependence of the piezoelectric field in the active region of two pseudomorphically strained $In_xGa_{1-x}N$ MQWs designed for blue (x=0.14) and green (x=0.26) light emission.

In both cases, non-linear elasticity along with the non-linear piezoelectricity was also introduced and as expected, a major reduction in the internal piezoelectric field estimates as a function of tensile strain was observed as a function of strain in both cases.

The results confirmed the experimental measurements of the change in the internal piezoelectric fields to the change in optical efficiency, which was measured by our collaborators using a system comprising a helium compressor to implement high hydrostatic presssure. While our model predicted a significant field reduction in accordance with the experiments, the classic linear model predicted a completely opposite trend of increment of the internal field with tensile strain, contrary to our experimental data. With introduction of non-linear elasticity, the difference between the two models became even more evident. This has also been confirmed by other research groups and the fact that the linear model provides incorrect field estimates is becoming increasingly accepted.

As tensile strain generation is possible by growing the well region of the LED structure on a semiconductor layer with a larger lattice parameter than that of GaN, a unique and novel approach for LED design has been proposed later on by adding a relaxed InGaN

metamorphic layer. The optical matrix elements and the ensuing spontaneous emission rate for the new structures are consistent with experimental data in the literature and the new LED devices with the proposed structures are expected to have an increment in the optical emission by a 10% higher output power. Similar propositions of addition of tensile strain to the device active region has been observed to be beneficial experimentally by another research group[226], while theoretical modelling of the band offsets and interface polarization in InN/GaN superlattices and their dependence on strain had also concluded that the strain conditions could be utilized to potentially control the device properties[194].

Furthermore, the author performed polarization calculations for III-N Nanowires, namely GaN and InN, and demonstrated that similar to the results obtained in ZnO nanowires, we can expect much improved estimates in our non-linear model compared to the linear model. These are fundamental calculations for both types of nanowires and more complex computations are required to study the non-linear piezoelectric effect in the optical and electronic properties of the nanowires. In particular, the equilibrium piezoelectric potential electrical current distribution will need to be incorporated in our model to correctly estimate the flow of charge carriers.

Quite similar to Quantum well nanostructures, the effects of our non-linear model has also large influence over the excitonic properties of QDs.

The author investigated the non–linear piezoelectric effect in semiconductor InAs/GaAs Quantum Dots, truncated pyramidal in shape, to study whether only quadratic or also cubic terms are important in electronic structure calculations. It is observed that in such structures, the absence of very large strain often does not need the requirement of the cubic piezoelectric coefficients. But the linear and quadratic correction terms (in the

diagonal strain components) helps to provide a precise estimate of the piezoelectric polarization in comparison to the conventional linear model of piezoelectricity.

The excitonic and biexcitonic emission spectra in different InGaN quantum dots show wide tunability for different alloy compositions. It can be exploited in devices as multi-exciton generation solar cells and photon entanglement applications. While the excitonic properties of the dots remain identical even for different sizes. Significant effect of non-linear piezoelectricity has been observed in this III-N dots similar to the wells. Results from our calculations suggest the enablement of design of single photon source emitting in the visible spectra through wide variation of the Indium content (from 20% to 80%) in the single InGaN quantum dots.

In summary, we developed a model on non-linearities in piezoelectricity, validated it on real devices and experimental data, also confirmed by others, and exploited the non-linear effect to make unexpected predictions of electro-optical behaviour in a variety of nanostructures.

4.1. Future Scope

Our research is now an integral part of the global piezotronics effort and we hope to contribute more in coming years.

The methodology used in this work has been well tested and validated by the experimental results for the Group III-Nitride materials. The calculations performed for different nanostructures such as quantum wells, quantum nanowires and quantum dots provide the impetus for further investigation in the field. The study of other materials in Group III-Vs and II-VIs can be carried out transferring the methodology for non-linear piezoelectricity already developed. The current model can be expanded not only to study the non-linearities in ZnSe, III-P and III-Sb semiconductors and their alloys, but also in different wurtzite and zincblendes crystal phases.

Preliminary calculations have been performed in the case of the nanowires and more in depth analysis is required for the case of InGaN nanowires, which is really important for new optoelectronic device designs. Research can also be performed for the design of III-V nanowires, particularly the InGaP ones, where the ZB-WZ polytypism impacts the behaviour of the nanostructures by a large extent.

Although the methodology provides much better agreement with the experimental data compared to the linear model of piezoelectricity, the effect of converse piezoelectric effect has not been studied and could well enhance the outcome.

Also, the study of Hirshfeld charge calculation for Z_H^* and investigation of non linear elasticity using CASTEP can also be carried out.

Furthermore, real device design and properties can be analysed involving the electronic structure calculations and Poisson and Schrodinger equation solver.

5. References

[1] Z. W. Pan, Z. R. Dai, Z. L. Wang, Science **291**, 1947 (2001).
[2] F. Zhang, S. Niu, W. Guo, G. Zhu, Y. Liu, X. Zhang, and Z. L. Wang, ACS Nano **7** (5), 4537 (2013).
[3] Y. Zhang, Y. Yanga and Z. L. Wang, Energy Environ. Sci., **5**, 6850 (2012).
[4] X. Y. Kong, Z. L. Wang, Nano Lett. **3**, 1625 (2003).
[5] Y. Zhang and Z. L. Wang, Adv. Mater. **24**, 4712 (2012).
[6] Z. L. Wang, Nano Today, **5**, 540-552 (2010)
[7] Z. L. Wang, J.H. Song, Science **312**, 242 (2006).
[8] W. L. Hughes, Z. L. Wang, J. Am. Chem. Soc. **126**, 6703 (2004).
[9] C-T. Huang, J. Song, W-F. Lee, Y. Ding, Z. Gao, Y. Hao, L-J. Chen, and Z. L. Wang, Journal of the American Chemical Society **132** (13), 4766 (2010).
[10] L. Lin, C.H. Lai, Y.F. Hu, Y. Zhang, X. Wang, C. Xu, R.L. Snyder, L.J. Chen, Z. L.Wang, Nanotechnology **22**, 475401 (2011).
[11] W.Zu, X. Wen and Z. L.Wang, Science, 340, 952 (2013).
[12] Z. L. Wang, Adv. Funct. Mater. **18**,3553 (2008).
[13] M. Lee, J. Bae, J. Lee, C. S. Lee, S. Hong, Z. L. Wang, Energ. Environ. Sci. **4**, 3359 (2011).
[14] Z. L. Wang, Adv. Mater. **24**, 280 (2012).
[15] Y. F. Hu, L. Lin, Y. Zhang, Z. L. Wang, Adv. Mater. **24**, 110 (2012).
[16] http://www.bbc.co.uk/news/science-environment-22302487
[17] http://news.cnet.com/8301-17938_105-57581627-1/new-smart-skin-so-sensitive-it-rivals-the-real-thing/
[18] http://www.natureworldnews.com/articles/1600/20130426/researchers-create-material-thats-sensitive-human-fingertip.htm
[19] http://www.theengineer.co.uk/electronics/news/robots-given-more-accurate-sense-of-touch/1016163.article
[20] http://www.scienceworldreport.com/articles/6490/20130426/smart-skin-gives-robots-adaptive-sense-touch-artificial-possibility.htm
[21] http://physicsworld.com/cws/article/news/2013/apr/26/nanowire-transistor-array-as-touch-sensitive-as-human-skin
[22] http://eandt.theiet.org/news/2013/apr/touch-robot.cfm
[23] Z. L. Wang, "*Piezotronics and Piezo-Phototronics"*, Microtechnology and MEMS, Springer-Verlag Berlin Heidelberg 2012.
[24] Z. L. Wang, MRS Bulletin, **37**, 814 (2012).
[25] C-Y. Chen, G. Zhu, Y. Hu, J-W. Yu, J. Song, K-Y. Cheng, L-H. Peng, L-J. Chou, and Z. L. Wang, ACS Nano **6** (6), 5687 (2012).
[26] R. Agrawal and H. D. Espinosa, Nano Lett. **11**, 786 (2011).
[27] Y. Hu, Y. Zhang, L. Lin, Y. Ding, G. Zhu, and Z. L. Wang, Nano Letters **12** (7), 3851 (2012).
[28] J. A. Czaban, D. A. Thompson and R. R. LaPierre, Nano Lett. **9**, 148 (2009).
[29] B. Hua, J. Motohisa, Y. Kobayashi, S. Hara and T. Fukui, Nano Lett. **9** (1), 112 (2009).
[30] J. Wang, M. S. Gudiksen, X. Duan, Y. Cui and C. M. Lieber, Science **293** (5534), 1455 (2003).
[31] P. K. Mohseni, A. Behnam, J. D. Wood, C. D. English, J. W. Lyding, E. Pop, and X. Li, Nano Lett. **13**, 1153 (2013).
[32] S. S. Yi, G. Girolami, J. Amano, M. S. Islam, S. Sharma, T. I. Kamins and I. Kimukin, Appl. Phys. Lett. **89**, 33121 (2006).
[33] K. Tomioka, M. Yoshimura and T. Fukui, Nature **488**, 189 (2012).
[34] Z. L. Wang, Materials Today, 7, p.23 (2004).

[35] W.L. Hughes, Z.L. Wang, J. Am. Chem. Soc. **126**, 6703 (2004).
[36] Q.X. Zhao , M. Willander , R.R. Morjan , Q.H. Hu , E.E.B. Campbell, Appl. Phys. Lett. **83**, 165 (2003).
[37] X.D. Wang, C.J. Summers, Z.L. Wang, Nano Lett. **3**, 423 (2004).
[38] S. Xu, Z.L. Wang, Nano Res. **4**, 1013 (2011).
[39] Y.G. Wei, W.Z. Wu, R. Guo, D.J. Yuan, S. Das and Z.L. Wang, Nano Lett.**10**, 3414 (2010).
[40] A. Mishra, L. V. Titova, T. B. Hoang, H. E. Jackson, L. M. Smith, J. M. Yarrison-Rice, Y. Kim, H. J. Joyce, Q. Gao, H. H. Tan and C. Jagadish, Appl. Phys. Lett. **91**, 263104 (2007).
[41] J. Bao, D. C. Bell, F. Capasso, J. B. Wagner, T. Mårtensson, J. Tragårdh, L. Samuelson, Nano Lett. **8**, 836 (2008).
[42] T. B. Hoang, A. F. Moses, H. L. Zhou, D. L. Dheeraj, B. O. Fimland, H. Weman, Appl. Phys. Lett. **94**, 133105 (2009).
[43] H. Shtrikman, R. Popovitz-Biro, A. Kretinin, L. Houben, M. Heiblum, M. Bukała, M. Galicka, R. Buczko, and P. Kacman, Nano Lett **9** (4), 1506 (2009).
[44] R. E. Algra, M. A. Verheijen, M. T. Borgström, L-F. Feiner, G. Immink, W. J. P. van Enckevort, E. Vlieg and E. P. A. M. Bakkers, Nature **456**, 369 (2008).
[45] P. Caroff, K. A. Dick, J. Johansson, M. E. Messing, K. Deppert and L. Samuelson, Nature Nanotechnol. **4**, 50 (2009).
[46] A. Beya-Wakata, P-Y Prodhomme and G. Bester, Phys. Rev. B **84**, 195207 (2011).
[47] F. Bernardini, V. Fiorentini, D. Vanderbilt, Phys. Rev. B 56, R10024 (1997).
[48] J. F. Nye, Physical Properties of Crystals, Oxford, 1957.
[49] W.G Cady, Piezoelectricity (McGraw-Hill, New York, 1946).
[50] S. Adachi, "Physical Properties of III-V Semiconductor Compounds",Wiley, New York (1992).
[51] S. Muensit, E. M. Goldys and I. L. Guy, Appl. Phys. Lett. **75**, 4133 (1999).
[52] K. Tsubouchi and N. Mikoshiba, IEEE Trans. Sonics Ultrason. SU-32, 634 (1985).
[53] A. Hangleiter, F. Hitzel, S. Lahmann and U. Rossow, Appl. Phys. Lett. **83**, 1169 (2003).
[54] I.B. Kobiakov, Sol. Stat. Comm. **35**, 305 (1980).
[55] "Spontaneous and piezoelectric polarization in nitride heterostructures", Edward T. Yu.
[56] A. Bykhovski, B. Gelmont, M. Shur, A. Khan, J. Appl. Phys.**77**, 1616 (1995).
[57] W. A. Harrison, Electronic Structure and Properties of Solids, Dover Publications Inc., New York, (1989).
[58] L. Kleinman, Phys. Rev. **128**, 2614 (1962).
[59] M. A. Migliorato, D. Powell, S. L. Liew, A. G. Cullis, P. Navaretti, M. J. Steer, and M. Hopkinson, J. Appl. Phys., 96, 5169-5172 (2004)
[60] M.A. Migliorato, D. Powell, E.A. Zibik, L.R. Wilson, M. Fearn, J.H. Jefferson, M.J. Steer, M. Hopkinson, A.G. Cullis, Physica E 26, 436 (2005).
[61] M. Grundmann, O. Stier, and D. Bimberg, Phys. Rev. B 52, 11969 (1995).
[62] J. H. Davies, J. Appl. Phys. 84, 1358 (1998).
[63] O. Stier, M. Grundmann, and D. Bimberg, Phys. Rev. B 59, 5688 (1999).
[64] M.J. Romeroa, D. Araújoa, J.L. Sánchez-Rojasb, E. Callejab, E. Muñozb, R. García, Microelectronics Journal **30,** 413 (1999).
[65] S. Rekayaa, L. Sfaxia, L. Bouzaïenea, H. Maarefa, C. Bru-Chevallier, Mat. Sci. and Eng. C **28**, 906 (2008).
[66] J.M. Ballingall, P.A. Martin, J. Mazurowski, P. Ho, P.C. Chao, P.M. Smith, K.H.G. Duh Thin Solid Films, **231**, 95(1993).
[67] T. Mimura, "*Semiconductors and Semimetals"*, Vol. 30, Issue C, Pages 157-193 (1990).
[68] G. Deligeorgis, G. Dialynas, Z. Hatzopoulos, and N. T. Pelekanos, Appl. Phys. Lett. **90**, 121126 (2007).
[69] M. Möller, A. Hernández-Mínguez, S. Breuer, C. Pfüller, O. Brandt, M. M de Lima, A. Cantarero, L. Geelhaar, H. Riechert and P. V. Santos, Nanoscale Res. Lett. **7**, 247 (2012).
[70] G. E. Dialynas, S. Kalliakos, C. Xenogianni, M. Androulidaki, T. Kehagias, P. Komninou, P. G. Savvidis, Z. Hatzopoulos and N. T. Pelekanos, J. Appl. Phys. **108**, 103525 (2010).
[71] G. E. Dialynas, N. Chatzidimitriou, S. Kalliakos, S. Tsintzos, P. G. Savvidis,

Z. Hatzopoulos and N. T. Pelekanos, Phys. Status Solidi A **205**, 2566 (2008).
[72] D. Barettin, A. V. Platonov, A. Pecchia, V. N. Kats, G. E. Cirlin, L. P. Soshnikov, A. D. Bouravleuv, L. Besombes, H. Mariette, M. Auf der Maur and A. D. Carlo, IEEE Journal of Selected Topics in Quantum Electronics, **19**, 1901209 (2013).
[73] G. J. Sullivan, M. Y. Chen, J. A. Higgins, J. W. Yang, Q. Chen, R. L. Pierson, B. T. McDermott, IEEE Electron Device Lett. 19, 198 (1998).
[74] S. C. Binari, J. M. Redwing, G. Kelner, W. Kruppa, Electron. Lett. **33**, 242 (1997).
[75] Y. F. Wu, B. P. Keller, S. Keller, D. Kapolnek, P. Kozodoy, S. P. DenBaars, U. K. Mishra, Appl. Phys. Lett. **69**, 1438 (1996).
[76] J. M. Van Hove, R. Hickman, J. J. Klaassen, P. P. Chow, P. P. Ruden, Appl. Phys. Lett. 70, 2282 (1997).
[77] Q. Chen, J. W. Yang, A. Osinsky, S. Gangyopadhyay, B. Lim, M. Z. Anwar, M. A. Khan, D.Kuksenkov, H. Temkin, Appl. Phys. Lett. **70**, 2277 (1997).
[78] S. Nakamura, G. Fasol, The Blue Laser Diode: GaN Based Light Emitters and Lasers (Springer-Verlag, Berlin, 1997).
[79] R. D. Underwood, S. Keller, U. K. Mishra, D. Kapolnek, B. P. Keller, and S. P. DenBaars, J. Vac. Sci. Technol. B, Vol. 16, No. 2, 822 (1998).
[80] A. Bykhovski, B. Gelmont, and M. S. Shur, J. Appl. Phys. **74**, 6734 (1993).
[81] P. M. Asbeck, E. T. Yu, S. S. Lau, G. J. Sullivan, J. Van Hove, and J. M. Redwing, Electron. Lett. **33**, 1230 (1997).
[82] R. Gaska, J. W. Yang, A. D. Bykhovski, M. S. Shur, V. V. Kaminski, and S. M. Soloviov, Appl. Phys. Lett. **72**, 64 (1998).
[83] E. T. Yu, G. J. Sullivan, P. M. Asbeck, C. D. Wang, D. Qiao, S. S. Lau, Appl. Phys. Lett.**71**, 2794 (1997).
[84] G. Martin, A. Botchkarev, A. Rockett, H. Morkoç, Appl. Phys. Lett. **68**, 2541 (1996).
[85] E. T. Yu, X. Z. Dang, L. S. Yu, D. Qiao, P. M. Asbeck, S. S. Lau, G. J. Sullivan, K. S. Boutros, and J. M. Redwing, Appl. Phys. Lett. **73**, 1880 (1998).
[86] T. Takeuchi, S. Sota, M. Katsuragawa, M. Komori, H. Takeuchi, H. Amano, I. Akasaki, Jpn. J. Appl. Phys. **36**, L382 (1997).
[87] Y-S. Choi, J-W. Kang, D-K. Hwang and S-J. Park, IEEE Trans. on Electr. Dev. **57**, 26 (2010).
[88] S. C. Minne, S. R. Manalis, and C. F. Quate, Appl. Phys. Lett. 67, **3918** (1995).
[89] B. A. Buchine, W. L. Hughes, F. L Degertekin and Z. L. Wang, Nano Lett. **6**, 1155 (2006).
[90] K-H. Kim, Brijesh Kumar, K. Y. Lee, H-K. Park, J-H. Lee, H. H. Lee, H. Jun, D. Lee and S-W Kim, Sci Rep. **3,** 2017 (2013).
[91] J. Shi, M. B. Starr, H. Xiang, Y. Hara, M. A. Anderson, J-H Seo, Z Ma and X. Wang, | Nano Lett., **11**, 5587 (2011).
[92] M. T. Ong and E. J. Reed, ACS Nano **6**, 1387 (2012).
[93] D. C. Elias, R. R. Nair, T. M. G. Mohiuddin, S. V. Morozov, P. Blake, M. P. Halsall, A. C. Ferrari, D. W. Boukhvalov, M. I. Katsnelson, A. K. Geim, K. S. Novoselov, Science **323**, 610 (2009).
[94] J. T. Robinson, J. S. Burgess, C. E. Junkermeier, S. C. Badescu, T. L. Reinecke, F. K. Perkins, M. K. Zalalutdniov, J. W. Baldwin, J. C. Culbertson, P. E. Sheehan, and E. S. Snow, Nano Lett. **10**, 3001 (2010).
[95] R. Martin, (2004). "Electronic Structure: Basic Theory and Practical Methods", Cambridge University Press.
[96] M. P. Allen and D. J. Tildesley, *"Computer simulation of liquids"*, Clarendon Press (1989).
[97] I. Souza and J. Martins Phys. Rev. B **55**, 8733 (1997).
[98] M. Parrinello and A. Rahman, Phys. Rev. Lett. **45**, 1196 (1980).
[99] M. C. Payne, M. P. Teter, D. C. Allan, T. A. Arias and J. D. Joannopoulos, Reviews of Modern Physics **64**(4), 1045, (1992).
[100] P. K. Davies, D. J. Singh, "*Fundamental physics of ferroelectrics 2003: Williamsburg, Virginia*", AIP Conference Proceedings **677** (2003).
[101] C. Kittel (2005) *"Introduction to solid state physics"*, Wiley.
[102] M. J. Lax (2001) "*Symmetry Principles in Solid State and Molecular Physics*",

Dover Publications.
[103] S. P. Łepkowski, Phys. Rev. B, **75**, 195303 (2007).
[104] K. Burke, "*The ABC of DFT*" (2007).
[105] P. Hohenberg and W. Kohn, Phys. Rev. **136** (1964).
[106] W. Kohn and L. J. Sham, Phys. Rev. **140**(1965)
[107] W. Kohn, Rev. Mod. Phys. **71**, 1253 (1999).
[108] Proofs of the two theorems can be found in, Electronic Structure pg (123), R.M Martin, Cambridge University Press (2004).
[109] A.E. Mattson, "In pursuit of the 'Divine' functional", Science **298**,759(2002).
[110] Density Functional Theory <http://www.physics.ohio-state.edu/~aulbur/dft.html>
[111] M. Payne et al, Rev. Mod. Phys., **64**, 1045 (1992).
[112] R. Garg, PhD. Thesis on "Structural and electronic properties of III-V semiconductors studied through ab initio techniques and Empirical Tight Binding" (2009).
[113] D. M. Ceperley and B. J. Alder, Phys. Rev. Lett. **45**, 566 (1980).
[114] E. Wigner Phys. Rev. **46**, 1002 (1934).
[115] J. P. Perdew, Y. Wang, Phys. Rev. B **45,** 13244 (1992).
[116] J. P. Perdew, A. Zunger, Phys. Rev. B **23,** 5048 (1981).
[117] G.P Srivastava, "An excellent review can be found in Theoretical Modelling of Semiconductor Surfaces", World Scientific (1999).
[118] R. Jones, O. Gunnarsson, Rev. Mod. Phys. **61**, 689 (1989).
[119] A. E. Mattson, P. A. Schultz, M. P. Desjarlais, T. R. Mattson, K. Leung, Modelling Simul. Mater. Sci. Eng.**13** (2005) R1- R31.
[120] D. Hamann Phys. Rev. Lett. **43**, 1494 (1979).
[121] N Troullier Phys. Rev. B **43**, 1993 (1991).
[122] D.Vanderbilt, Phys Rev B **41**,7892 (1990).
[123] S. Louie, Phys. Rev. B **26**,846 (1982).
[124] D. Chadi, Phys. Rev. B, **8**,5587 (1973).
[125] H. Monkhorst, Phys. Rev. B **13**, 5189 (1976).
[126] P. Pulay, Mol. Phys. **17**, 197(1969).
[127] H. Hellmann, F. Deuticke, *Einführung in die Quantenchemie*, Leipzig, 285 (1937).
[128] R. P. Feynman, Phys. Rev. **56**, 340–343 (1939).
[129] S. Froyen, M. L. Cohen, Phys. Rev. B, **29**,3770 (1982)
[130] S. G. Louie, S. Froyen, M. L. Cohen, Phys. Rev. B **26**, 1738 (1982).
[131] S. Froyen, M. L. Cohen, Phys. Rev. B **28**, 3258 (1983).
[132] M. T. Yin and M. L. Cohen, Phys. Rev. B **26**, 3259 (1982).
[133] M. T. Yin and M. L. Cohen, Phys. Rev. B **26**, 5668 (1982).
[134] A. García, M. L. Cohen, J. H. Eggert, F. Moshary, W. J. Evans, K. A. Goettel and I. F. Silvera, Phys. Rev. B **45**, 9709 (1992).
[135] A. Yoshida, A. Wakahara and H. J. Kim, The International Conference on Electrical Engineering, O-**069** (2008).
[136] G. Xiao-Ju, X. Bo, L. Zhong-Yuan, Y. Dong-Li, H. Ju-Long and G. Li-Cong, Chin. Phys. Lett. **25**, 6, 2158 (2008).
[137] V. Timon, S. Brand, S. J. Clark, R. A. Abram, J. Phys.: Condens. Matter, **16**, 531 (2004).
[138] G.Y. Gao, K.L. Yao, Z.L. Liu, Y.L. Li, Y.C. Li and Q.M. Liu, Solid State Communications **138**, 494 (2006).
[139] S**.** Q. Wang and H. Q. Ye, J. Phys.: Condens. Matter, **17**, 4475 (2005).
[140] S. Tomić and N. Vukmirović, Phys. Rev. B **79**, 245330 (2009).
[141] J. Singh "Electronic and Optoelectronic Properties of Semiconductor Structures", Cambridge University Press (2003).
[142] J. Luttinger and W. Kohn, Phys. Rev. **97**, 869 (1955).
[143] S. L. Chuang and C. S. Chang, Phys. Rev. B **54**, 2491(1996).
[144] S. Tomić and N. Vukmirović, J. Appl. Phys. **110**, 053710 (2011).
[145] S.A. Choulis, T.J.C. Hosea, S. Tomic, M. Kamal-Saadi, A. R. Adams, E.P. O'Reilly, B.A.Weinstein, and P. J. Klar, Phys. Rev. B **66**,165321 (2002).

[146] U. Aeberhard, R. Vaxenburg, E. Lifshitz and S. Tomić, Phys. Chem. Chem. Phys., **14**, 16223 (2012).
[147] R. M. Martin, Phys. Rev. B **5**, 1607(1972).
[148] W. G. Cady, Piezoelectricity (McGraw-Hill, New York, 1946).
[149] G. Bester, and A. Zunger, Phys. Rev. B **71**, 045318(2005).
[150] G. Bester, X. Wu, D. Vanderbilt, and A. Zunger, Phys. Rev. Lett. **96**, 187602 (2006).
[151] M. A. Migliorato, D. Powell, A. G. Cullis, T. Hammerschmidt and G. P. Srivastava, Phys. Rev. B **74**, 245332 (2006).
[152] R. A. Hogg, T. A. Fisher, A. R. K. Willcox, D. M. Whittaker, M. S. Skolnick, D. J. Mowbray, J. P. R. David, A. S. Pabla, G. J. Rees, R. Gray, J. Woodhead, J. L. Sanchez-Rojas, G. Hill, M. A. Pate, P. N. Robson, Phys. Rev. B **48**, 8491 (1993).
[153] J. L. Sánchez-Rojas, A. Sacedón, F. González-Sanz, E. Calleja, and E. Muñoz, Appl. Phys. Lett. **65**, 2042 (1994).
[154] C. H. Chan, M. C. Chen, H. H. Lin, Y. F. Chen, G. J. Jan, and Y. H. Chen, Appl. Phys. Lett. **72**, 1208 (1998).
[155] T. B. Bahder, R. L. Tober and J. D. Bruno, Superlatt. and Microstruct. **14**,149 (1993).
[156] S. Cho, A. Majerfeld, A. Sanz-Hervás, J. J. Sánchez, J. L. Sánchez-Rojas, and I. Izpura, J. Appl. Phys. **90**, 915 (2001)
[157] P. Ballet, P. Disseix, J. Leymarie, A. Vasson, and A-M. Vasson, Phys. Rev. B **59**, R5308 (1999).
[158] L. R. Wilson, Ph.D. thesis, University of Sheffield, 1997.
[159] M. Moran, H. Meidia, T. Fleischmann, D. J. Norris, G. J. Rees, A. G. Cullis and M. Hopkinson, J. Phys. D **34**, 1943 (2001).
[160] D. Rideau, M. Feraille, L. Ciampolini, M. Minondo, C. Tavernier, H. Jaouen and A. Ghetti, Phys. Rev. B **74**, 195208 (2006).
[161] For Z^* the subscript *H* indicates that for this quantity we follow Harrison's definition (Ref. [57]), not to be confused with the commonly used quantity Z^*, the effective charge, which is instead equivalent to Harrison's e_T^*.
[162] N.Troullier and J. Martins, Phys. Rev. B **43**, 1993(1991).
[163] J. D. Pack and H. J. Monkhorst, Phys. Rev. B **16**, 1748 (1977).
[164] S. Q. Wang and H. Q. Ye, Phys. Stat. Sol. (b) **240**, 45 (2003).
[165] S. Q. Wang and H. Q. Ye, J. Phys. Condens. Matter **17**, 4475 (2005).
[166] S-G. Shen, D-X. Zhang and X-Q. Fan, J. Phys.: Condens. Matter **7**, 3529 (1995).
[167] C. Falter, W. Ludwig, M. Selmke and W. Zierau, Phys. Lett. A **105**, 139 (1984).
[168] M. Di Ventra and P. Fernández, Phys. Rev. B **56**, R12698 (1997).
[169] N. Bouarissa, Phys. Lett. A **245**, 285 (1998).
[170] R. Garg, A. Hüe, V. Haxha, M. A. Migliorato, T. Hammerschmidt, and G. P. Srivastava, Appl. Phys. Lett. **95**, 041912 (2009).
[171] J. P. Perdew and A. Zunger, Phys. Rev. B **23**, 5048 (1981).
[172] S. J. Clark, M. D. Segall, C. J. Pickard, P. J. Hasnip, M. J. Probert, K. Refson, M. C. Payne, Zeitschrift für Kristallographie **220**(5-6) pp.567-570 (2005).
[173] G. Tse, J. Pal, U. Monteverde, R. Garg, V. Haxha and M.A. Migliorato, J. Appl. Phys. **114**, 073515 (2013).
[174] A. D. Andreev and E. P. O'Reilly, Phys. Rev. B **62**, 15851 (2000).
[175] E. T. Yu, X. Z. Dang, P. M. Asbeck, S. S. Lau and G.J. Sullivan, J. Vac. Sci. Technol. B **17**, 1742 (1999).
[176] D. R. Hamann, Phys. Rev. B **40**, 2980 (1989).
[177] M.V. Barry, Proc. R. Soc. Lond. A **392**, 45 (1984).
[178] S. Y. Karpov, Phys. Status Solidi C **7**, 1841 (2010).
[179] F. Bernardini and V.Fiorentini, Appl. Phys. Lett **80**, 4145 (2002).
[180] K. Shimada, Jpn. J. Appl. Phys. 45, L358 (2006).
[181] I. Vurgaftman and J. R. Meyer, J. Appl.Phys. 94, 3675 (2003).
[182] J. Pal, G. Tse, V. Haxha, M. A. Migliorato and S. Tomić, Journal of Physics: Conference Series **367**,012006 (2012).

[183] J. Pal, G. Tse, V. Haxha, M. A. Migliorato, and S. Tomić,
Phys. Rev. B, **84**, p. 085211 (2011).
[184] M. Leroux, N. Grandjean, J. Massies, B. Gil, P Lefebvre, P. Bigenwald.
Phys. Rev. B **60**, 1496 (1999).
[185] N. Suzuki and N. Iizuka, Jpn. J. Appl. Phys. **38**, L363 (1999).
[186] S.-H. Park and S.-L. Chuang, Appl. Phys. Lett **76**, 1981 (2000).
[187] G. Vaschenko, C. S. Menoni, D. Patel, C. N. Tome, B. Clausen, N. F. Gardner, J. Sun,
W. Gotz, H. M. Ng, and A. Y. Cho, Phys. Status Solidi B **235**, 238 (2003).
[188] D. Cai and G.-Y. Guo, J. Phys. D: Appl. Phys. **42**, 185107 (2009).
[189] C. Adelmann, E. Sarigiannidou, D. Jalabert, Y. Hori, J.-L. Rouvie`re, B.Daudinc, S. Fanget,
C. Bru-Chevallier, T. Shibata and M. Tanaka, Appl. Phys. Lett. **82**, 4154 (2003).
[190] A. Helman, M. Tchernycheva, A. Lusson, E. Warde, F. H. Julien, Kh. Moumanis,
G. Fishman, E. Monroy, B. Daudin, D. Le Si Dang, E. Bellet-Amalric, and D. Jalabert,
Appl. Phys. Lett. **83**, 5196 (2003).
[191] M. Tchernycheva, L. Nevou, L. Doyennette, F. H. Julien, E. Warde, F. Guillot, E. Monroy,
E. Bellet-Amalric, T. Remmele and M. Albrecht, Phys. Rev. B **73**, 125347 (2006).
[192] C. Buchheim, R. Goldhahn, A. T. Winzer, G. Gobsch, U. Rossow, D. Fuhrmann,
A. Hangleiter, F. Furtmayr and M. Eickhoff, Appl. Phys. Lett. **90**, 241906 (2007).
[193] X. Y. Cui, D. J. Carter, M. Fuchs, B. Delley, S. H. Wei, A. J. Freeman, and C. Stampfl,
Phys. Rev. B **81**, 155301 (2010).
[194] C. C. Shieh, X.Y.Cui, B.Delly and C.Stampfl , J. Appl. Phys. 109, 083721 (2011).
[195] J. Pal, G. Tse, V. Haxha, M. A. Migliorato and S. Tomić,
Opt. Quant. Electron, 44, 195 (2012).
[196] O. Ambacher, J. Majewski, C. Miskys, A. Link, M. Hermann, M. Eickhoff, M. Stutzmann,
F. Bernardini, V. Fiorentini, V. Tilak, B. Schaff, and L. F. Eastman,
J. Phys.: Condens. Matter **14**, 3399 (2002).

[198] H.Y.S. Al-Zahrani, J. Pal and M.A. Migliorato, NanoEnergy (2013) (Article in press).
http://dx.doi.org/10.1016/j.bbr.2011.03.031
[199] S. Massidda, R. Resta, M. Posternak and A. Baldereschi, Phys. Rev. B, **52**, (R)16977 (1995)
[200] W. A. Harrison, Phys. Rev. B **10**, 767 (1974).
[201] S.-H, Hang, S. F. Chichibu, Appl. Phys. Lett. **112**, 073503 (2012).
[202] G. Carlotti, G. Socino, A. Petri and E. Verona, Appl. Phys. Lett. **51**, 1889 (1987).
[203] M.-H. Kim, M. F. Schubert, Q. Dai, J. K. Kim, E. F. Schubert, J. Piprek, and Y. Park,
Appl. Phys. Lett. **91**, 183507 (2007).
[204] J. Piprek, Phys. Stat. Sol. (a) **207**, 2217 (2010).
[205] S. Chichibu, T. Azuhata, T. Sota and S. Nakamura, Appl. Phys. Lett. **69**, 4188 (1996).
[206] T. Takeuchi, S. Sota, M. Katsuragawa, M. Komori, H. Takeuchi, H. Amano, and I. Akasaki,
Jpn. J. Appl. Phys., **36**, p. L382 (1997).
[207] M.-H. Kim, M. F. Schubert, Q. Dai, J. K. Kim, E. F. Schubert, J. Piprek and Y. Park,
Appl. Phys. Lett. **91**, 183507 (2007).
[208] S. Huang, Z. Chen, Y. Xian, B. Fan, Z. Zheng, Z. Wu, H. Jiang and G. Wang,
Appl. Phys. Lett. **101**, 041116 (2012).
[209] X. Li, X. Ni, H. Y. Liu, F. Zhang, S. Liu, J. Lee, V. Avrutin, Ü. Özgür, T. Paskova,
G. Mulholland, K. R. Evans, and H. Morkoç, Phys. Stat. Sol (c), **8**, p 1560-1563 (2011).
[210] H. Masui, S. Nakamura, S. P. DenBaars and U. K. Mishra,
IEEE Trans. Electron Devices, **57**, 88 (2010).
[211] Y. Kawaguchi1, C-Y. Huang, Y-R. Wu, Q. Yan, C-C. Pan, Y. Zhao, S. Tanaka, K. Fujito,
D. Feezell1, C. G. Van de Walle, S. P. DenBaars and S. Nakamura,
Appl. Phys. Lett. **100**, 231110 (2012).
[212] S. Takagi, Y. Enya, T. Kyono, M. Adachi, Y. Yoshizumi, T. Sumitomo, Y. Yamanaka,
T. Kumano, S. Tokuyama, K. Sumiyoshi, N. Saga, M. Ueno, K. Katayama, T. Ikegami,
T. Nakamura, K. Yanashima, H. Nakajima, K. Tasai, K. Naganuma, N. Futagawa,
Y. Takiguchi, T. Hamaguchi and M. Ikeda, Appl. Phys. Exp. **5**, 082102 (2012)

[213] M. J Lai, M. J. Jeng, and L. B Chang, Japan. J. Appl. Phys. **49**, 021004 (2010)
[214] T. Detchprohm, M. Zhu, W. Zhao, Y. Wang, Y. Li, Y. Xia and C. Wetzel, Phys. Stat. Sol C **6**, S840-S843(2009)
[215] B. G. Crutchley, I. P. Marko, S. J. Sweeney, J. Pal and M. A. Migliorato, Phys. Stat. Sol, **250**, 698–702 (2013)
[216] K. Shimada, T. Sota, K. Suzuki and H. Okumura, Jpn. J. Appl. Phys. **37**, Pt.2,12A (1998).
[217] G. Vaschenko, D. Patel, C. S. Menoni, N. F. Gardner, J. Sun, W. Go¨tz, C. N. Tome´ and B. Clausen, Phys. Rev. B **64**, 241308 (2001).
[218] A. R. Adams, M.Silver, and J. Allam, High Pressure in Semiconductor Physics II, pp 310 (1998)
[219] T. Suski, S.P. Łepkowski, G. Staszczak, R. Czernecki, P. Perlin, and W. Bardyszewski, J. Appl. Phys. **112**, 053509 (2012).
[220] R. J. Thomas, M. S. Boley, H. R. Chandrasekhar, M. Chandrasekhar, C. Parks, A. K. Ramdas, J. Han, M. Kobayashi, and R. L. Gunshor, Phys. Rev. B **49**, p. 2181 (1994).
[221] J. Pal, M. A. Migliorato, C-K. Li, Y-R. Wu, B. G. Crutchley, I. P. Marko and S. J. Sweeney, J. Appl. Phys (Article in Press)
[222] N. Okamoto, K. Hoshino, N. Hara, M. Takikawa, Y. Arakawa, J. Cryst. Growth **272**, 278 (2004).
[223] C. X. Wang, K. Tsubaki, N. Kobayashi, T. Makimoto, and N. Maeda, Appl. Phys. Lett. **84**, 2313 (2004).
[224] S. Ghosh, P. Waltereit, O. Brandt, H. T. Grahn, and K. H. Ploog, Phys. Rev. B **65**, 075202 (2002).
[225] I. Vurgaftman and J. Singh, Appl. Phys. Lett. **64**, 1472 (1994).
[226] J. Zhang and N. Tansu, J. Appl. Phys. **110**, 113110 (2011).
[227] R. P. Feynman, J. Microelectromechanical Systems, **1**, 60 (1992).
[228] A. I. Hochbaum, P. D. Yang, Chem. Rev. **110**, 527 (2010).
[229] P. Yang, R. Yan and M. Fardy, Nano Lett. **10**, 1529 (2010).
[230] H. P. T. Nguyen, Y-L. Chang, I. Shih, Z. Mi, IEEE Journal of Selected Topics in Quantum Electronics, **17**, 1062-1069 (2011).
[231] Q. Li, J. B. Wright, W. W. Chow, T. S. Luk, I. Brener, L. F. Lester, and G. T. Wang, Optics Express, **20**, 17873 (2012).
[232] J. Heo, W. Guo and P. Bhattacharya, Appl. Phys. Lett. **98**, 021110 (2011).
[233] J.-W. Yu, P.-C. Yeh, S.-L. Wang, Y.-R. Wu, M.-H. Mao, H.-H. Lin, and L.-H. Peng, Appl. Phys. Lett. **101**, 183501 (2012).
[234] C-Y. Chen and Y-R. Wu, J. Appl. Phys. **113**, 214501 (2013).
[235] G. Bester, A. Zunger, X. Wu and D. Vanderbilt, Phys. Rev. B **74**, 081305(R) (2006).
[236] V. Haxha, I. Drouzas, J.M. Ulloa, M. Bozkurt, P.M. Koenraad, D.J. Mowbray, H.Y. Liu, M.J. Steer, M. Hopkinson, M.A. Migliorato, Phys Rev B **80**, 165334 (2009).
[237] P. Michler, A. Kiraz, C. Becher, W. V. Schoenfeld, P. M. Petroff, L. D. Zhang, E. Hu and A. Imamoglu, Science **290**, 2282 (2000).
[238] R. M. Stevenson, R. J. Young, P. Atkinson, K. Cooper, D. A. Ritchie and A. J. Shields, Nature **439**, 179 (2006).
[239] S. Kako, C. Santori, K. Hoshino, S. Gotzinger, Y. Yamamoto, and Y. Arakawa, Nature Mat. **5**, 887 (2006).
[240] L.-W. Ji, Y.K. Su, S.J. Chang, C.S. Chang, L.W. Wu, W.C. Lai, X.L. Du and H. Chen, Journal of Crystal Growth **263**, 114 (2004).
[241] Il-Kyu Park, Min-Ki Kwon, Seong-Bum Seo, Ja-Yeon Kim, Jae-Hong Lim and Seong-Ju Park, Appl. Phys. Lett. **90**, 111116 (2007).
[242] K. Tachibana, T. Someya and Y. Arakawa, Appl. Phys. Lett. **74**, 383 (1999).
[243] T. Xu, A. Y. Nikiforov, R. France, C. Thomidis, A.Williams and T. D. Moustakas, Phys. Stat. Sol. (a) **204**, 2098 (2007).
[244] C. B. Soh, W. Liu, S. J. Chua, S. S. Ang, Rayson J. N. Tan, S. Y. Chow, J. Appl. Phys. **108**, 093501 (2010).

[245] A. Asgari and S.Razi, Opt. Exp. **18**, 14604 (2010).
[246] G. Liu , H. Zhao , J. Zhang, J. H. Park L. J. Mawst and N.Tansu, Nanoscale Research Letters, **6**,342 (2011).
[247] S. Tomić, N. M. Harrison and T. S. Jones, Opt. Quant. Electron. **40**, 313 (2008).
[248] A. F. Jarjour, R. A. Taylor, R. A. Oliver, M. J. Kappers, C. J. Humphreys, A. Tahraou, Appl. Phys. Lett. **91**, 052101 (2007).
[249] O. Moriwaki, T. Someya, K. Tachibana, S. Ishida and Y. Arakawa, Appl. Phys. Lett. **76**, 2361 (2004).
[250] H. Schömig, S. Halm, A. Forchel1, G. Bacher, J. Off and F. Scholz, Phys. Rev. Lett. **92**, 106802 (2004).
[251] D. P. Collins, A. F. Jarjour, R. A. Taylor, M. Hadjipanayi, R. A. Oliver, M. J. Kappers, C. J. Humphreys and A. Tahraoui, Phys. Status Solidi C **6**, 864 (2009).
[252] D. P. Collins, A. F. Jarjour, R. A. Taylor, M. Hadjipanayi, R. A. Oliver, M. J. Kappers, C. J. Humphreys and A. Tahraoui, Nanotechnology, **20**, 245702(2009).
[253] R. A. Taylor, A. F. Jarjour, D. P. Collins, M. J. Holmes, R. A. Oliver, M. J. Kappers and C. J. Humphreys, Nanoscale Res Lett **5,** 60 (2010).
[254] A. D. Andreev and E. P. O'Reilly, Appl. Phys. Lett. **79**, 521 (2001).
[255] D. Simeonov, A. Dussaigne, R. Butté and N. Grandjean, Phys. Rev. B **77**, 075306 (2008).
[256] D. Williams, A. Andreev, and E. O'Reilly, Superlattices and Microstructures **36**, 791 (2004).
[257] P.-O. Löwdin, Phys. Rev. **97**, 1474 -1489 (1955).
[258] G. Makov and M. C. Payne, Phys. Rev. B **51**, 4014 (1995).
[259] S. Tomić and N. Vukmirović, Phys. Rev. B **79**, 245330 (2009).
[260] J. Renard, R. Songmuang, C. Bougerol, B. Daudin, and B. Gayral, Nano Lett. **8**, 2092 (2008).